NTNU
Norwegian University of
Science and Technology

Spatial reservoir characterisation with focus on distribution of porosity and permeability properties:

A study of the Tarbert and Ness Formations at the Gullfaks Field

Ina Cathrine Sagen

Petroleum Geoscience and Engineering
Submission date: February 2016
Supervisor: Steinar Løve Ellefmo, IGB
Co-supervisor: Maarten Felix, IGB

Norwegian University of Science and Technology
Department of Geology and Mineral Resources Engineering

Abstract

This thesis aims to characterise the spatial petrophysical distribution of porosity and permeability properties in the Tarbert and Ness Formation at the Gullfaks Field. The geomodelling software Leapfrog Geo was used to build a reservoir model and estimate the spatial petrophysical properties. Four different procedures were used to obtain the results; the Geological Model (GM), the Geological Model Fault Block 2 (GM Fault Block 2), petrophysical model of the Geological Model (GM) volume and petrophysical model of the Geological model Fault Block 2 (GM Fault Block 2) volume.

The results showed that Leapfrog Geo is suitable to characterise petrophysical properties in a reservoir model where the main data source is well data. However, with additional data sources, are probably other types of software preferable. The radial basic function (RBF) is suitable to interpolate and estimate fault iso-surfaces and petrophysical data. However, not formation iso-surfaces that had to be triangulated. The Geological Model Fault Block2 (GM Fault Block 2) volume procedure yielded the best result, because of the good volume control both within the fault block and the formations. A 40m x 40m x 10m grid cell size yielded the best result and grid cell size is constrained both by smoothness and computer power.

Sammendrag

Denne oppgaven tar sikte på å karakterisere den romlige petrofysiske fordeling av porøsitet og permeabilitet verdier i Tarbert og Ness formasjonen i Gullfaks-feltet. Det geologiske modelleringsprogrammet Leapfrog Geo ble brukt til å bygge en reservoarmodell og beregne de romlige petrofysiske egenskaper. Fire forskjellige fremgangsmåter ble anvendt for å oppnå resultatene; den "geologiske modellen" (GM), den "geologiske modellen forkastningsblokk" (GM Fault blokk 2), "petrofysisk modell av den geologiske modellen (GM) volum" og "petrofysisk modell av den geologiske modellen forkastningsblokk 2 (GM Fault Block 2) volum".

Resultatene vister at Leapfrog Geo er egnet til å karakterisere petrofysiske egenskaper i en reservoarmodell, hvor den viktigste datakilden er brønndata. Men med flere datakilder, er trolig andre typer programvare å foretrekke. Radial Basic Function (RBF) er egnet til å interpolere og estimere forkastnings iso-overflater og petrofysisk data. Men ikke formasjons iso-overflater, som her er triangulerte. Den "geologiske modellen forkastningsblokk 2 (GM Fault Block 2) volum" prosedyren ga det beste resultatet, på grunn av god volumkontrollen både i forkastningsblokk og formasjonene. En 40m x 40m x 10m grid celle størrelse ga det beste resultatet og blokk celle størrelse er begrenset både av glatthet og datakraft.

Preface

This text is submitted as master thesis in Petroleum Geology (TGB4900) at the Norwegian University of Science and Technology (NTNU). The research project started in August 2015 and was completed in February 2016.

The data used in this thesis was retrieved from the "NPD-Schlumberger, PETREL Ready Database", where Statoil owns the data. Statoil, NPD and Schlumberger has given the Department of Petroleum Engineering and Applied Geophysics (IPT) access to these data for research and teaching purposes only.

I would like to credit those who have contributed in different ways throughout the period:

- My main supervisor at the Department of Geology and Resources Engineering, Førsteamanuensis Steinar Løve Ellefmo is thanked for giving me access to the Leapfrog Geo software and providing invaluable support and comments to the modelling process and thesis.
- My supervisor at the Department of Geology and Resources Engineering, Førsteamanuensis Maarten Felix is thanked for valuable support and comments to enhance the thesis.
- Research Assistant Dicky Harishidayat at the Department of Petroleum Engineering and Applied Geophysics is thanked for providing access the data in the "PETREL Ready Database" and insight into the PETREL model.

Additionally, I would like to thank my fellow master students and staff at both the Department of Geology and Mineral Resources Engineering and Department of Petroleum Engineering and Applied Geophysics for the great time I have had at NTNU.

Ina Cathrine Sagen
Trondheim, February 2016

Contents

Abstract **i**

Sammendrag **iii**

Preface **v**

List of Figures **xi**

1 Introduction **1**
- 1.1 Problem definition and aim of work 1
- 1.2 Organisation of the thesis 2

2 Petrophysics in sedimentary media **3**
- 2.1 Properties of porous media 3
  - 2.1.1 Porous media 3
  - 2.1.2 Porosity 5
  - 2.1.3 Permeability 7
  - 2.1.4 Additivity 9
- 2.2 Sedimentological factors controlling porosity and permeability 10
  - 2.2.1 Texture and fabric 11
  - 2.2.2 Sedimentary structures 12
- 2.3 Estimation of petrophysical properties 14
  - 2.3.1 Upscaling 15
  - 2.3.2 Variogram 15
  - 2.3.3 Kriging 17
  - 2.3.4 Algorithm choice 19

3 Geology of the study area **21**
- 3.1 Geological setting 23
  - 3.1.1 Northern North Sea 23
  - 3.1.2 Gullfaks 25
- 3.2 Lithological description of selected interval 28
  - 3.2.1 Ness Formation 28
  - 3.2.2 Tarbert Formation 31

4 Conceptual Geological Model 35
4.1 Morphology and sequence stratigraphy 35
4.1.1 Mesaverde Group 39
4.2 Facies model 40
4.3 Petrophysical model 44

5 Geomodeling tool 47
5.1 Workflow 47
5.1.1 Leapfrog Geo 48
5.1.2 Generic approach 51
5.2 Input parameters 52
5.2.1 Structural data 53
5.2.2 Well data 55
5.3 Estimated parameters 59
5.3.1 Meshes 59
5.3.2 Volume and grid 61
5.3.3 Output 62

6 Results 65
6.1 The Geological Model (GM) 65
6.2 The Geological Model Fault Block 2 (GM Fault Block 2) 67
6.3 Petrophysical model of the Geological Model (GM) volum 68
6.3.1 Interpolated model 68
6.3.2 Block Model 71
6.4 Petrophysical model of the Geological Model Fault Block 2 (GM Fault Block 2) volume 73
6.4.1 Interpolated model 73
6.4.2 Block model: Grid cells 70m x 70m x 40m 74
6.4.3 Block model: Grid cells 40m x 40m x 10m 76
6.4.4 Block model: Grid cells 10m x 10m x 5m 79

7 Discussion and Conclusion 81
7.1 Input data and method 81
7.2 Results 82
7.3 Conclution 84

Bibliography 85

A Appendix: Input graphs 95
A.1 Porosity well graphs 95
A.2 Permeability well graphs 98

B Appendix: Property Model GM fault block 2 103
B.1 Interpolated Model 103
B.1.1 Tarbert Upper 103
B.1.2 Tarbert Middle 104

B.1.3 Tarbert Lower 105
B.1.4 Ness Upper 106
B.1.5 Ness Lower 107
B.2 Block model 108
B.2.1 Tarbert Upper 108
B.2.2 Tarbert Middle 109
B.2.3 Tarbert Lower 110
B.2.4 Ness Upper 111
B.2.5 Ness Lower 112

List of Figures

2.1.1 Illustration of REV (Nield and Bejan, 2012) 5
2.1.2 Illustration of cubic and rhombohedral packing (Graton and Fraser, 1935) 5
2.1.3 Core plug sampling 7
2.1.4 Capillaric tube model (Nordahl, 2004) 8
2.2.1 Effect of grain size and sorting (Brayshaw et al., 1996) 11
2.2.2 Illustration of sedimentary units (Nordahl, 2004) 12
2.2.3 Illustration of shale effect on porosity (Dewan, 1983) 13
2.2.4 Left: Scale effect on permeability (Ringrose et al., 1993). Right: Example of vertical and horizontal permeability. 13
2.3.1 Experimental variogram (Caers, 2011) 17
2.3.2 Illustration of the Kriging method (Ringrose and Bentley, 2015) . . 18

3.0.1 Location map of Gullfaks (Fossen and Hesthammer, 1998) 22
3.1.1 Schematic event chart Nøttvedt et al. (1995) 23
3.1.2 Map of rift zones northern North Sea (Færseth, 1996). 25
3.1.3 Profile Gullfaks Fault Block (Rouby et al., 1996). 25
3.1.4 Structural development domino faults (Petterson et al., 1990). 26
3.2.1 Stratigraphic column from Middle to Upper Jurassic (Husmo et al., 2003). 28
3.2.2 Core samples of Ness formation (NPD-Factpages, 2015) 29
3.2.3 Stratigraphic column, Brent GP (Hesthammer and Fossen, 1997). . . 30
3.2.4 Core sample from Tarbert formation (NPD-Factpages, 2015) 31
3.2.5 Illustration transgressive environment(Folkestad et al., 2014) 32
3.2.6 Stratigraphic column with interpretations (Olaussen et al., 1992). . . 33

4.1.1 A(Left): Delta elements (Bhattacharya, 2006). B (Right): Niger delta 36
4.1.2 Stratigraphic column with interpretations (Walker and Cant, 1984). 36
4.1.3 Morphological elements from a wave-dominated estuary (Dalrymple et al., 1992) 37
4.1.4 Marginal-marine environments (Boyd et al., 1992) 37
4.1.5 Chart with biomarkers and system tracs for the Brent Group (Fjellanger et al., 1996). 38

4.1.6 Cliff house sandstone (Eschard et al., 1993) 40
4.2.1 Facies architecture (Went et al., 2013) 41
4.2.2 A (Upper): Topographic view of Top Ness. B (Lower): Top Tarbert. 43
4.3.1 A (Upper): Top Ness, porosity. B (Lower): Top Ness, permeability. . 45
4.3.2 A (Upper): Top Tarbert, porosity. B (Lower): Top Tarbert, permeability. 46

5.1.1 Flowchart 48
5.1.2 Leapfrog Geo workflow scheme (Cowan et al., 2002). 49
5.1.3 Illustration of Delaunay triangulation. 50
5.1.4 Data-driven generic approach (Ringrose and Bentley, 2015). 51
5.2.1 Topographic overview of the Gullfaks Field. 52
5.2.2 Formations and surfaces in the Gullfaks model. 53
5.2.3 Surfaces from scatter-data. 53
5.2.4 The faults from the point-data. 54
5.2.5 A (left): Hole-id) and start coordinates. B (right): Plot of well points. 55
5.2.6 A (Upper): Well points of porosity. B (Lower): Well points of permeability. 56
5.2.7 A (Left): Histogram of porosity properties. B (Right):Histogram of permeability properties. 57
5.2.8 A (Upper): Well A10: Porosity versus depth plot. B (Lower): Permeability versus depth plot. 58
5.3.1 A (Left): Iso-surface from radial basic function. B (Right): Triangulated Iso-surface. 59
5.3.2 Mesh grid (Royer et al., 2015). 60
5.3.3 Iso-surfaces cut through of a fault. 61
5.3.4 Regular grid cell 62

6.1.1 GM volume model. 66
6.2.1 Selected area of volume model. 67
6.3.1 A (Upper): Porosity volume model. B (Lower): With well placement 69
6.3.2 A (Upper): Permeability volume model. B (Lower): With well placement 70
6.3.3 A (Left): Porosity block model. B (Right): Cut through diagonal from North to East corner 71
6.3.4 A (Left): Permeability block model. B (Right): Cut through diagonal from North to East corner 72
6.4.1 Upper Tarbert: Interpolated model. 73
6.4.2 Number of blocks 74
6.4.3 Upper Tarbert: Interpolated model. 75
6.4.4 Upper Ness block model 75
6.4.5 Number of blocks 76
6.4.6 Upper Tarbert: Block model. 77
6.4.7 Upper Tarbert: Block model. 77
6.4.8 Block model of all the formations 78

B.1.1 Tarbert Upper: Porosity volume 103

B.1.2 Tarbert Upper: Permeability volume 104
B.1.3 Tarbert Middle: Permeability volume 104
B.1.4 Tarbert Lower: Porosity volume 105
B.1.5 Tarbert Lower: Permeability volume 105
B.1.6 Ness Upper: Porosity volume 106
B.1.7 Ness Upper: Permeability volume 106
B.1.8 Ness Lower: Porosity volume 107
B.1.9 Ness Lower: Permeability volume 107
B.2.1 Tarbert Upper: Porosity block model 108
B.2.2 Tarbert Upper: Permeability block model 108
B.2.3 Tarbert Middel: Porosity block model 109
B.2.4 Tarbert Niddle: Permeability block model 109
B.2.5 Tarbert Lower: Porosity block model 110
B.2.6 Tarbert Lower: Permeability block model 110
B.2.7 Ness Upper: Porosity block model 111
B.2.8 Ness Upper: Permeability block model 111
B.2.9 Ness Lower: Porosity block model 112
B.2.10 Ness Lower: Permeability block model 112

Chapter 1

Introduction

Estimation of the petrophysical properties porosity and permeability is important for the oil industry and a lot of research goes into estimating petrophysical properties from subsurface data.

Petterson et al. (1990) described the Gullfaks Field as the most complex structure so far developed in Norwegian waters. In this thesis a reservoir model is built for the Gullfaks Field.

The reservoir model is built for petrophysical property characterisation. Leapfrog Geo, a implicit and deterministic modelling tool is used to build the model and estimate the properties. Few, if any previous studies have used this software for an offshore petroleum field.

1.1 Problem definition and aim of work

The aim of the thesis is to produce a spatial reservoir characterisation of the Upper Brent GP (base Cretaceous- top Etive FM) at the Gullfaks field, with focus on distribution of porosity and permeability properties. The main elements in the thesis will includes a geological conceptual model and a property models The geological conceptual model include a characterisation of lithology and depositional setting of the Upper Brent Gp. The property model is a spatial reservoir characterisation of the porosity and permeability properties. These properties can be estimated from well-data to a reservoir model by implicit modelling and geostatistical estimation, which is performed in the software Leapfrog Geo. The modelling process and workflow will be reviewed in detail.

The overall goal of the thesis is to evaluate if the spatial distributions of the porosity and permeability properties of the model are realistic compared to the geological conceptual model and do the chosen model method and geostatistical method give a good representation of the chosen area.

1.2 Organisation of the thesis

This constitutes of in total seven chapters, including the introduction. The thesis is organised in five sections:

1. Theoretical background (Chapter 2):

The theoretical background in Chap. 2. introduce petrophysical conceptual models, sedimentological implications on petrophysical properties, and different published methods for estimation of porosity and permeability from well data. The chapter also includes a short review of different algorithm methods used in reservoir modelling for petrophysical estimation and simulation. The petrophysical background theory is reviewed in a cross-disciplinary manner, and constitute the backbone for further discussion of well data and reservoir modelling (e.g. Chapter 5).

2. Geological conceptual model (Chapter 3 and 4):

Chapter 3. review the geological background theory of the Gullfaks field in the North Sea. The chapter has a divided focus on structural and lithological events. Chapter 4. focuses on depositional environments and morphology encountered in the Ness and Tarbert formation.

3. Geomodeling tool (Chapter 5):

Chapter 5. describes the modelling tool used in this thesis, review the input parameters and the methodological workflow.

4. Results (Chapter 6):

The property model is the output of the modelling procedure described in the previous chapter and constitute of a porosity model and a permeability model. This chapter is divided with respect to the procedures that is used to yield the results

5. Discussion and conclusion (Chapter 7):

Chapter 7. evaluates the results of the property model (Chap. 6) and the workflow of the modelling procedure. This is the discussion chapter. At the end, is application of the results evaluated and concluded.

Chapter 2

Petrophysics in sedimentary media

The main goal in petroleum exploration is to find a reservoir rock, with the ability to store an economically profitable amount of hydrocarbons. This goal requires that hydrocarbons are allowed to flow freely through the reservoir rock. A reservoir rock can more precisely be described as a porous media. The first property, the ability to store, is called *porosity*. The second property, the ability to transmit, is called *permeability*. These two properties, or parameters as they also might be called, are important to estimate in petrophysics.

This chapter will outline some basic concepts regarding petrophysics and estimation. The topic of this thesis is somewhat cross-disciplinary, but is founded on a geological perspective. The readers might have different backgrounds, and this chapter can serve as an introduction to the theories and model assumptions relevant to this thesis.

2.1 Properties of porous media

A broad range of earth science textbooks covers porous mediums as topic. However, the different fields may focus on different aspects of the media's properties. Most of the background theory presented here can be found in textbooks describing dynamics of porous media (Bear, 1988; Nield and Bejan, 2012; Scheidegger, 1974).

2.1.1 Porous media

A porous media is a multiphase matter, which consists of a solid matrix and a pore space (Allen, 1985; Bear, 1988; Nield and Bejan, 2012). Simply stated, the pore space is the "empty" space in a solid matrix that is filled with a fluid (e.g. air, water or oil).

Allen (1985) describes the solid phase as closely packed mineral particles, while he uses the term voids for the pore space. The shape, size, disposition and connectedness of the voids are dependent on how the mineral particles are packed. Scheidegger (1974) defines the pores as the intermediate size between molecular interstices and caverns. In order to be defined as a porous medium, these 'intermediate sized' pores should be frequently distributed in the solid and at least some of the pores should be interconnected. Interconnected pores have the ability to transfer one or more fluids. If the pore space is saturated by one fluid it is called a single-phase flow. If the pore is saturated by a liquid and a gas it is a two-phased flow (Nield and Bejan, 2012).

Characterising the geometry of the pores or voids and their interconnection is a complex problem. As Allen (1985) discussed the voids are depending on the "packing" of the medium, which can be irregular both in shape and in appearance through the medium. It is challenging to define a diameter for a single pore "vein", predict the path of the flow through the medium, the geometrical volume and surface of the pore "vein". Defining a diameter for a single pore "vein", predict the path the flow will take through the medium, geometrical volume and surface is challenging. There are several methods to "deriving the laws governing the macroscopic variables" (Nield and Bejan, 2012), e.g. designed porous media (Bejan, 2004; Bejan et al., 2004), statistical (Georgiadis and Catton, 1987, 1988) and spatial (Bear, 1988; Bear and Bachmat, 1990) methods. These methods will not be discussed in detail in this thesis. However, the concept behind the spatial method Representative Elementary Volume (REV) has become so commonly used that it has to be mentioned.

The continuum approach presume that porous matter behave as a hypothetical substance, which is continuous throughout the spatial domain it occupies, and can be described by a set of variables (Bejan et al., 2004). This method, also called the *effective medium approximation* (Bruggeman, 1935), replaces a complex medium with a hypothetical homogeneous one. The method treats the porous media as a continuum, where a particle associated with a volume is chosen. The particle must be large enough to give a mirco-geometry average, but small enough to be representative for the centroid of the particle, which gives an average representative volume for the medium. This volume is called a *Representative Elementary Volume* (REV) (Fig.2.1.1) (Bear, 1988). In the later years this method has been associated with upscaling of extensive properties (like permeability) in heterogeneous media for use in reservoir modelling (e.g. Nordahl and Ringrose (2008); Ringrose et al. (2008)).

Other properties that describes aspects of porous media are homogeneity and isotropy. A medium is said to be *homogeneous* if certain properties of the medium is independent of position within the medium. When the properties are dependent on position the medium is *heterogeneous*. Likewise a property may vary with the

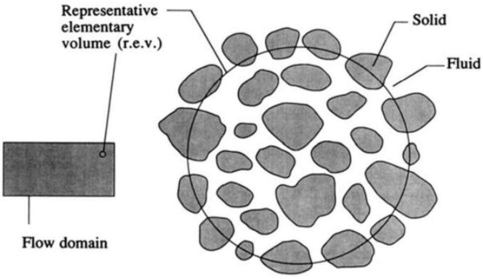

Figure 2.1.1. Representative Elementary Volume (REV): the intermediate size relative to flow domain and pore space. From Nield and Bejan (2012).

direction it is measured within the medium, when independent of direction the medium is called *isotropic*. When dependent on measured direction the medium is said to be *anisotropic* (Bear and Bachmat, 1990; Sheriff and Geldart, 1995). Depending on the measured volume, most reservoirs are heterogeneous and anisotropic in nature.

2.1.2 Porosity

Sedimentary rocks have an inherited (primary) porosity. This porosity is dependent on how the particles in the medium is packed together. Conceptually these particles can be seen as equally sized, uniform spheres. The space between the spheres is the porosity. In this subchapter is a short overview of the basic concept of porosity is given, followed by an overview of permeability in the next subchapter. The background is based on the articles by Fraser (1935); Graton and Fraser (1935) and textbooks from Bear (1988); Zolotukhin and Ursin (2000).

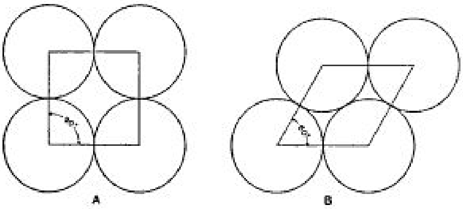

Figure 2.1.2. Illustration of A) cubic and B) simple rhombohedral packing of equally sized spheres. From Graton and Fraser (1935).

The squares inside figure 2.1.2 represents a unit cell from which the pore or void volume can be calculated. By looking at the cubic pacing in Fig.2.1.2A) it is easy to see that the pore volume is the difference between the total volume of the cube and the volume of the solid spheres. The total porosity (ϕ), a dimensionless property, can be represented by assuming parallel cylindrical pores. Where the *total* porosity is the ratio between the pore volume (V_p) and the total volume (V_b)

$$\phi = \frac{V_p}{V_b} \tag{2.1}$$

or as the fraction of the total (bulk) volume (V_b) subtracted the solid volume (V_s) by assuming cubic-packed monosized spheres

$$\phi = \frac{V_b - V_s}{V_b}. \tag{2.2}$$

By using equation (2.2) the porosity of the cubic packing is 0.476 (47.6%) and the rhombohedral packing has a porosity of 0.26 (26.0%). It is important that the total volume (bulk volume) that is used in these equations are representative for the medium (REV) as discussed earlier, obviously this is not a problem with the hypothetical problem in this case. However, it can be seen that the porosity is just dependent on the grain configuration and independent of the sphere size.

In natural occurring mediums, e.g. sandstones, the solid matrix can form a complex volume where not all the pore spaces are interconnected. These connected pores can be referred to as the *effective* porosity ϕ_e. The relation between interconnected pore volume ($V_{p,e}$) and non-interconnected pore volume ($V_{p,ne}$) is given by

$$V_p = V_{p,e} + V_{p,ne}. \tag{2.3}$$

Effective porosity can then be given as in equation (2.1), but as the ratio between interconnected pore volume and the total volume

$$\phi_e = \frac{V_{p,e}}{V_b}. \tag{2.4}$$

The *specific surface* area (S) is another geometrical quantity of porous media. It is defined as the ratio between the total internal surface area of the pores (A_s) and the total volume

$$S = \frac{A_s}{V_b} \quad [S] = [m^{-1}]. \tag{2.5}$$

Alternatively, the specific surface area for the solid (S_s) phase can be found as

$$S_s = \frac{A_s}{V_s} = \frac{A_S}{V_b(1-\phi)}, \tag{2.6}$$

which gives the relation

$$S = S_s(1-\phi). \tag{2.7}$$

The ratio between A_s and V_s indicates that the sphere size increases with decreasing radius, and that the specific surface area is dependent on the sphere size.

Both porosity and the specific surface area are for complex solid matrix found by experimental volume values. Direct porosity measurements are performed on core plugs from well samples. Additionally, porosity can be estimated from wireline logs, however this data type is not used in this thesis and will therefore not be addressed.

The cylindrical core plugs are 3-5 cm long and with a diameter of ~3 cm. Horizontal samples are taken approximately every 30 cm of the core, while vertical samples (vertical to the bedding plane, see fig. 2.1.3) are taken less frequently. Porosity measurements are done in the laboratory, either with a gas expansion method where interconnected porosity values are measured or with a destructive method where the total porosity value is measured. Thin sections and image analysis (e.g. BSE image) can be used to separate connected and interconnected pores. This method gives an estimation based on a 2D sample.

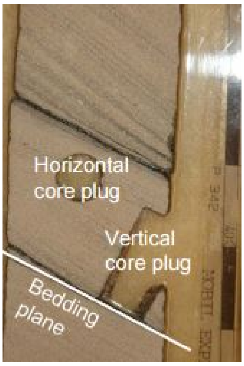

Figure 2.1.3. Core plug sampled in horizontal and vertical direction. Figure from Statoil.

2.1.3 Permeability

Permeability is the medium's capability to transmit fluid, and is therefore only related to interconnected and permeable pores. For a particular medium with a single fluid flowing through it, a constant permeability value can be found. This value is called *absolute* permeability. If more than one fluid flows through the medium (e.g. oil and water), the *effective* permeability depend on each of the fluids relative saturation. In that case, the *relative* permeability to a specific fluid (e.g. oil) can be found as the ratio of the rock's effective permeability to this particular fluid and its absolute permeability (Zolotukhin and Ursin, 2000). In this thesis only single fluid flow will be discussed.

In order to determine the permeability of a porous medium experimentally, the fluid flow rate (Q) is measured through a core plug. What might be the most famous experimentally investigation of this was performed by Henry Darcy, proven in 1856 (Bear, 1988; Zolotukhin and Ursin, 2000). He noticed that the drop in water pressure across a one dimensional sand filter was proportional to the water filtration velocity, giving the following relation:

$$Q = K * A\frac{h}{\Delta l}, \quad [Q] = [m^3/s]. \tag{2.8}$$

Where Q is flow rate, h is difference in manometer levels (hydrostatic pressure gradient across the filter medium), A is the cross-sectional area in flow direction and Δl is the length of the medium. The proportionality coefficient K [m/s] represent hydraulic conductivity. The Darcy law is valid for laminar, incompressible fluid flow through a fully saturated homogeneous medium at low speed. Note that this is the one-dimensional equation, for the generalised three-dimensional differential equation see e.g. Bear (1988); Scheidegger (1974).

Since Darcy performed his experiment with water, the fluid viscosity (μ) was not included in the equation. The proportionality coefficient K is therefore dependent on both fluid and matrix properties. The relational effect of the grain configuration (matrix) and the fluid can be separated by the relation from Nutting (1930):

$$K = k\frac{\gamma}{\mu} = k\frac{\rho g}{\mu} = k\frac{g}{v}. \tag{2.9}$$

Where the g is the gravitation constant, v is kinematic viscosity, ρ is the fluid density and γ is the specific weight of the fluid. The k is the specific or intrinsic permeability with dimension m^2. The specific permeability, referred to as just permeability in this thesis, is only dependent on the matrix properties. The Darcy law can now be written as

$$Q = \frac{k}{\mu}\frac{(\Delta p + \rho g \Delta z)}{\Delta l}. \tag{2.10}$$

The SI unit of permeability is as mentioned above m^2, but in addition is the unit Darcy (D) common. Notice that 1 D = 0.987 μm^2, and that the Darcy fraction 1/1000 is used for millidarcy (mD).

Navier-Stoke equation can be used to describe the fluid flow behaviour in the pore network. While Darcys law solves permeability on a macroscopic level, the Navier-Stokes equation can be used on a microscopic level. For the simplest cases Navier-Stokes equation can be used directly and exact to find a solution. However, describing the pore surface of a complex porous medium is probably close to impossible. A quantum approach, the Navier-Stoke's capillaric tube model, simplifies and describes the phenomena at a larger scale, but does not provide an exact solution for complex mediums (Scheidegger, 1974). A simplified equation which assume steady, laminar flow in a cylindrical tube is expressed as the Hagen-Poiseuille equation,

$$Q = \frac{\pi R^4 \Delta p}{8 \mu L} \tag{2.11}$$

where R is tube radius, L is the tube's length and Δp is the pressure drop in the tube.

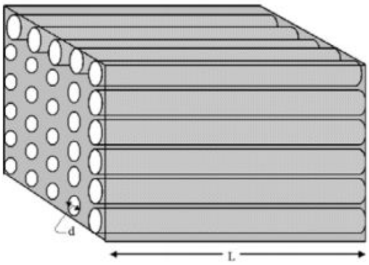

Figure 2.1.4. Model of capillaric tube model with bundle of straight, circular tubes. From Nordahl (2004).

A bundle of n equal tubes per unit cross area with a diameter d and length L (Fig. 2.1.4) can than be expressed as

$$q = \frac{n\pi d^4}{128\mu} * \frac{\Delta p}{L}, \tag{2.12}$$

where q is the specific discharge (flow per unit area). From this model porosity is found as $\phi = n\pi d^2/4$ and permeability for a bundle of tubes is derived compared with Darcy's law as

$$k = \phi * \frac{d^2}{32}. \tag{2.13}$$

Instead of using fixed diameters of the capillary tubes it is possible to use the hydraulic radius theory and Kozeny-Carman equation (Carman, 1937). In this case the tubes are modelled as a set of channels with equal length, but variable cross-section. This method also introduces the arbitrary factor tortuosity ($\tau = \mathrm{L}/L_T$), which gives flexibility to the length of the tubes, where L_T is the true length of the tube.

The Kozeny-Carman equation solves the Navier-Stokes equation simultaneously for all the channels and permeability becomes

$$k = c\frac{\frac{\phi^3}{(1-\phi)^2}}{S_s^2}. \tag{2.14}$$

S_s is the specific surface area pf the solid (eq.(2.6)), and c is the Kozeny constant. The constant c can also be expressed as $1/\tau^2 c_0$. For spherical grains of equal diameter d be written as

$$k = c\frac{d^2}{36} * \frac{\phi^3}{(1-\phi)^2}. \tag{2.15}$$

This method works well in well sorted sandstones, but not for mediums with high or low porosity values. The method also neglects the diameter changes between pores and pore throats, additionally the tortuosity coefficient is challenging to interpret physically and measure experimentally (Scheidegger, 1974).

In summation, permeability is more challenging to define than porosity. Mainly because all the model equations above ignore or simplify some geometrical aspects of permeability in porous medium. Likewise some of the geometrical parameters that are included in the equations are difficult to measure experimentally. However, by using the continuum approach can the permeability parameter be represented from a microscopic level to a macroscopic level, which can give a more nuanced interpretation of the whole medium.

2.1.4 Additivity

The properties describing a porous medium are generally divided into two types. The first type is called *extensive* properties and are dependent on the quantity of the porous material, e.g. mass and energy. The other type, *intensive* properties, denote concentrations or intensities of mass or energy. This parameter is independent of the quantity or shape of the porous media, e.g. temperature, density, pressure, porosity and permeability (Nordahl, 2004).

A distinctive difference between extensive and intensive properties were discussed by Narasimhan (1983). He found that only extensive properties are additive, while intensive properties are not. Although, by using a capacity function he argued that intensive properties could be transformed into extensive properties. Since porosity is a volume normalised parameter where the capacity function is unity, it is regarded as an additive property. Generally, the concept of REV can be used to give physical meaningful averaging of intensive properties (Hassanizadeh and Gray, 1983).

Additivity involves a mathematical function in which a property can be expressed as a weighted sum of some independent variable or variables (Ringrose and Bentley, 2015). *Additive* properties are independent on the spatial distribution of the different components, and represent a scalar value. They are simple to upscale analytically by a volume average equation (arithmetic average). *Non-additive* properties on the other hand is dependent on the spatial distribution of the different components and are represented by a tensor or vector. In order to upscale these properties is a fine scale explicit model is used.

Most measuring devices only measures in the finite domain and the result is given as the average of the measured properties over the measured area. It is therefore important to know that these data are represented correctly statistically. The average porosity is easier to define due to its additive property compared to the average permeability as a non-additive property.

2.2 Sedimentological factors controlling porosity and permeability

The previous section reviewed some of the basic theoretical concepts of porosity and permeability in a conceptual porous media. Most reservoirs are heterogeneous and anisotropic in nature (Chap.2.1.1). In this thesis a reservoir is synonym with a siliciclastic hydrocarbon reservoir rock, which means that the focus is on sandstone reservoirs. Carbonate reservoirs are reviewed in detail in e.g. Lucia (2007); Pöppelreiter et al. (2008).

There is a strong relation between the depositional process and the porosity and permeability anisotropy in sedimentary structures. Anisotropy of petrophysical properties occur in the smallest scale from grain shape, size and arrangement in the solid matrix, to larger scaled lamina and bedding structures. All of these different scaled anisotropies affects the measured porosity and permeability in a reservoir unit. Providing a detailed description of sedimentary structures and typical depositional environments is outside the scope of this thesis, however these topics are well described in most textbooks about sedimentology (e.g. Allen (1982a,b); Boggs (2011)). The intention of this chapter is to provide a general overview over petrophysical variability in stratified deposits.

2.2.1 Texture and fabric

Texture characterises the individual grains and the spatial arrangement of an aggregate of grains. Individual grains can be described by parameters as grain size and grain shape. Grain size and sorting have been linked to specific depositional environment (Middleton, 1976; Sun et al., 2002), although grain size is probably more dependent on depositional processes and not particular environments.

Natural occurring grains are generally complex with irregular surfaces and individually they are not simple to express exactly (as discussed in 2.1.1). Sedimentary grains can however, be characterise by the independent properties; form, roundness and surface texture (see Barrett (1980) for review of quantitative measurement methods).

Fabric characterises the orientation and packing of grain aggregates. Grains with a non-spherical and angular shape are prone to have a looser packing in sediments because they have more contact points between the grains (Atkins and McBride, 1992). The influence of fabric on the petrophysical properties permeability and porosity have been studied extensively (e.g. Fraser (1935); Pryor (1973)). Beard and Weyl (1973) found that grain size and sorting were more influential parameters than fabric and grain shape. Porosity was found independent of grain size, but decreases with decreasing sorting. Permeability was found dependent on both grain size and sorting. In poorly sorted sediments, finer grained materials can block the pore throats which decreases the permeability. The figure 2.2.1 illustrates the relationship between grain size and sorting for porosity and permeability respectively.

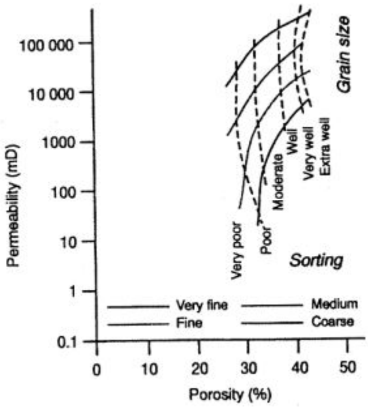

Figure 2.2.1. Grain size and sorting as a function of porosity and permeability. From Brayshaw et al. (1996).

In stratified sediments the burial depth is an important factor as it affects the pacing of the sediments by compaction. The studies performed by Ramm (1992) and Ramm and Bjørlykke (1994) on data from the Norwegian Continental Shelf, found that sandstone porosity was mainly affected by initial mineralogical and textural composition, but that burial history, pressure and temperature variations account for some porosity variations. They found that porosity for well sorted sandstone could differ from an initial 45-40% at surface, down to values of 5-10% at onset depth of metamorphism (6-8 km). General porosity values encountered in sandstone at reservoir depth range from 40-0% and permeability values range from 10000-0.001 mD (Brensdal and Halvorsen, 1992; Ringrose and Bentley, 2015).

2.2.2 Sedimentary structures

Jensen et al. (1996) states that clastic sediments are rarely uniform in lithology, grain size, cementation, and textural features. While fabric describes microscopic (∼mm) features, sedimentary structures describe structural features on macroscopic (cm-m's) scale.

Primary sedimentary structures are formed during or shortly after deposition (Reineck and Singh, 1980). Sedimentary structures can be formed as a result of grain size sorting and spatial arrangement in homogeneous lithologies or in combination with more than one lithology. Figure 2.2.2 illustrates how several lamina ($<$ 1 cm thick) layers with a specific internal structure can form complex bedform ($>$ 1 cm thick) structures (Ringrose et al., 1993). A particularly interesting property of sedimentary structures is that they can behave as flow boundaries. As can be seen from the figure, the sedimentary boundaries appears both on a small scale between the laminasets and between the separate bed units. Primary sedimentary structures are strongly dependent on depositional process and environment (e.g. Allen (1982a,b)), for instance the heterolithic bedding illustrated in figure 2.2.2 is typical for tidal influenced environments (Reineck and Singh, 1980).

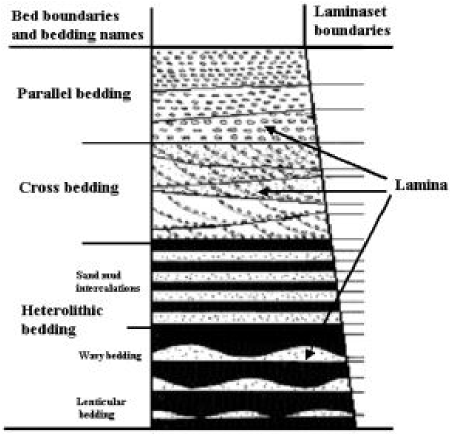

Figure 2.2.2. Illustration of sedimentary units. From Nordahl (2004).

Concerning heterolithic bedding, the volume of shale or mudstone reduces the porosity of the sandstone. Dispersed shale resides in the pore space and substantially reduces the total porosity (see effective porosity in chap. 2.1.2). Figure 2.2.3 illustrates three types of shale distribution found in porous media. Notice how laminated shale occupies both the matrix and pore space because of the alternation between sand and shale.

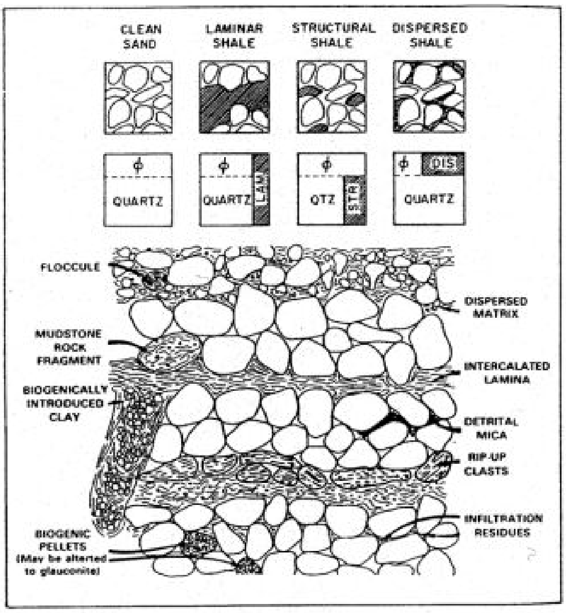
CLEAN SAND
LAMINAR SHALE
STRUCTURAL SHALE
DISPERSED SHALE
ϕ
QUARTZ
ϕ
QUARTZ
LAM
ϕ
QTZ
STR
ϕ
DIS
QUARTZ
FLOCCULE
MUDSTONE ROCK FRAGMENT
BIOGENICALLY INTRODUCED CLAY
BIOGENIC PELLETS (May be altered to glauconite)
DISPERSED MATRIX
INTERCALATED LAMINA
DETRITAL MICA
RIP-UP CLASTS
INFILTRATION RESIDUES

Figure 2.2.3. Illustration of how shale effects the porosity in sandstone. From Dewan (1983).

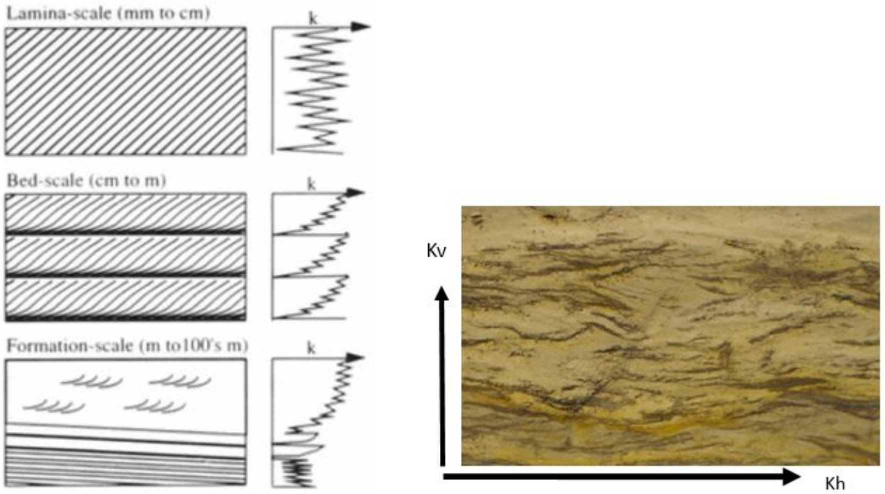
Lamina-scale (mm to cm)
k
Bed-scale (cm to m)
k
Formation-scale (m to100's m)
k
Kv
Kh

Figure 2.2.4. A (left): Scale effect on permeability; lamina-, bed-, and formation-scale (Ringrose et al., 1993). B (right): Example of vertical and horizontal permeability differences in flaser bedded sandstone, scale ~30x25 cm.

Several studies have verified that sedimentary structures have an effect on petrophysical properties, particularly on permeability (e.g. Brayshaw et al. (1996); Gibbons et al. (1993)). Both Ringrose et al. (1993) and Jensen et al. (1996) assessed the effect of permeability property at different unit scales. Figure 2.2.4A) shows that the permeability (k) changes in lamina sized beds are more drastic than at bed-scale and again more drastic than at formation-scale. However, lamina scaled anisotropy is more challenging to measure directly than overall trends (Brensdal and Halvorsen, 1992). Permeability is dependent on spatial distribution, therefore it is meaningful to divide the property in horizontal and vertical direction. Anisotropy in the vertical plane tend to be larger than in the horizontal plane, because sedimentary systems commonly are strongly layered (Ringrose and Bentley, 2015). Figure 2.2.4B is an example of how a sedimentary structure, e.g. flaser bedding, can effect the permeability. In vertical direction the mud drapes will to some degree obstruct the flow, while the sandstone can have good connectivity in the horizontal direction. In this case the horizontal permeability (k_h) is larger than the vertical permeability (k_v).

In addition to primary structures, sedimentary structures can be divided into secondary, organic and inorganic sedimentary structures (Reineck and Singh, 1980). Organic (living organisms present during deposition) and inorganic (e.g. gravity effects) sediment structures can drastically alter the primary structure. Secondary sedimentary structures are formed some time after sedimentation and includes amongst others diagenesis and bioturbation. Diagenesis can alter the original fabric of the deposition and give secondary porosity. Secondary porosity can present as vuggy, fractures and dissolution altering the intergranular porosity (e.g. Lucia (2007)). In clastic sediments it is unusual that diagenesis completely obscure the primary fabric (Ringrose and Bentley, 2015), however it can locally increase heterogeneity (Pyrcz and Deutsch, 2014). Unfilled fractures however, both on a microscopic and a macroscopic scale, will reduce the resistance of fluid flow and increase the permeability through the deposition.

2.3 Estimation of petrophysical properties

So far in the thesis the main topic has been core data. Chapter 2.1 briefly describes how petrophysical data is obtained from core samples. The size of the core samples is small compared to the entire reservoir. Core samples can be biased sampled with respect to the sedimentary structure, as it would be unknown whether the sample is representative for the reservoir or just a local abnormality. Due to the size of the sample, it is possible that lamina textured anisotropy can be oversampled compared to the large scaled elements in the geological length scale, e.g. channels. How close the specimens are sampled in the core is also decisive for a representative result.

The distance between each of the wells in a petroleum field are commonly in the kilometre range, usually several kilometres. Each well here represent a small, sampled area with reservoir information. On the other hand the petrophysical properties and lithology for the rest of the field, can be found either by the "best guess" method or by statistical estimation. The author of this thesis strongly recommends the latter approach.

The estimation method used later in this thesis is Kriging. In order to discuss this method key elements such as upscaling and the variogram model must be defined. Chapter 2.3.4 discuss briefly Kriging as an algorithm choice in reservoir modelling.

2.3.1 Upscaling

The term *upscaling* has been used previously without any closer explanation. It refers to procedures where the petrophysical property is measured for a small support volume and then averaged to represent an larger volume (e.g. from core plug to wireline tool resolution) The volume of additive properties, like porosity, can simply be averaged by arithmetic averaging (Nordahl, 2004; Nordahl and Ringrose, 2008). In other words, if the porosity value for all the cells in a reservoir model is defined, the total reservoir porosity is precisely equal to the sum of the cell porosity divided by the number of cells (Ringrose and Bentley, 2015).

Non-additive properties do not follow the same rule as additive properties during upscaling and it is therefore necessary to realy on estimation. An averaged permeability do not equal upscaled (effective) permeability, due to the spatial distribution and boundary conditions that determines the larger support value (Nordahl, 2004). Effective permeability, in this case upscaled permeability, can be found either by deterministic, stochastic and heuristic estimation methods (Renard and De Marsily, 1997).

Nordahl (2004) reviewed and summarised the following main elements about the deterministic, stochastic and heuristic method. The deterministic method assumes that the permeability distribution in space is known. The stochastic method assume random distribution as a probability density function (pdf) of space. The heuristic method uses rules (e.g. weighting and power average) to calculate plausible effective permeabilities. Each of the methods mentioned above contains several different approaches that will not be discussed in detail here.

2.3.2 Variogram

In order to find a distribution model for the entire reservoir model from the upscaled data, the "missing" data points between the wells can be interpolated or in some cases extrapolated (Caers, 2011). However, there is a spatial correlation between the distributions of non-additive data that needs to be addressed.

The degree of correlation in the data set can either be found by the empirical correlation function or variogram analysis. The correlation function characterise the dependency of values within a data set. The correlation coefficients measure the dependency between two parameters by comparing how far a pair of values (x,y), deviates from a straight line function (Ringrose and Bentley, 2015). However, the correlation coefficients do not reflect the spatial variation within the values.

Caers (2011) states that the variogram method is typically the preferred method by geostatisticians. The methods popularity is probably largely due to its ability to express spatial variation of parameters, but also because it is a simple and quick method that can be viewed graphically.

The variogram differentiates the value between pairs of data points and find the distance between those two points. The numerical expression is an averaged squared difference and is most simply expressed as

$$2\gamma = (1/N)\sum(z_i - z_j)^2, \tag{2.16}$$

where z_i and z_j are pairs of points in the dataset and N is the number of data points. By a simple rearranging of equation (2.16) can γ be expressed as

$$\gamma = (1/2N)\sum(z_i - z_j)^2. \tag{2.17}$$

This equation is the semivariogram function and *semi* here refers to the half of the variogram function. However, the terms semi- and variogram can be used interchangeably in the literature. The semivariogram function can be calculated for all pairs of data points in a data set, regardless of the spatial distance or spread between the data points.

The more formal definition of semi-variance can be expressed as

$$\gamma(h) = \frac{1}{2}E[Z(x_i + h) - Z(x_i)]^2, \tag{2.18}$$

where E is the mean (expectation), $Z(x)$ is the value of a point in space and $Z(x+h)$ is the value at a separation distance of h (the lag).

The function in eq. (2.18) is a stochastic function with two stochastic variables of Z(x). Inherently the variogram function assumes that a mean $E(Z(x)) = \mu(x)$ and the variance of Z(x) exists. This assumption yields three realisations with coinciding constraints referred to as strong (strict), weak (second order) and intrinsic stationarity.

The experimental variogram, in literature sometimes just referred to as semivariogram, is used to find the spatial variation with respect to one specific direction. The equation for the experimental variogram is given as

$$\gamma^*(h) = \frac{1}{2N(h)}\sum[z(x_i + h) - z(x_i)]^2. \tag{2.19}$$

The results of both the theoretical and the experimental variogram can be plotted graphically. When a trend line is fitted through the points the plot is referred to as a *semivariogram model*, as shown in Fig. 2.3.1. The expected shape of a semivariogram model is an increased γ with an increasing h. The standard semivariogram models are typically fitted by Gaussian, spherical or exponential model trend lines.

Figure 2.3.1 also visualise the three defining features of a semivariogram model. After a certain distance h, the distance between the points in the compared data pairs are so large that there is no influence between them. Statistically the covariance is equal to zero at this point. This influence distance is termed *range.* The corresponding γ value is at this point approximately equal to the variance. The influence distance along the y-axis is termed *sill.* The *nugget* is the extrapolated γ value at zero separation. The presence of a nugget is indicative of how good the spatial continuity is in the data. In the case of Fig. 2.3.1, the nugget effect indicates that there is a large variation of distances less than the sampling interval.

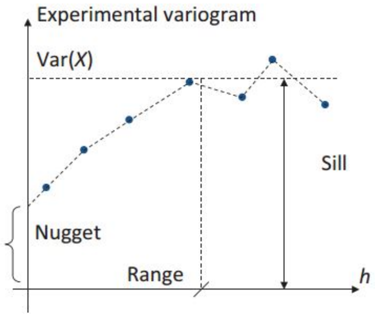

Figure 2.3.1. Experimental variogram plotted against semi-variance $\gamma(h)$ on the y-axis and distance h on the x-axis. From Caers (2011).

This short introduction to the variogram method is mainly inspired by Caers (2011); Pyrcz and Deutsch (2014); Ringrose and Bentley (2015). Numerous geostatistical textbooks describes this topic in greater detail with variating notations (e.g. Chilès and Delfiner (2009); Isaaks and Srivastava (1989); Journel and Huijbregts (1978); Lantuéjoul (2013)).

2.3.3 Kriging

Kriging was first developed and published by Matheron (1967), who named the method after his student Daniel Krige. The method was used originally to estimate ore grade in goldmines. Since then many variations and application areas of Kriging have arisen. A broad range of geostatistical textbook reviews this topic, particularly those who also reviews the Variogram (see Chap. 2.3.2). One of the better reviews of the topic were written by Jensen et al. (2000), which has a text that is easy to follow, but still sufficiently detailed.

Kriging is a basic estimation method that utilise the information from the semivariogram in order to estimate a petrophysical value for a untested spatial point. The variogram, as described earlier, correlates data pairs as function of distance. The *Kriging estimator* finds a set of wights for these points and uses them to estimate measurements for untested points as a function of the geographical arrangements of the samples.

A simple layout of an estimation problem is viewed in Fig. 2.3.2. From the data of three wells marked $X_{i=1,2,3}$ it is desirable to find a property, Z^*, at the unmeasured location, o. To do so, a common interpolation function can be used;

$$Z^* = \sum_{i=1}^{n} \lambda_i Z_i \tag{2.20}$$

where Z_i are known values from the locations X_i and λ_i is the *Kriging weight* for each well. These set of weights are determined by a Kriging estimator and should obtain a minimum expected variance given the available known data points. After that it is easy to calculate Z^* (Jensen et al., 2000; Ringrose and Bentley, 2015).

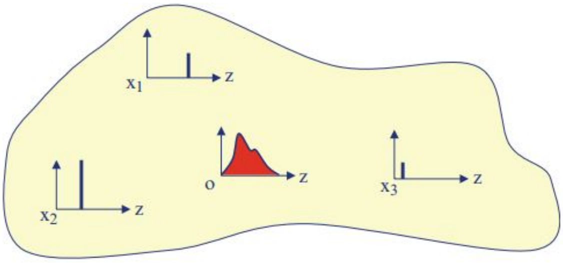

Figure 2.3.2. Illustration of the Kriging method, where o is the unmeasured location. From Ringrose and Bentley (2015).

The linearity of Z_i simplifies the equation (2.20) and results in an approximate normal (Gaussian) distribution of Z^* (marked red in figure 2.3.2). The example over is obviously also quite simplified with respect to how the Kriging weights are estimated.

There are several estimation methods within Kriging, where Simple Kriging (SK) is the mathematically simplest method. The method assumes that the mean value and distribution are known and that they are statistically stationary (Ringrose and Bentley (2015)).

The simplest problem is point-estimation. Under the assumption that the expected value, m, is known, a new variable $Z(x) = Y(x) + m$ with expected value equal to zero can be assumed. The equation (2.20) can then be rewritten as

$$Y^* = \sum_{i=1}^{n} \lambda_i Y_i. \tag{2.21}$$

Under the assumption that the equation is unbiased and the covariance $C(x_i, x_j)$

can be used to express the new equation system for simple kriging as

$$\sum_j \lambda_j C(x_i, x_j) = \bar{C}(x_i, x_j). \tag{2.22}$$

This equation system is solved as matrices with a $Ax = b$ form. The weights, λ, are then used in estimator;

$$\begin{aligned} Z^* = Y^* + m = \sum_i \lambda_i Y(x_i) + m = \sum_i \lambda_i [Z(x_i) - m] + m \\ = \sum_i \lambda_i Z(x_i) + m(1 - \sum_i \lambda_i) \end{aligned} \tag{2.23}$$

in order to find the estimated value for the unknown value Z^*. The point-estimation procedure reviewed here is a shortened version from Ellefmo and Larsen (2013), but e.g. Chilès and Delfiner (2009); Jensen et al. (2000); Mallet (2002) have much more detailed reviews.

Kriging is a method which gives the best linear unbiased estimate (BLUE), and in order to do that most applications of Kriging requires constrains. The Ordinary Kriging (OK) and Universal Kriging (UK) methods uses such constrains. Cokriging is a method that uses secondary data integration in the estimation. It means that the estimator retrieve information from more than one node (e.g. well) at each iteration during the estimation (Chilès and Delfiner, 2009; Jensen et al., 2000; Pyrcz and Deutsch, 2014).

2.3.4 Algorithm choice

At the end of this chapter follows a few words about the algorithm choice concerning geological reservoir modelling. The literature can be a bit confusing at this point as it exists quite a few methods, which are implemented in numerous computer softwares. Ringrose and Bentley (2015) have described the three distinct algorithm directions; Object modelling, Texture-based methods and Pixel-based methods. The majority of these methods are simulation methods, while Kriging is an estimator.

Object modelling uses, as the name indicates, objects or discrete shapes in three-dimensional space to model major elements or group of elements (e.g. Bridge and Leeder (1979); Deutsch and Wang (1996); Holden et al. (1998); Lantuéjoul (2013)).
Texture-based methods uses training images to recreate an desired architecture and the more recent developments include multi-point statistical (MPS) algorithms (e.g. Caers and Zhang (2004); Strebelle (2002)).

The umbrella term *Pixel-based methods* are those methods which uses a indicator variagram to create the model architecture by assigning the model element types on a cell-by-cell basis. The indicator variogram is just a variogram (Chap. 2.3.2) that has been adapted for discrete variables. Common approaches include Sequential

Indicator Simulation (SIS) (e.g. Journel and Alabert (1990); Seifert and Jensen (1999)), indicator Kriging and various facies trend or belt methods.

However, in the literature most Pixel-based methods, truncated Gaussian simulation, and often also MPS and Object-based models are referred to as just stochastic models. *Stochastic* indicates that the algorithm provides several plausible reservoir models (e.g. MacDonald and Aasen (1994); Srivastava (1994)). The Pixel-based method Indicator Kriging and other Kriging estimators on the other hand are *deterministic* methods, which provide just one model that honours the data deterministically.

Chapter 3

Geology of the study area

The Gullfaks field is located within an area of approximately 75 km^2, confined within block 34/10 in the Norwegian sector of the North Sea (Fig. 3.0.1) (Fossen and Hesthammer, 1998; Yielding et al., 1999). The field was discovered in 1978 and has been producing petroleum since 1986. Current licensees holders are Statoil Petroleum AS (operator), Petoro AS and OMV (Norge) AS (NPD-Factpages, 2015).

There are three major reservoir units in the Gullfaks field; the Brent Group (Middle Jurassic), the Cook Formation (Lower Jurassic), and the Statfjord Formation (Lower Jurassic–Upper Triassic) (Yielding et al., 1999). This thesis will only focus on the reservoir units of upper Brent Group. The main trapping mechanism is tilted falut blocks (domino blocks).

Overlaying the Brent GP is the Viking GP (Upper Jurassic) and the base Cretaceous (late Cimmerian) unconformity. The Viking GP is unevenly eroded through the field, up to 100m Upper Jurassic shales are preserved in the hengingwalls in the western part of the field (Fossen and Hesthammer, 1998). In this thesis the Upper Jurassic sediments will simply be addressed as the Viking GP. The base Cretaceous unconformity (BCU) represent a major time gap (up to 100 Ma) (Fossen and Hesthammer, 1998) and separate the Jurassic depositions from the overlaying Cretaceous deposits.

This chapter will serve as an introduction to the study area. Chapter 3.1 outlines the geological setting of the northern North Sea and the Gullfaks Field. Chapter 3.2 outline the sedimentology of the Upper Brent Group (Ness and Tarbert Formation).

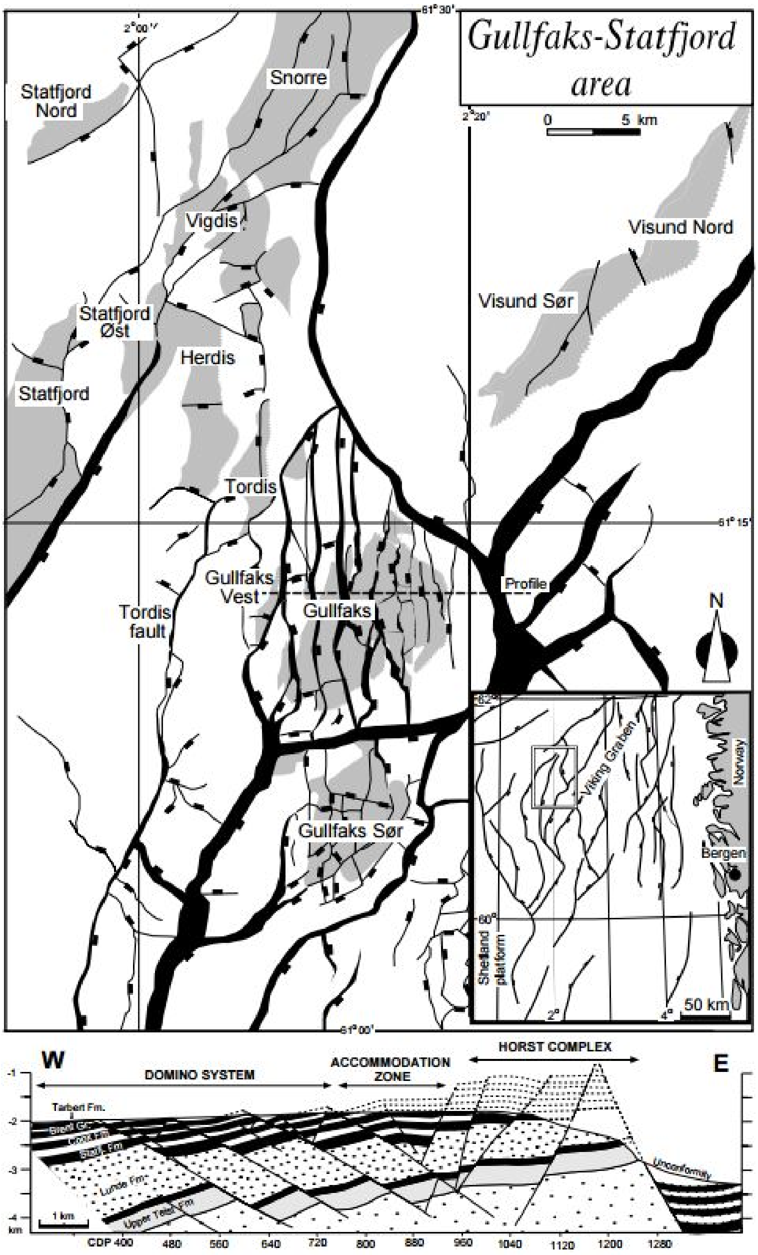
Gullfaks-Statfjord area
0 5 km
61° 30'
2° 00'
2° 20'
61° 15'
61° 00'
Statfjord Nord
Snorre
Vigdis
Statfjord Øst
Herdis
Statfjord
Tordis
Gullfaks Vest
Tordis fault
Gullfaks
Profile
Visund Nord
Visund Sør
Gullfaks Sør
N
62°
60°
Viking Graben
Norway
Bergen
Shetland platform
2°
4°
50 km
W
E
DOMINO SYSTEM
ACCOMMODATION ZONE
HORST COMPLEX
Tarbert Fm.
Brent Gr.
Cook Fm.
Statf. Fm.
Lunde Fm.
Upper Teist Fm.
Unconformity
1 km
-1
-2
-3
-4
km
CDP 400
480
560
640
720
800
880
960
1040
1120
1200
1280

Figure 3.0.1. Location map and East-West profile of the Gullfaks Field. From Fossen and Hesthammer (1998).

3.1 Geological setting

The Gullfaks field is located on the edge of the East Shetland Basin and western flank of the Viking Graben. As can be seen from Fig. 3.0.1, this entire area is strongly influenced by rifting events. A number of papers covering the structural geology of the Gullfaks field and regional area have been published (e.g. Folkestad et al. (2014); Fossen and Hesthammer (1998, 2000); Hesthammer and Fossen (1997); Rouby et al. (1996)).

3.1.1 Northern North Sea

The North Sea Basin has been described as an interior fracture basin (Kingston et al., 1983) and later as a failed rifts basin (Allen and Allen, 2013). According to Allen and Allen (2013) failed rifts are defined as basins where the rifting was aborted before the onset of seafloor spreading and the development of passive margins. During cooling, failed rifts widen and post-rift sedimentary rocks onlap the previous rift shoulders.

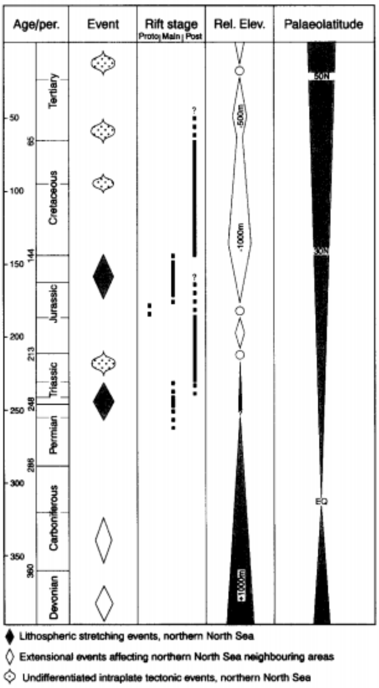

Figure 3.1.1. Schematic event chart of rifting events in the northern North Sea. From Nøttvedt et al. (1995)

The structural framework of faults and shear zones in the North Sea Basin was formed during the Caledonian orogeny and the subsequent extensional collapse of this orogenic belt in the Devonian (Folkestad et al., 2014; Fossen and Hesthammer, 1998). Two post-orogenic lithospheric rift episodes occurred, one during the Late Permian–Early Triassic (Permo-Triassic) and one during the Middle–Late Jurassic (see Fig.3.1.1) (Badley et al., 1988; Gabrielsen et al., 1990). The details regarding timing, extent and significance of the Permo-Triassic stretching and the dating of the Jurassic rifting have however been a matter of debate (e.g Færseth (1996); Gabrielsen et al. (1990); Roberts et al. (1995)).

During the Permian–Triassic phase of extension, large tilted fault-blocks bounded by master-faults with throws of the order of several kilometres formed in a 150 km wide, North–South oriented basin (Folkestad et al., 2014). During the Jurassic rifting, were the master-faults reactivated, in addition to new-formed faults in a N-S to a NNE-SSW direction (Fig. 3.1.2) (Færseth, 1996).

The Permo-Triassic event was significant

(Roberts et al., 1995), however the late Jurassic deformations are more obvious on commercial seismic and well data (Fossen and Hesthammer, 1998). The Middle Jurassic Brent GP is likely to be mainly influenced by the later Jurassic extension phase.

Allen and Allen (2013) suggest that there is a close relation between failed rift basins and their sedimentary structure. The sediments deposited before a rifting event are named pre-rift deposits, the deposits during a rifting event are called syn-rift and the deposits after a rifting event are referred to as post-rift deposits. These sediment deposition terms follow the three-stage rifting model (post-, syn- and post-rift), commonly used to describe the late Jurassic extension phase in the North Sea (e.g. Allen and Allen (2013); Folkestad et al. (2014); Nøttvedt et al. (1995)). According to Allen and Allen (2013), is it typically a sedimentary evolution from non-marine to shallow-marine in the syn-rift phase and deeper-marine in the post-rift phase. Where the Middle Jurassic Brent Group fit into this rift sedimentation-pattern has been a matter of discussion.

The Brent Group is deposited in a deltaic and shallow marine environment. In Aalenian time, the thermal uplift of the "Mid North Sea Dome" created a regional high at the triple junction between Viking Graben, Moray Firth and Central Graben (Fjellanger et al., 1996). The erosion form this uplifted area is probably the main sediment supply to the "Brent Delta", which progradated northward during a lifespan of about 2 million years (Helland-Hansen et al., 1992). Following the sedimentary evolution suggested by Allen and Allen (2013) the Brent GP can be syn-rift sediments. Ravnås et al. (1997) states that the Brent Delta might not have continued northward of 62° N because of the onset of the Jurassic rifting event. The sediment distribution might have been limited by increased fault activity and subsidence. Ravnås et al. (1997), including studies like Færseth (1996); Fjellanger et al. (1996); Helland-Hansen et al. (1992), therefore suggests that the syn-rift deposition began in the Bajocian Ness Formation (upper) [see Fig. 3.2.1 for stratigraphic column].

Alternatively it has also been suggested that the onset of syn-rift deposition started in Late Bajocian age with the Tarbert Formation (Davies et al., 2000; Johannessen et al., 1995; Løseth et al., 2009), or that the entire Brent GP was deposited before the late Jurassic extension phase (pre-rift) (Hampson et al., 2004; Jennette and Riley, 1996). The limited extent of the Brent Delta might just partially be influenced by the rifting event. It is possible that a relative sea-level rise and exhausted sediment supply due to an over-extended delta front (Helland-Hansen et al., 1992) were limiting, therefore the Brent GP could be pre-rift. Generally the early phases of the Jurassic rifting is poorly understood (Davies et al., 2000). Folkestad et al. (2014) found that the Gullfaks-Kvitebjørn megablock likely was influenced by rifting in the lowermost part of Ness Formation, while at the East Shetland Platform and Horda Platform the rifting probably was initiated later, during the Tarbert Formation.

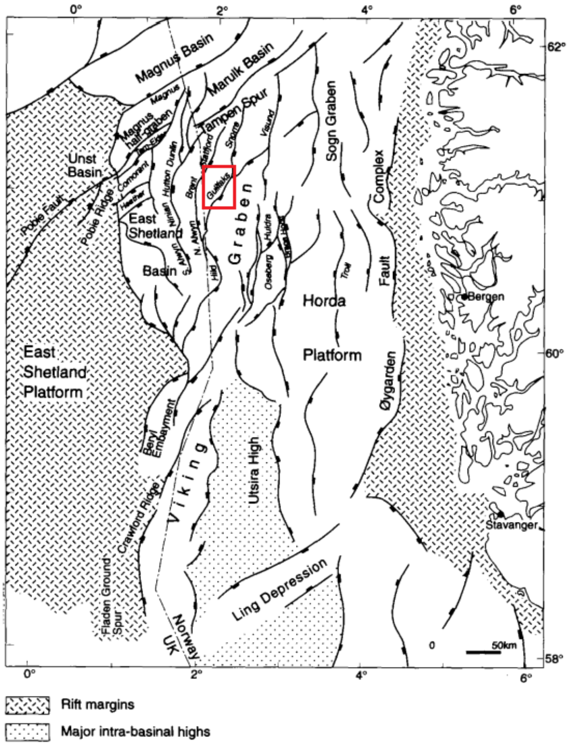
0°
2°
4°
6°
62°
60°
58°
Magnus Basin
Marulk Basin
Tampen Spur
Sogn Graben
Unst Basin
Magnus half-graben
Snorre
Visund
Statfjord
Gullfaks
Brent
Hutton
Dunlin
Cormorant
Heather
Ninian
Pobie Fault
Pobie Ridge
East Shetland Basin
N. Alwyn
S. Alwyn
Hild
Huldra
Oseberg
Graben
Complex
Fault
Troll
Horda
Platform
Bergen
East Shetland Platform
Beryl Embayment
Viking
Utsira High
Øygarden
Crawford Ridge
Fladen Ground Spur
Norway
UK
Ling Depression
Stavanger
0
50km
Rift margins
Major intra-basinal highs

Figure 3.1.2. Map of northern North Sea; rift zones formed during Permo-Triassic and Jurassic extension. Red rectangle marks the Gullfaks field. Modified from Færseth (1996).

3.1.2 Gullfaks

The NNE-SSW-trending Gullfaks fault block is a 10-25 km wide (first-order) fault block (A to C on Fig. 3.1.3), located on the western flank of the Viking Graben.

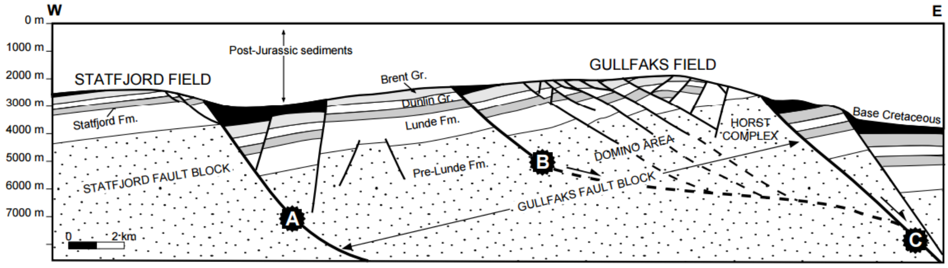
W
E
0 m
1000 m
2000 m
3000 m
4000 m
5000 m
6000 m
7000 m
Post-Jurassic sediments
STATFJORD FIELD
GULLFAKS FIELD
Brent Gr.
Dunlin Gr.
Statfjord Fm.
Lunde Fm.
Pre-Lunde Fm.
Base Cretaceous
HORST COMPLEX
DOMINO AREA
STATFJORD FAULT BLOCK
GULLFAKS FAULT BLOCK
A
B
C
0
2 km

Figure 3.1.3. East-West profile of the northern part of the Gullfaks Fault Block. Dashed fault lines where it is poor seismic resolution. From Rouby et al. (1996).

The Gullfaks Field occupies the eastern half of the Gullfaks fault block (B to C on Fig. 3.1.3) (Fossen and Hesthammer, 1998, 2000). A eastward, low-angle detachment fault (B on Fig. 3.1.3) underlying the Gullfaks reservoir has been interpreted from a deep reaching seismic survey (Fossen et al., 2000; Rouby et al., 1996). If present, Bale et al. (2008) suggest the detachment might have formed as a response to gravitational instability after the main fault pattern had been established during the Late-Jurassic.

The Gullfaks Field shows heavily internally deformation (Fossen and Hesthammer, 2000), which has been divided into three structural domains; the domino area, horst complex (Fig. 3.1.3) and the transitional graben system in between (Bale et al., 2008). Fossen and Hesthammer (1998) termed the transitional zone for an accommodation zone (Fig. 3.0.1).

The domino region is located in the western part of the field and constitutes the main part of the Gullfaks Field. This is where the main petroleum reservoirs are located (Bale et al., 2008). These domino blocks are generally N-S trending fault blocks (main faults) with a displacement in the range of 50-500 m, see Fig. 3.1.4 for development model. The block-bounding faults have a dip of 25-30° to the east and the sedimentary strata gently dip to the west with about 15° (Bale et al., 2008; Fossen and Hesthammer, 1998; Rouby et al., 1996).

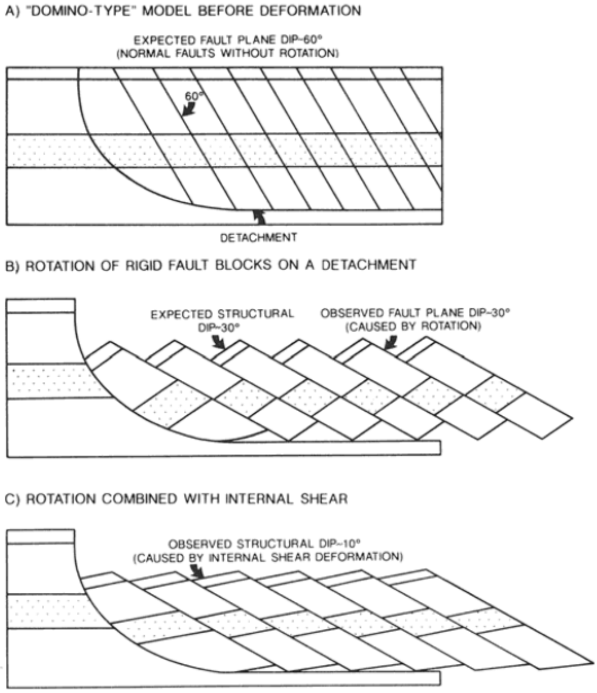
A) "DOMINO-TYPE" MODEL BEFORE DEFORMATION
EXPECTED FAULT PLANE DIP~60°
(NORMAL FAULTS WITHOUT ROTATION)
60°
DETACHMENT
B) ROTATION OF RIGID FAULT BLOCKS ON A DETACHMENT
EXPECTED STRUCTURAL DIP~30°
OBSERVED FAULT PLANE DIP~30°
(CAUSED BY ROTATION)
C) ROTATION COMBINED WITH INTERNAL SHEAR
OBSERVED STRUCTURAL DIP~10°
(CAUSED BY INTERNAL SHEAR DEFORMATION)

Figure 3.1.4. Structural development of domino faults in the western area of Gullfaks. From Petterson et al. (1990).

Minor faults within the N-S trending fault blocks have various orientation and are likely the result of readjustments within the fault blocks (Bale et al., 2008). Fossen and Hesthammer (2000) describe the main direction of the minor faults as (1) N-S-striking minor faults sub-parallel (synthetic) to the main faults; (2) E-W-striking minor faults; (3) diagonal; and (4) steep N-S-striking minor faults antithetic to the main faults. Fossen et al. (2000) suggest that the first category might be due to the detachment fault, which results in hangingwall collapse some places. Type (2) and (3) are related to internal block deformation, while type (4) is interpreted to be adjustment structures related to block-boundary conditions (Fossen and Hesthammer, 2000). As pointed out by Fossen and Rørnes (1996) the main faults are a direct result of the Jurassic extension phase, while the minor faults are largely due to adjustment and extensional collapse.

The transitional accommodation zone in the central part of the field is significant different from the horst and domino zones. It has a graben structure that can be characterised as a collapsed anticline with a western-dipping western limb and a subhorizontal to gently east-dipping eastern limb (Fossen and Hesthammer, 1998). Sæland and Simpson (1982) interpreted the structure as the result of a "keystone" collapse.

The eastern part of the field have a horst complex structure, which is considerably steeper then those in the domino area. The dips are both east- and west-dipping (about 60-70°) and the sedimentary strata is almost planar (Fossen and Hesthammer, 1998). The central and eastern parts of the Gullfaks field were heavily eroded during the Cretaceous transgression (Bale et al., 2008; Petterson et al., 1990). Due to the uplift of the Statfjord formation, the Brent and Cook reservoirs have been eroded away in the eastern part of the field (Petterson et al., 1990).

3.2 Lithological description of selected interval

The Middle Jurassic Brent GP consists of the Broom, Rannoch, Etive, Ness and Tarbert formation (from oldest to youngest, see Fig.3.2.1). Only the upper Brent, Ness and Tarbert formation, is characterised in detail here. The depth of the Brent GP varies through the Gullfaks field, but the top of the group is located from depth 1800 to 2000m. The field is well explored, according to the NPD-Factpages (2015) there are 28 exploration wells and numerous development wells drilled into the Gullfaks field.

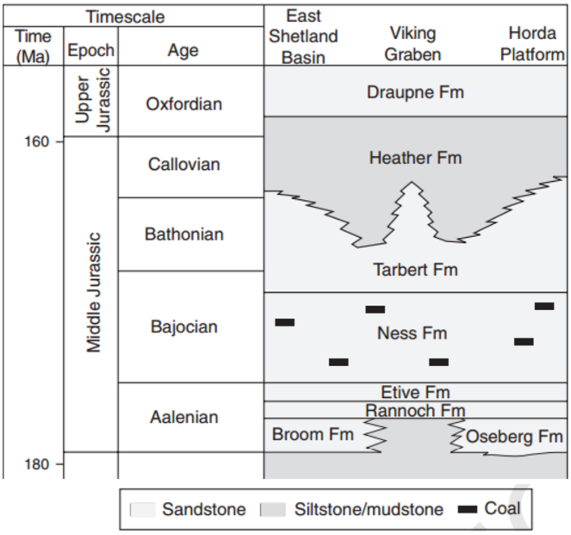
Timescale
Time (Ma)
Epoch
Age
East Shetland Basin
Viking Graben
Horda Platform
Upper Jurassic
Oxfordian
Draupne Fm
160
Callovian
Heather Fm
Bathonian
Middle Jurassic
Tarbert Fm
Bajocian
Ness Fm
Aalenian
Etive Fm
Rannoch Fm
Broom Fm
Oseberg Fm
180
Sandstone
Siltstone/mudstone
Coal

Figure 3.2.1. Stratigraphic column from Middle to Upper Jurassic. Modified from Husmo et al. (2003).

3.2.1 Ness Formation

A general description of the Ness formation is given by Richards et al. (1993), as heterolithic with interbedded siltstone, sand, mudstone and coal. The sedimentological structure of the lower sandstones are seen as thin bedded, parallel laminated, ripple laminated, or hummocky cross-laminated. The upper sandstones are thicker (up to 5m) than the lower unit, and have cross-bedding, ripple lamination and parallel lamination. Additionally bioturbation and micaceous sand occur. The mudstone are structureless and contain plant fragments and root traces. Coals in the centimetre scale are found throughout the formation, particularly in the lower part.

At the Gullfaks field, the Ness formation shows a general thinning from south to north (135 to 82 m) (Olaussen et al., 1992). Figure 3.2.2 gives an example of how the Ness formation in cores looks at the upper part and the lower part of the filed. Petterson et al. (1990) notes the base Ness formation at the first occurrence of a coal bed over the clan, Etive sands. A three-fold subdivision of the Ness formation has been used to describe the formation (Richards et al., 1993), where amongst others Petterson et al. (1990) and Olaussen et al. (1992) have focused on the Gullfaks field.

The lowermost unit, N-1, is from 5 to 35 m in thickness. It has some minor ripple-laminated and crossstratified medium- to fine- and sporadically coarsegrained sandstones. Mainly the unit is heterolithic with laminated clay- and siltstones, dominated by coals, root zones and some siderite nudles.

The N-2 unit range from 34 to 56 m in thickness. It is dominated by three to five coarsening-upward sequences grading from claystone to micaceous fine- to medium-grained sandstones. The sandstones are ripple-laminated, locally with mudstone drapes. These sands have a good reservoir quality (Olaussen et al., 1992).

According to Petterson et al. (1990) the common occurrence of soil profiles with siderite is typical for the N-3 unit. The N-3 unit comprises thick coal beds, mudstones, sandstones, and coarsening- as well as fining-upward sequences (Olaussen et al., 1992).

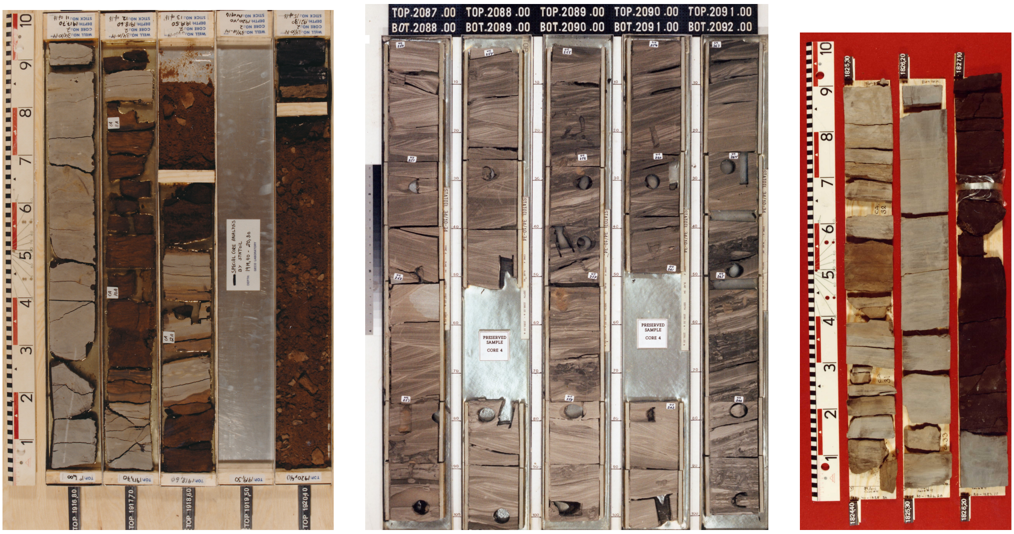
TOP.2087 .00
BOT.2088 .00
TOP.2088 .00
BOT.2089 .00
TOP.2089 .00
BOT.2090 .00
TOP.2090 .00
BOT.2091 .00
TOP.2091 .00
BOT.2092 .00
PRESERVED SAMPLE CORE 4
PRESERVED SAMPLE CORE 4
TOP 1916.80
TOP 1917.70
TOP 1918.60
TOP 1919.50
TOP 1920.40
1824.40
1825.30
1826.20

Figure 3.2.2. Left: Upper Ness (N-3), well 34/10-14 at 1916-1921m, north-middle part of Gullfaks. Possible soil profile with coal beds. Middle: N-2, well 34/10-34 at 2087-2092m, Gullfaks west. Heterolithic, bayfill sandstone with small-scale hummocky stratification. Right: Lower Ness (N-1), well 34/10-1 at 1824-1827m, southern Gullfaks. Shows a crevasse spilled over a thick coal-mash layer. From NPD-Factpages (2015).

Interpretation

The depositional environment interpreted from the Ness formation by Olaussen et al. (1992) correlates relatively good with the interpretations done by Mjøs (2009) and Folkestad et al. (2014).

The lower Ness, N-1, lower delta plain environments containing swamp and lagoon deposits with crevasse splay and distributary channel sands. Middle Ness, N-2, represents bayfill, crevasse splays, and mouthbar deposits. Upper Ness, N-3, represent delta plain deposits with soil development, peat deposits, fluvial channels, and interchannel deposits (Olaussen et al., 1992). In figure 3.2.6 the stratigraphic column and the separation of the three units is shown.

The Ness facies tract has been interpreted as coastal plain deposits (Johannessen et al., 1995; Mjøs, 2009), while Olaussen et al. (1992) and Petterson et al. (1990) uses the term delta plain specific for Gullfaks. The bays at Gullfaks have probably been more protected than the more northern parts of the Tampen Spur area, leading to the development of lagoonal to palaeosol conditions. The upward coarsening sandstone sequences in N-2, represents interdistributary bay fill, which has good reservoir quality. Both the lower and upper part of the Ness formation have to some degree been influenced by fluvial channels. According to Petterson et al. (1990) the lower part have low-sinuosity distributary channels, which locally can be in connection with the underlying Etive Formation. The fluvial channels in N-3 are rarely, and only locally, in connection with N-2. Where the upper Ness is uneroded, it is a laterally persistent permeability barrier across the Gullfaks Field. The vertical permeability communication in the Ness formation is overall low, as it can be seen from Fig.3.2.3, compared to the other formations in the Brent Group.

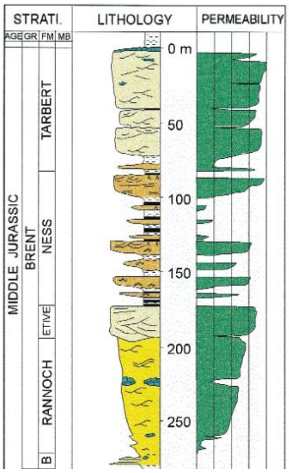

Figure 3.2.3. Stratigraphic and permeability column of the Brent Gp. "B" is the Broom Formation. Modified from Hesthammer and Fossen (1997).

3.2.2 Tarbert Formation

Richards et al. (1993) generally describe the Tarbert member as consisting of grey to brown, relatively massive fine to medium grained, locally calcite-cemented sandstone with subordinate thin siltstones, mudstones and coals. The formation is found over much of the East Shetland Basin north of about 60° 30'N, although locally it might be absent due to erosion. Eroded sections occur mostly in the crest of tilted fault-blocks. Helland-Hansen et al. (1992) recognises the bottom of the Tarbert Formation by the first appearance of shoreline sediments (deltafront or shoreface/foreshore) above the continental deposits of the Ness Formation.

The Tarbert formation at the Gullfaks field has also sustained erosion, where the formation is present locally in the western part of the field (the domino-area from chapter 3.1.2) (Petterson et al., 1990). Olaussen et al. (1992) describe the formation as up to 115 m thick, of stacked sandstone bodies with interbedded mudstones, siltstones, and thin, often extensive coal beds. Calcite cementation is common, particularly in the upper part of the formation. Figure 3.2.4 gives an example of how the lower Tarbert formation looks like in cores. Unfortunately is the NPD core-photo collection of the Tarbert formation at the Gullfaks field of poor quality.

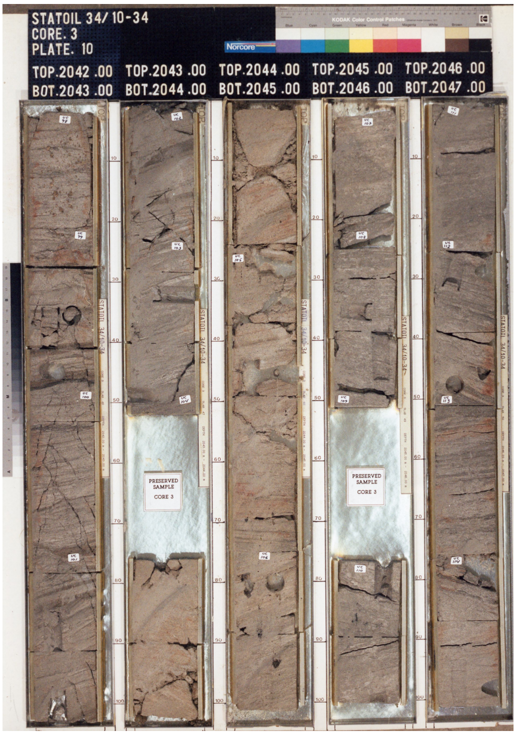
STATOIL 34/ 10-34
CORE. 3
PLATE. 10
Norcore
KODAK Color Control Patches
TOP.2042 .00
BOT.2043 .00
TOP.2043 .00
BOT.2044 .00
TOP.2044 .00
BOT.2045 .00
TOP.2045 .00
BOT.2046 .00
TOP.2046 .00
BOT.2047 .00
PRESERVED SAMPLE CORE 3
PRESERVED SAMPLE CORE 3

Figure 3.2.4. Lower Tarbert formation at well 34/10-34, depth 2042-2047m. Bioturbated, planar to low-angle laminated sandstone. From NPD-Factpages (2015).

Interpretation

The lower part of the Tarbert formation (T-1) at the Gullfaks field has been interpreted to have deposits associated with tidal flat and shoreface environment (Petterson et al., 1990), mainly backbarrier lagoonal, delta marsh, and mouth bar deposits (Olaussen et al., 1992). The lower unit represent a permeability barrier that covers most of the field (Petterson et al., 1990).

The upper unit (T-2) is interpreted to consist mainly of foreshore and shoreface sequences, probably of beach and barrier island origin (Olaussen et al., 1992). Thick clean sand with very good reservoir qualities are found locally (Petterson et al., 1990).

The Tarbert Formation at Gullfaks field is interpreted to be a shallow marine sandstone sequence deposited during a relative rise in sea level (Fig.3.2.6). The Tarbert Formation represents the retreating part of the Brent delta (Folkestad et al., 2014). The facies differentiation is expressed by the development of a wave-storm dominated shoreface facies tract during the progradational-dominated phase and a tidal bay-barrier complex facies tract during the succeeding aggradational phase (Mjøs, 2009).

The lateral facies variations have been affected by the fault activity in the area, as discussed in chapter 3.1. Folkestad et al. (2014) discussed that particularly the rotation of the Permo-Triassic fault-blocks might have given an asymmetric subsidence pattern along the coastline. The asymmetric subsidence could have led to the estuary development of high-subsidence and accommodation space in the hangingwall parts, while the footwall parts of the fault blocks would have been more wave-reworked and had less subsidence (e.g. Fig. 3.2.5).

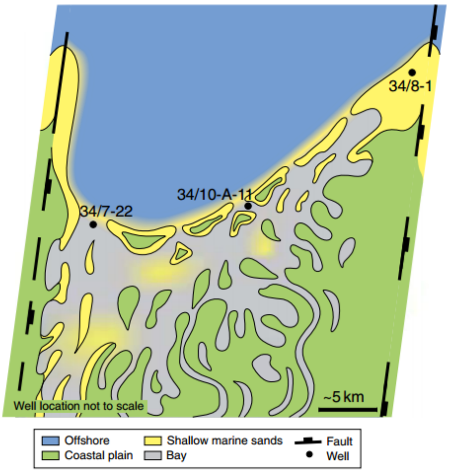

Figure 3.2.5. Illustration transgressive environment of Tarbert and Ness. 34/10-A-11 is a well in the Gullfaks field. Shoreline at the footwall area (34/8-1) extends further into the basin, whereas the hangingwall area (34/7-22) experienced transgression. From Folkestad et al. (2014).

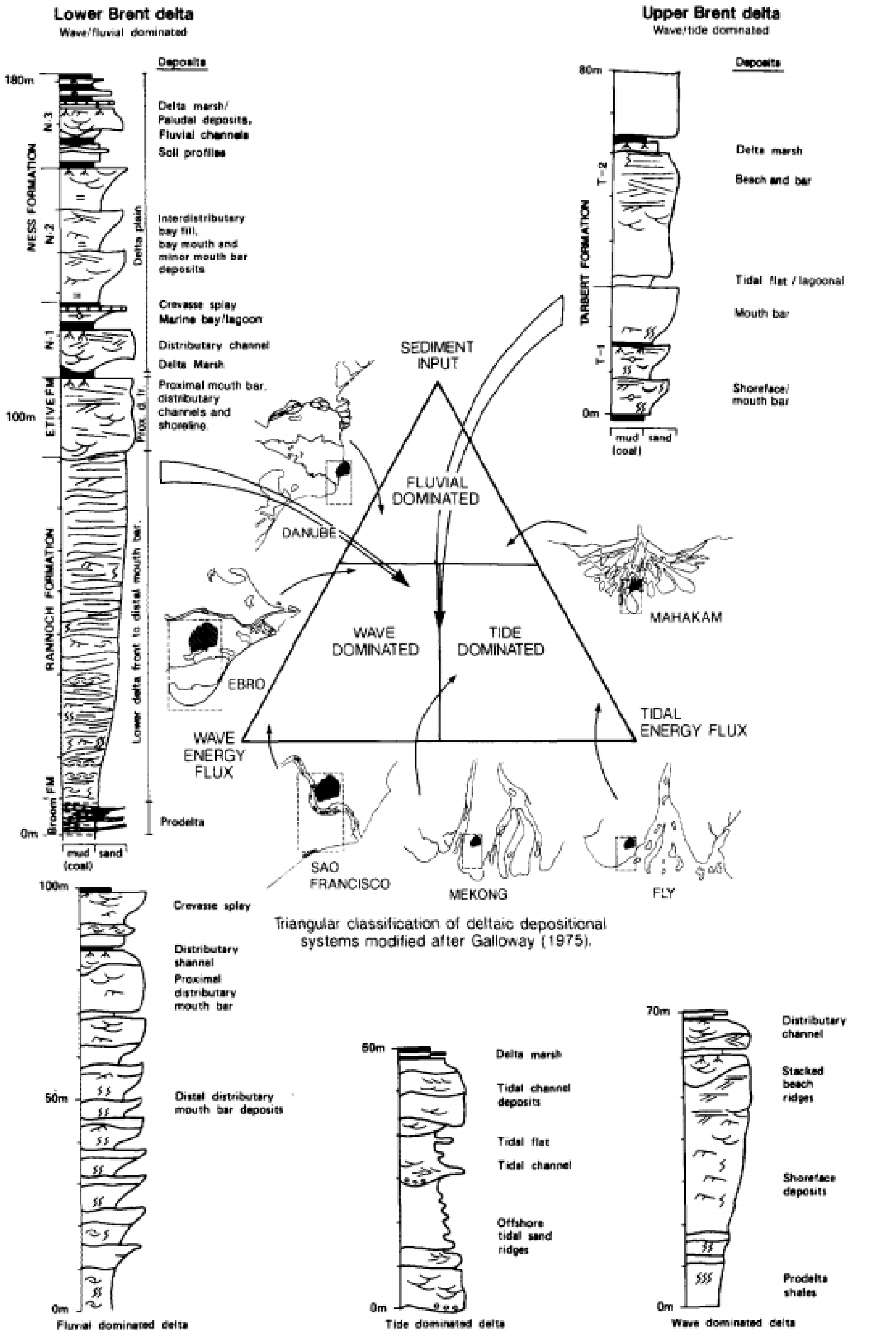
Lower Brent delta
Wave/fluvial dominated
Deposits
180m
100m
0m
NESS FORMATION
N-3
N-2
N-1
ETIVE FM
RANNOCH FORMATION
Broom FM
Delta plain
Prox. d. fr.
Lower delta front to distal mouth bar.
Delta marsh/ Paludal deposits, Fluvial channels Soil profiles
Interdistributary bay fill, bay mouth and minor mouth bar deposits
Crevasse splay
Marine bay/lagoon
Distributary channel
Delta Marsh
Proximal mouth bar, distributary channels and shoreline.
Prodelta
mud (coal)
sand
Upper Brent delta
Wave/tide dominated
Deposits
80m
0m
TARBERT FORMATION
T-2
T-1
Delta marsh
Beach and bar
Tidal flat / lagoonal
Mouth bar
Shoreface/ mouth bar
mud (coal)
sand
SEDIMENT INPUT
FLUVIAL DOMINATED
WAVE DOMINATED
TIDE DOMINATED
WAVE ENERGY FLUX
TIDAL ENERGY FLUX
DANUBE
EBRO
MAHAKAM
SAO FRANCISCO
MEKONG
FLY
Triangular classification of deltaic depositional systems modified after Galloway (1975).
100m
50m
0m
Crevasse splay
Distributary shannel
Proximal distributary mouth bar
Distal distributary mouth bar deposits
Fluvial dominated delta
60m
0m
Delta marsh
Tidal channel deposits
Tidal flat
Tidal channel
Offshore tidal sand ridges
Tide dominated delta
70m
0m
Distributary channel
Stacked beach ridges
Shoreface deposits
Prodelta shales
Wave dominated delta

Figure 3.2.6. Stratigraphic column of Brent GP with interpretations compared to resent deltaic depositional systems. From Olaussen et al. (1992).

Chapter 4

Conceptual Geological Model

A conceptual model can be described as a synthesis of the modeller's understanding of the reservoir based on the available data (Bjørlykke, 2010). A conceptual model can also be described as an environmental model with uncertainties (Refsgaard et al., 2006). Common for conceptual geological models is that they focus on (model)elements that are present in the data or expected in a specific environment. Faulting events were discussed in Chap. 3.1.

4.1 Morphology and sequence stratigraphy

The lithological descriptions and interpretation of the Ness and Tarbert in Chapter 3.2 is not very detailed. Few authors have reviewed the lithology of Gullfaks in detail, but rather focused on facies descriptions.

The description of the Ness formation is relatively unproblematic; the depositional environment can be interpreted as a wave and fluvial dominated delta, where the fluvial component is dominant. However, the interpretation of the Tarbert formation is a bit more unclear. The interpretation of Tarbert references to backbarrier lagoon and barrier island which are typical elements in an estuary marginal-marine environment. Olaussen et al. (1992) interpreted the Tarbert formation as a wave-tidal dominated delta, as it can be seen in Fig. 3.2.6.

Delta and estuary can be defined with alternating meaning in the literature, it will therefore be useful to define these concepts closer as they are used in this thesis. A delta is defined by Bhattacharya (2006) as; "*discrete shoreline protuberances formed where a river enters a standing body of water and supplies sediments more rapidly than they can be redistributed by basinal processes, such as tides and waves*" (p. 237). Indicating that all deltas are river-dominated and deltas are fundamentally regressive in nature. The major morphology elements of deltas consist of a terrestrial part strongly influenced by a fluvial environment and delta plains. The coastal area of the delta contains of the delta front and the lobes influenced by wave and potentially tidal forces (Fig. 4.1.1A). Idealised logs of fluvial, tidal and wave dominated delta is portraied in the lower part of Fig. 3.2.6. The major fluvial morphological elements are portrayed in Fig. 4.1.2 (see e.g. Bridge (2006); Bridge and Leeder (1979); Walker and Cant (1984)). An example of a major modern wave dominated delta is the Niger delta (Fig. 4.1.1B).

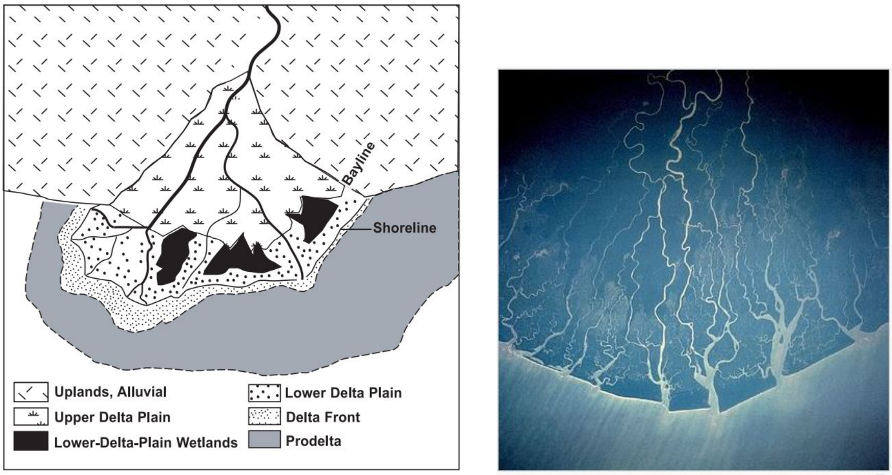
Bayline
Shoreline
Uplands, Alluvial
Upper Delta Plain
Lower-Delta-Plain Wetlands
Lower Delta Plain
Delta Front
Prodelta

Figure 4.1.1. A(Left): The major areal elements in a delta. From Bhattacharya (2006). B (Right): Niger delta, modern analogue of a wave dominated delta. Photo from NASA.

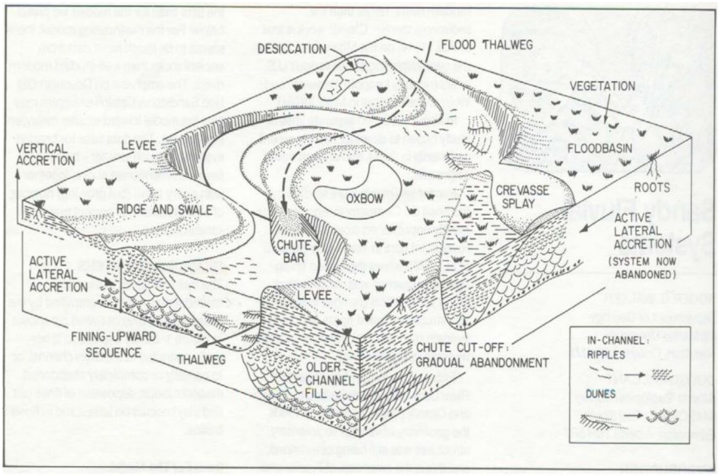
DESICCATION
FLOOD THALWEG
VEGETATION
VERTICAL ACCRETION
LEVEE
FLOODBASIN
ROOTS
RIDGE AND SWALE
OXBOW
CREVASSE SPLAY
ACTIVE LATERAL ACCRETION (SYSTEM NOW ABANDONED)
CHUTE BAR
ACTIVE LATERAL ACCRETION
LEVEE
FINING-UPWARD SEQUENCE
THALWEG
OLDER CHANNEL FILL
CHUTE CUT-OFF: GRADUAL ABANDONMENT
IN-CHANNEL: RIPPLES
DUNES

Figure 4.1.2. Morphological elements in a fluvial system. Here portrait as a block diagram of a meandering river system. From Walker and Cant (1984).

An estuary is defined by Dalrymple et al. (1992) as; "*the seaward portion of a drowned valley which receives sediment from both fluvial and marine sources, and which contains facies influenced by tide, and fluvial processes; the estuary is considered to extend from the landward limit of tidal facies at its head to the seaward limit of coastal facies at its mouth*" (p. 1132). Figure 4.1.3 shows the morphological elements in an idealised wave dominated estuary. Figure 4.1.4 gives a schematic overview of different marginal-marine environments with respect to transgressive and regressive systems.

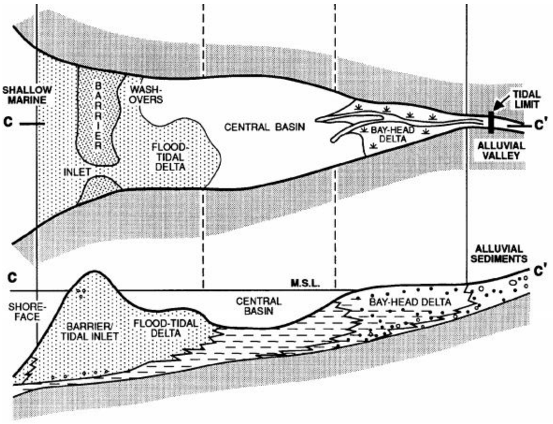
SHALLOW MARINE
C
BARRIER
WASH-OVERS
CENTRAL BASIN
FLOOD-TIDAL DELTA
INLET
BAY-HEAD DELTA
TIDAL LIMIT
C'
ALLUVIAL VALLEY
ALLUVIAL SEDIMENTS
C
M.S.L.
C'
SHORE-FACE
BARRIER/ TIDAL INLET
FLOOD-TIDAL DELTA
CENTRAL BASIN
BAY-HEAD DELTA

Figure 4.1.3. Morphological elements from a wave-dominated estuary in plain view and section. From Dalrymple et al. (1992).

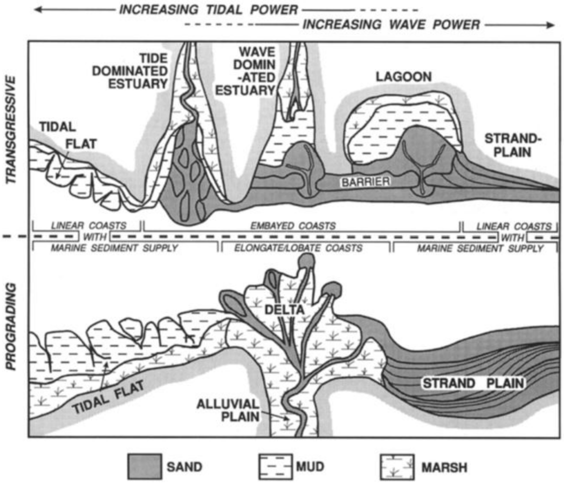
INCREASING TIDAL POWER
INCREASING WAVE POWER
TRANSGRESSIVE
TIDE DOMINATED ESTUARY
WAVE DOMIN -ATED ESTUARY
LAGOON
TIDAL FLAT
STRAND-PLAIN
BARRIER
LINEAR COASTS WITH MARINE SEDIMENT SUPPLY
EMBAYED COASTS
ELONGATE/LOBATE COASTS
LINEAR COASTS WITH MARINE SEDIMENT SUPPLY
PROGRADING
DELTA
TIDAL FLAT
ALLUVIAL PLAIN
STRAND PLAIN
SAND
MUD
MARSH

Figure 4.1.4. Marginal-marine environments, the transgressive estuary on top and the prograding/regressive delta below. From Boyd et al. (1992).

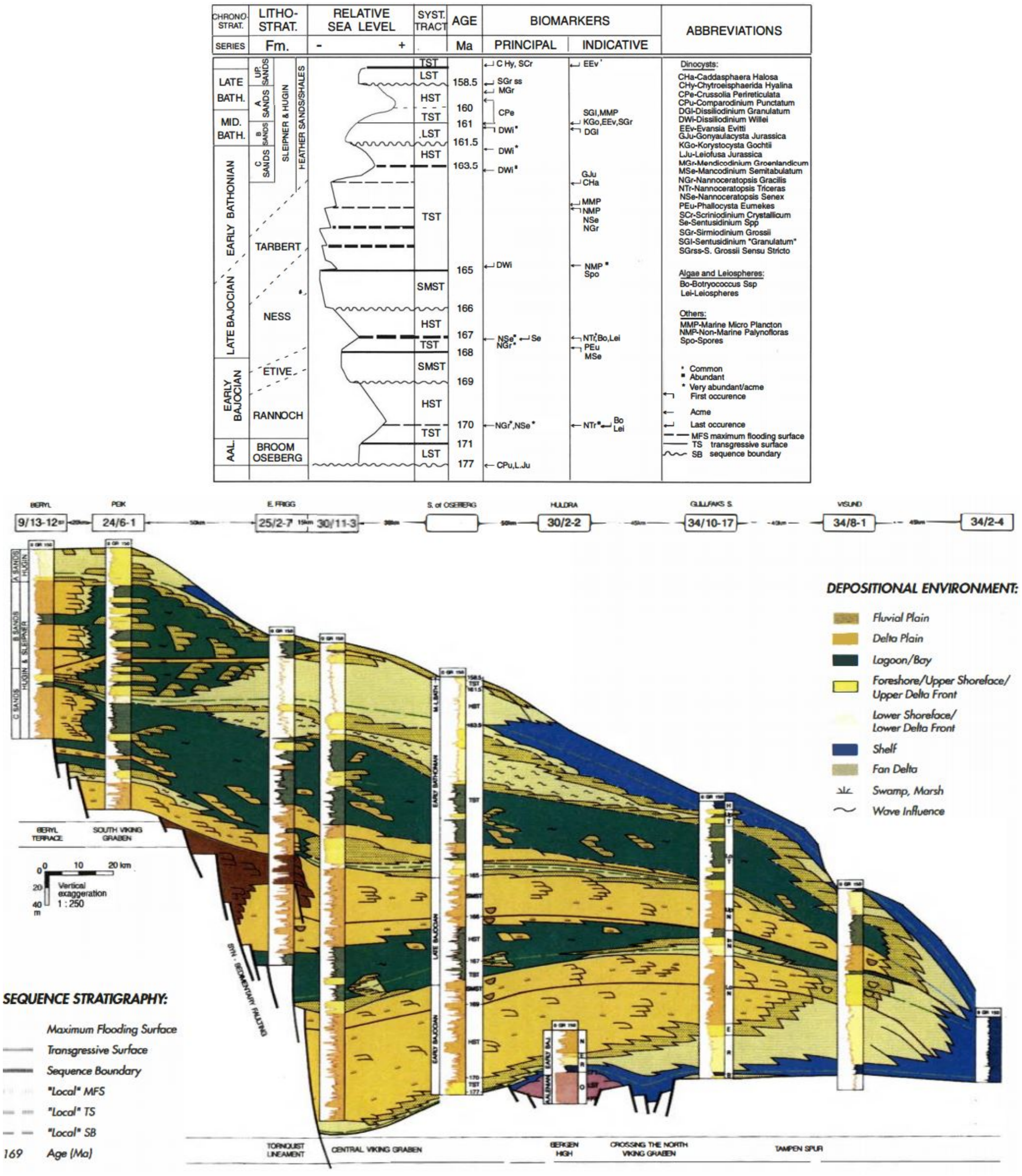

CHRONO-STRAT.
LITHO-STRAT.
RELATIVE SEA LEVEL
SYST. TRACT
AGE
BIOMARKERS
ABBREVIATIONS
SERIES
Fm.
Ma
PRINCIPAL
INDICATIVE
LATE BATH.
MID. BATH.
EARLY BATHONIAN
LATE BAJOCIAN
EARLY BAJOCIAN
AAL.
UP. SANDS
A SANDS
B SANDS
C SANDS
SLEIPNER & HUGIN
HEATHER SANDS/SHALES
TARBERT
NESS
ETIVE
RANNOCH
BROOM OSEBERG
TST
LST
HST
SMST
158.5
160
161
161.5
163.5
165
166
167
168
169
170
171
177
Dinocysts:
CHa-Caddasphaera Halosa
CHy-Chytroeisphaerida Hyalina
CPe-Crussolia Perireticulata
CPu-Comparodinium Punctatum
DGl-Dissiliodinium Granulatum
DWi-Dissiliodinium Willei
EEv-Evansia Evitti
GJu-Gonyaulacysta Jurassica
KGo-Korystocysta Gochtii
LJu-Leiofusa Jurassica
MGr-Mendicodinium Groenlandicum
MSe-Mancodinium Semitabulatum
NGr-Nannoceratopsis Gracilis
NTr-Nannoceratopsis Triceras
NSe-Nannoceratopsis Senex
PEu-Phallocysta Eumekes
SCr-Scriniodinium Crystallicum
Se-Sentusidinium Spp
SGr-Sirmiodinium Grossii
SGl-Sentusidinium "Granulatum"
SGrss-S. Grossii Sensu Stricto
Algae and Leiospheres:
Bo-Botryococcus Ssp
Lei-Leiospheres
Others:
MMP-Marine Micro Plancton
NMP-Non-Marine Palynofloras
Spo-Spores
Common
Abundant
Very abundant/acme
First occurence
Acme
Last occurence
MFS maximum flooding surface
TS transgressive surface
SB sequence boundary
BERYL
PEK
E. FRIGG
S. of OSEBERG
HULDRA
GULLFAKS S.
VISUND
9/13-12
24/6-1
25/2-7
30/11-3
30/2-2
34/10-17
34/8-1
34/2-4
DEPOSITIONAL ENVIRONMENT:
Fluvial Plain
Delta Plain
Lagoon/Bay
Foreshore/Upper Shoreface/ Upper Delta Front
Lower Shoreface/ Lower Delta Front
Shelf
Fan Delta
Swamp, Marsh
Wave Influence
BERYL TERRACE
SOUTH VIKING GRABEN
0 10 20 km
0 20 40 m
Vertical exaggeration 1 : 250
SEQUENCE STRATIGRAPHY:
Maximum Flooding Surface
Transgressive Surface
Sequence Boundary
"Local" MFS
"Local" TS
"Local" SB
169 Age (Ma)
SYN-SEDIMENTARY FAULTING
TORNQUIST LINEAMENT
CENTRAL VIKING GRABEN
BERGEN HIGH
CROSSING THE NORTH VIKING GRABEN
TAMPEN SPUR

Figure 4.1.5. A (Upper): Chart with biomarkers and system tracs Brent Group. B (Lower): S-N cross-section of the Brent and Vestland deltaic systems, well 34/10-17 is Gullfaks South. Abbreviations: HST - Highstand Systems Tract, TST - Transgressive Systems Tract, SMST - Shelf-Margin Systems Tract, LST - Lowstand Systems Tract. Formation names: H - Heather, T - Tarbert, N - Ness, E - Etive, R - Rannoch, B - Broom, O - Oseberg. From Fjellanger et al. (1996).

The Jurassic strata were deposited during a long-term global transgression that began in the Triassic and the entire first-order cycle lasted approximately 250 Ma (Hallam, 1977; Haq et al., 1987). As for the second order regressive and transgressive cycles, Graue et al. (1987) found that the Brent GP consist of three complete cycles.

Several articles discuss the sequence stratigraphy of the Brent GP, amongst others Davies et al. (2000); Fjellanger et al. (1996); Folkestad et al. (2014); Helland-Hansen et al. (1992); Mjøs (2009). It is a census amongst these authors that the Ness Formation entirely or mostly, belongs to the upper part of the progradational Brent delta and Tarbert belong to the retrogradational part of the delta. From Fig. 4.1.5 it can be seen that the Tarbert formation and partially the upper part of the Ness formation is marked in a Transgressive Systems Tract (TST), which would indicate a estuary dominated environment from the definitions above.

4.1.1 Mesaverde Group

The Mesaverde Group in Campanian, Colorado is a good outcrop analogue to the Brent Group both in size and in depositional environment, particularly to the Tampen Spur area of the North Sea (e.g. Doligez et al. (1999); Eschard et al. (1993); Fält et al. (1989)). Observing a fitting outcrop, and preferably modern analogues, gives geological inside into the field, and constitute an important element in developing a conceptual model. The outcrop study can help determine probable (unseen) structures and morphological elements that can be hard to obtain just from the field data.

The terrestrial, littoral and marine deposition of the Mesaverde Group constitute of a regressive and transgressive wedge of Campanian age. Eschard et al. (1993) have correlated the costal plain series of the Menefee formation with the Ness formation. Eschard et al. found that the Menefee formation had more fluvial depositions than the Tampen Spur area, which shows extensive lagoon deposits. The Cliff house sandstone correlates well with the Tampen Spur Tarbert Formation. The Cliff house sandstone was interpreted as shoreface sandstones deposited under storm-dominated conditions with a landward stepping stacking pattern (Fig. 4.1.6).

From the observations of the Mesaverde group it was deducted that transgression accompanies a base-level rise in the coastal plain settings, which for the Ness formation indicates that sandy lagoonal deposits are time-equivalent with transgression events. The landward stepping of littoral genetic units in the Tarbert Formation induce a widespread mudstone or low permeability layers that acts as vertical permeability barriers within the reservoir.

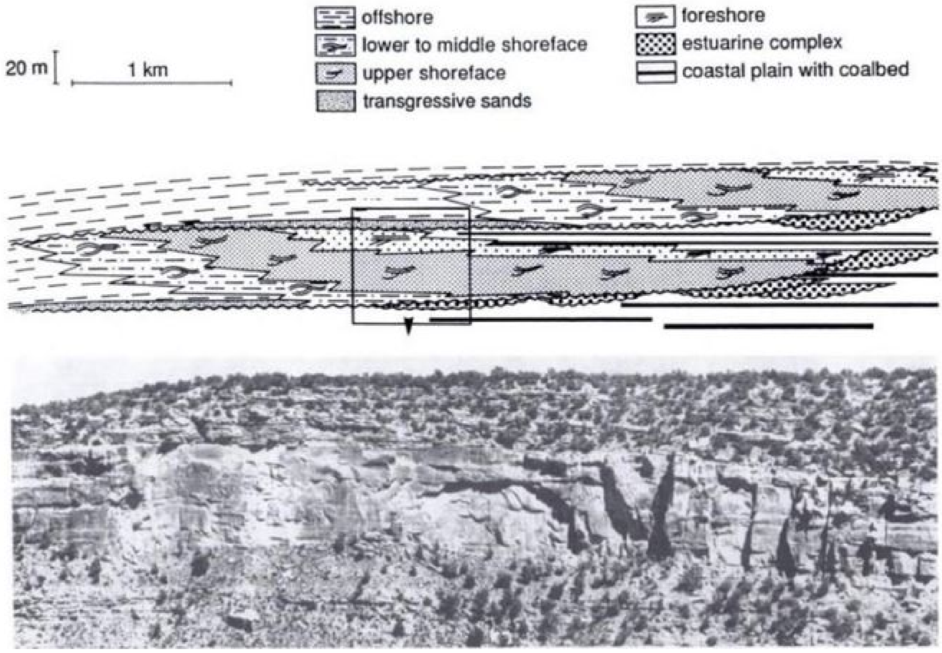

Figure 4.1.6. Cliff house sandstone, an analogue to the Tarbert formation, shows landward stepping stacking pattern. From Eschard et al. (1993).

4.2 Facies model

The lithological information about the Ness formation in 3.2.1, mainly is indicative of a continental environment, e.g. coal beds, soil beds and root zones. The water present during deposition is probably confined to fluvial channels, lagoons and possibly lakes. Looking at the morphological elements in a delta (Fig. 4.1.1), lower delta plain looks like a valid interpretation.

Went et al. (2013) suggest four main facies for the Ness formation (Fig. 4.2.1); lagoonal/lake margin, lagoon, peat swamp and fluvial channel.

The lagoonal/lake margin facies (no. 7.) contains the typical cross-laminated sandstones, that also can be found in fluvial elements as crevasse splays and the levee. Lagoon facies (no. 8.), also include bay fill, and typically has a very heterolithic strata with convolute or deformed bedding. Peat swamp coal (no. 9.) often is associated with lagoon facies (no. 8.). With the environment described in the faices over, defining the channels as mainly fluvial seems reasonable (no. 10.). However, it is possible that some of the channels closer to the delta front are dominated by tidal and wave influence.

An alternative facies characterisation of the Upper Ness surface at the Gullfaks field, can be found in the Fig. 4.2.2A. This facies architecture is fluvial and include

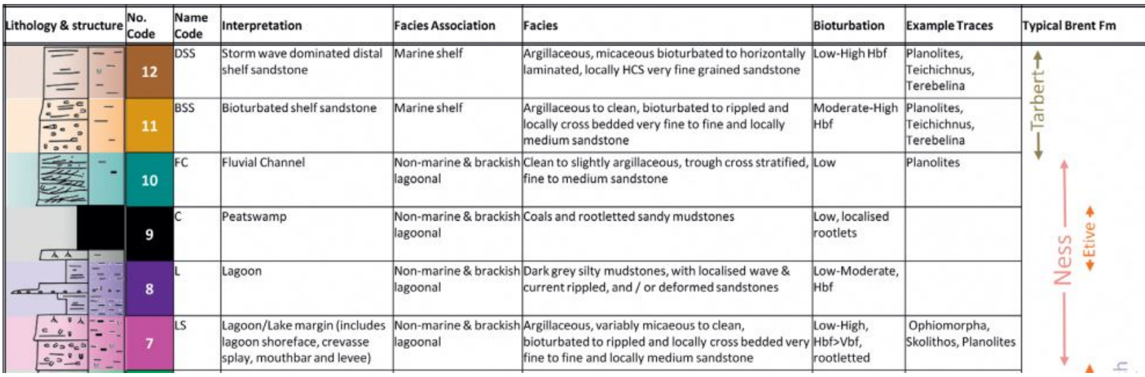
Tarbert
Ness
Etive

Lithology & structure	No. Code	Name Code	Interpretation	Facies Association	Facies	Bioturbation	Example Traces	Typical Brent Fm
	12	DSS	Storm wave dominated distal shelf sandstone	Marine shelf	Argillaceous, micaceous bioturbated to horizontally laminated, locally HCS very fine grained sandstone	Low-High Hbf	Planolites, Teichichnus, Terebelina	
	11	BSS	Bioturbated shelf sandstone	Marine shelf	Argillaceous to clean, bioturbated to rippled and locally cross bedded very fine to fine and locally medium sandstone	Moderate-High Hbf	Planolites, Teichichnus, Terebelina	
	10	FC	Fluvial Channel	Non-marine & brackish lagoonal	Clean to slightly argillaceous, trough cross stratified, fine to medium sandstone	Low	Planolites	
	9	C	Peatswamp	Non-marine & brackish lagoonal	Coals and rootletted sandy mudstones	Low, localised rootlets		
	8	L	Lagoon	Non-marine & brackish lagoonal	Dark grey silty mudstones, with localised wave & current rippled, and / or deformed sandstones	Low-Moderate, Hbf		
	7	LS	Lagoon/Lake margin (includes lagoon shoreface, crevasse splay, mouthbar and levee)	Non-marine & brackish lagoonal	Argillaceous, variably micaeous to clean, bioturbated to rippled and locally cross bedded very fine to fine and locally medium sandstone	Low-High, Hbf>Vbf, rootletted	Ophiomorpha, Skolithos, Planolites	

Figure 4.2.1. Facies architecture of the Upper Brent. From Went et al. (2013).

main elements that correlates with Fig. 4.1.2. The background floodplain facies would be relatively similar to the peat swamp coal (no. 9.) facies, and probably would include parts of the lagoon facies (no. 8.). The fluvial channel facies (no. 10) is equivalent in the figure below. The lagoon/lake margin facies (no. 7.) is split into levee sand, crevasse splay and channel margin.

The Tarbert formation has been more challenging to place in a depositional environment. The literature discussing sequence stratigraphy (references in Chap. 4.1) presents different parasequence boundaries for Tarbert, indicating that on a regional scale (northern North Sea), the Tarbert formation has significant lateral variations. Lateral variations within the Gullfaks Field, e.g. the northern, central and southern parts, can be possible.

Went et al. (2013) suggested in Fig. 4.2.1 two marine shelf facies; bioturbated shelf sandstone (no. 11.) and storm wave dominated distal self sandstone (no. 12.). The core sample in Fig. 3.2.4, could belong to the bioturbated shelf sandstone facies. However, based on the general lithology descriptions in Chap. 3.2, it appears that the Tarbert formation at Gullfaks is located more landward relative to Went et al. (2013) findings. The entire sequence appears to have been deposited in shallow water or coastal- plain environments close to a palaeoshoreline. It is here conceptualised that the Tarbert Formation can be described as a bay-head delta (see location of bay-head delta within the wave-dominated estuary in Fig. 4.1.3).

Based on these observations and assumptions it is conceptualised that the Tarbert formation includes a foreshore, an upper shoreface and a lower shoreface facies. A tidal influenced lagoonal facies, which probably can be subdivided into a distal tidal influenced and a proximal tidal influenced subfacies. In the lithology description it is referenced to thin coals and what Helland-Hansen et al. (1992) describes as continental 'Ness-like' deposits. Indicating that the peat swamp coal facies (no. 9.) in association with the more continental lagoon facies (no. 8.) from the Ness formation, also appears in the Tarbert formation. The channel facies in the Tarbert formation would be mainly fluvio-estuarine channels.

An alternative facies characterisation of the Upper Tarbert surface at the Gullfaks field, can be found in the Fig. 4.2.2B. It is based on fluvial facies, like in Fig. 4.2.2A. The channel sands in this figures is considerably wider than for the upper Ness. The is a considerable build up of channel sands along the North-West edge and central part of the field. It is also more levee sand facies and less background floodplain facies at the upper Tarbert than the Upper Ness. The log in Fig. 3.2.6 marks both the Upper Tarbert and Upper Ness as quite similar, described as delta marsh in the figure, indicating that Fig. 4.2.2B possibly portrays some "Ness-like" deposits. Generally, a fluvial facies division of the Tarbert formation can be a bit misleading and is probably not representative for the entire formation.

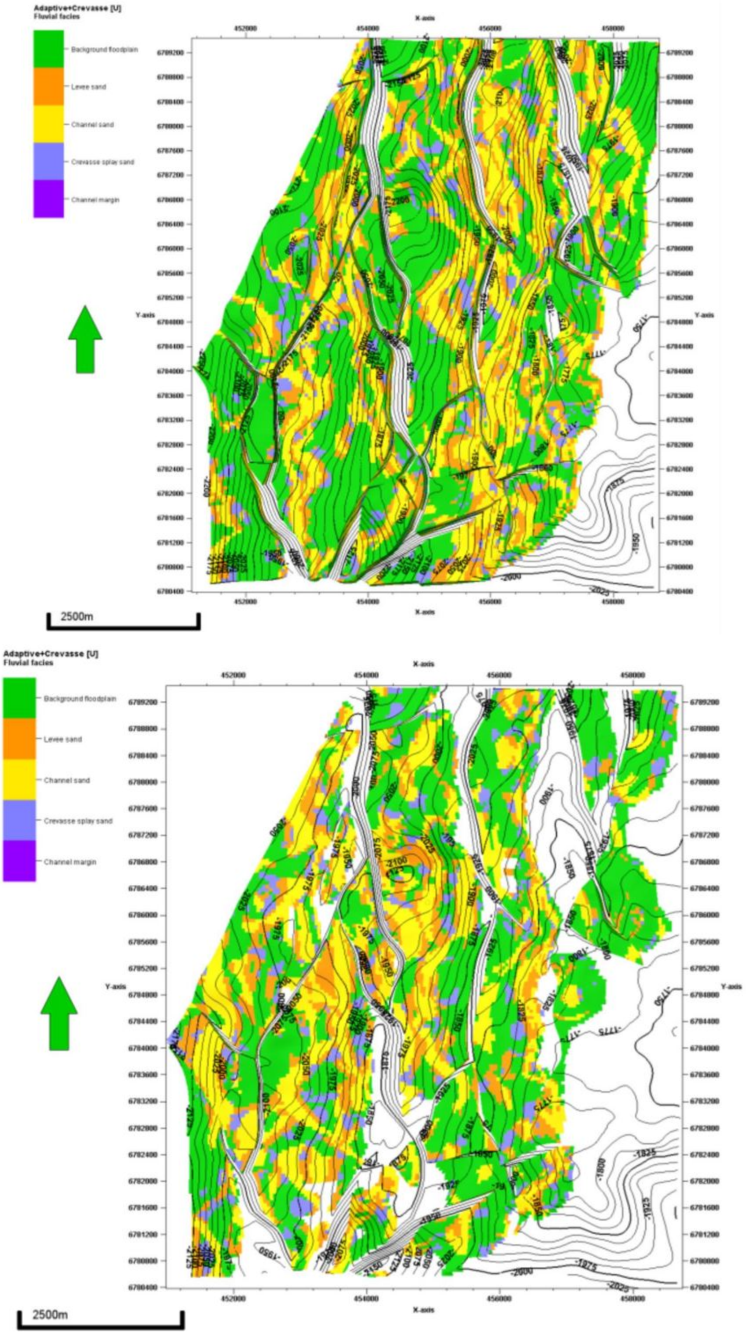
Adaptive+Crevasse [U]
Fluvial facies
Background floodplain
Levee sand
Channel sand
Crevasse splay sand
Channel margin
X-axis
Y-axis
452000
454000
456000
458000
6789200
6788800
6788400
6788000
6787600
6787200
6786800
6786400
6786000
6785600
6785200
6784800
6784400
6784000
6783600
6783200
6782800
6782400
6782000
6781600
6781200
6780800
6780400
2500m

Figure 4.2.2. A (Upper): Topographic view of Top Ness. B (Lower): Topographic view of Top Tarbert. Both with assigned facies; Background floodplain (green), Levee sand (orange), Channel sand (yellow), Crevasse splay sands (blue), Channel margin (purpel). From PETREL model, made available by D. Harishidayat, unpublished.

4.3 Petrophysical model

In Chap. 2.2 it was discussed how lithology and sedimentary structures strongly affect the results of petrophysical measurements. Particularly permeability measurements often can be read as a log indicating lithology and to some degree sedimentary structure. In Chap. 2 petrophysical values were mainly discussed on core or lamina-scale, in this chapter the focus is formation scale.

The facies and their associations as discussed in the previous chapter, can be used to say something about the relative relation of petrophysical properties. Quite intuitively it can be predicted that the peat swamp, floodplain and general tidal influenced lagoonal facies (Tarbert), would have a considerably low porosity and permeability values than for instance crevasse splay, foreshore and shoreface facies. This prediction is based on how much mud it is expected to be present in each facies.

In order to conceptualise what kind of petrophysical values and distribution that is to expect in the field, it can be useful to look at the corresponding petropysical plots to Fig. 4.2.2. Fig. 4.3.1 shows the porosity and the permeability of the Top Ness surface and Fig. 4.3.2 shows the petrophysical values of the Top Tarbert surface. These figures are based on the same core data as used in this thesis, but the total amount of input data in these models are considerably larger than what is used here.

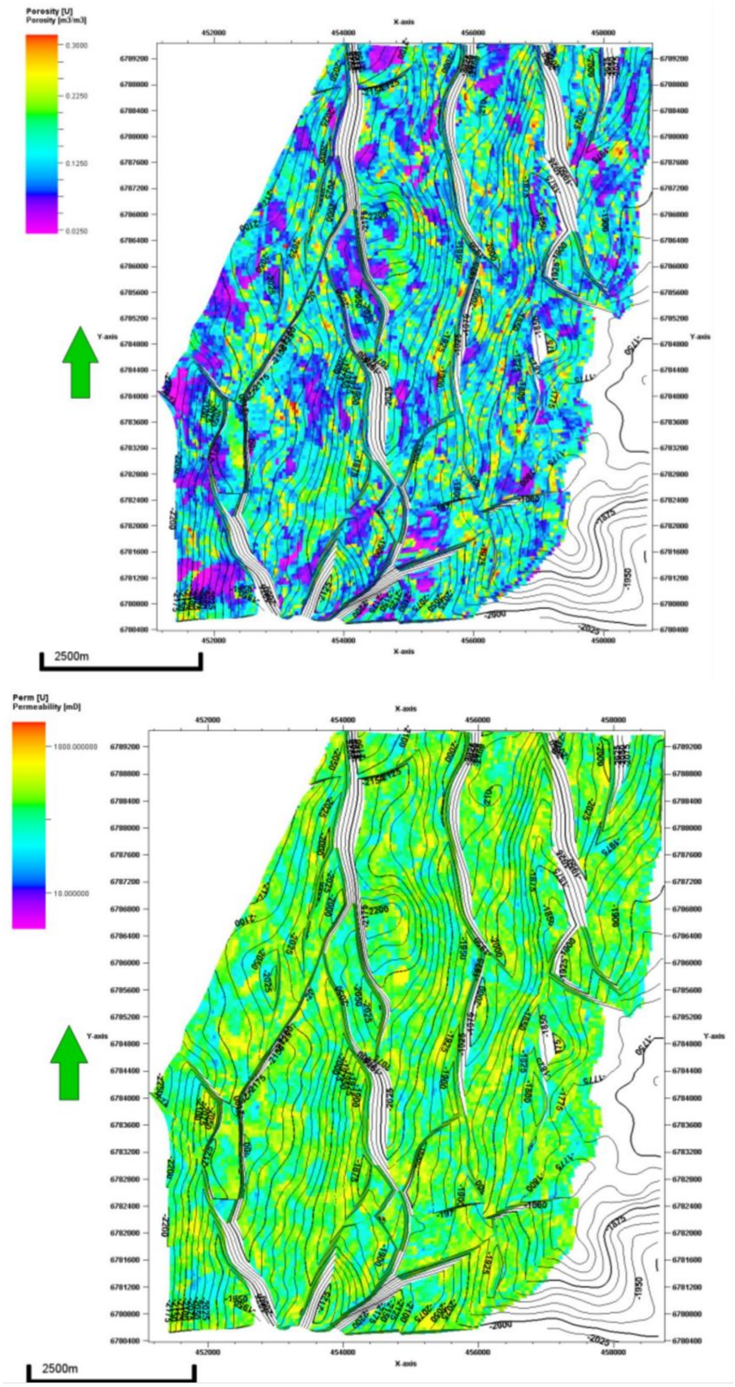
Porosity [U]
Porosity [m3/m3]
0.3000
0.2250
0.1250
0.0250
X-axis
452000
454000
456000
458000
Y-axis
6789200
6788800
6788400
6788000
6787600
6787200
6786800
6786400
6786000
6785600
6785200
6784800
6784400
6784000
6783600
6783200
6782800
6782400
6782000
6781600
6781200
6780800
6780400
2500m
Perm [U]
Permeability [mD]
1000.000000
10.000000
-2000
-2025
-1950
-1875
-1750
-1775

Figure 4.3.1. A (Upper): Topographic view of Top Ness, with assigned porosity values. B (Lower): With assigned permeability values. From PETREL model, made available by D. Harishidayat, unpublished.

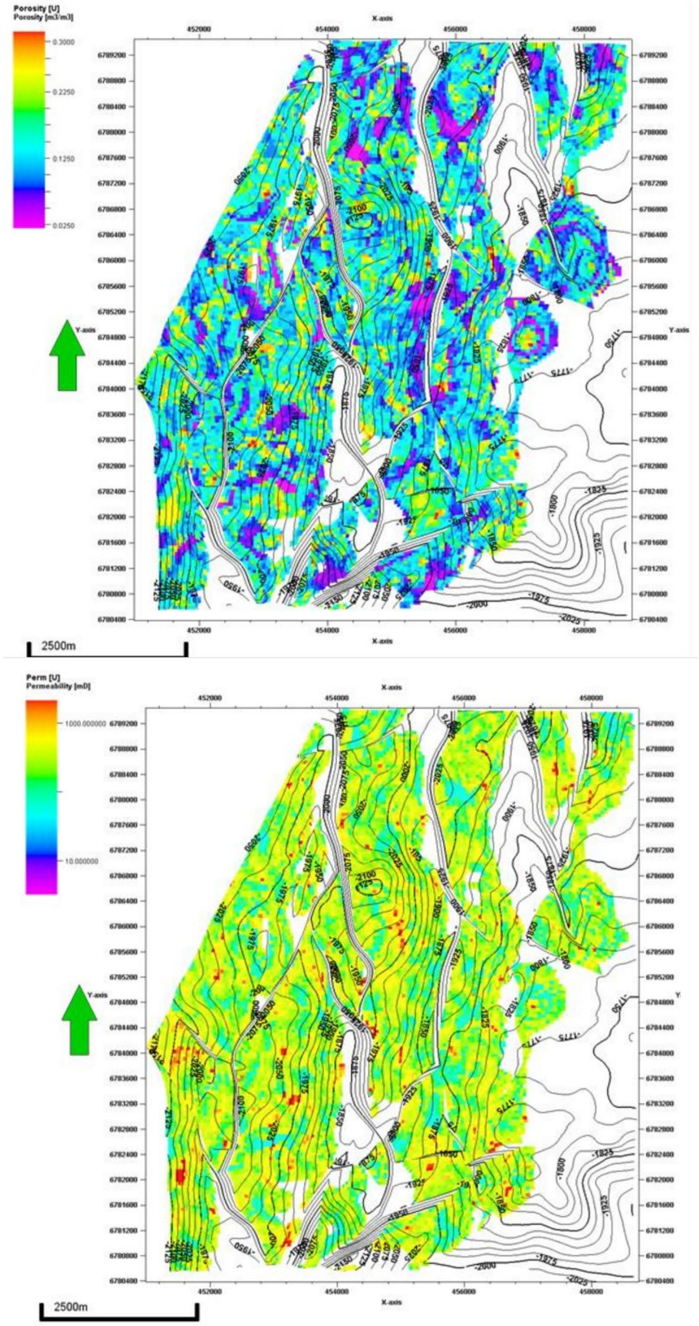
Porosity [U]
Porosity [m3/m3]
0.3000
0.2250
0.1250
0.0250
X-axis
452000
454000
456000
458000
Y-axis
6789200
6788800
6788400
6788000
6787600
6787200
6786800
6786400
6786000
6785600
6785200
6784800
6784400
6784000
6783600
6783200
6782800
6782400
6782000
6781600
6781200
6780800
6780400
2500m
Perm [U]
Permeability [mD]
1000.000000
10.000000
X-axis
Y-axis
2500m

Figure 4.3.2. A (Upper): Topographic view of Top Tarbert, with assigned porosity values. B (Lower): With assigned permeability values. From PETREL model, made available by D. Harishidayat, unpublished.

Chapter 5

Geomodeling tool

A three-dimensional (3D) reservoir model can have different purposes, for instance it can be built for visualisation, well planning, fluid simulation and improved oil recovery. The reservoir model discussed in this thesis is a *fit-for-purpose* model, with the purpose of characterising petrophysical properties. Ringrose and Bentley (2015) describe the overall aim for reservoir modelling as; *"to capture knowledge of the subsurface in a quantitative form in order to evaluate and engineer the reservoir"* (p. 62). A reservoir model is not a true representation of the subsurface, but rather a simplified model with elements of the truth obtained from measurable input data and geological knowledge. As Box and Draper (1987) stated, *"essentially, all models are wrong, but some are useful"* (p. 424).

Geomodelling defines the topology, geometry and physical properties of geological objects by using mathematical methods (Mallet, 2002). A broad variety of computer packages for geomodelling and reservoir modelling exist, all with slightly different approaches and user area. In this thesis the software *Leapfrog Geo*[1] is used as modelling tool. Leapfrog Geo is a commercial available software that uses a deterministic modelling approach.

The aim of this chapter is to review the workflow and the data used is the modelling process.

5.1 Workflow

The overall workflow covered in this thesis is illustrated in Fig.5.1.1. The figure is inspired by Ringrose and Bentley (2015), and is the first part of the general workflow diagram for a *fit-for-purpose* model. The aim for this thesis coincides with the purpose of this reservoir model; to characterise the petrophysical properties, porosity and permeability, of the Upper Brent GP at Gullfaks. Property modelling is the step where petrophysical properties is assigned to the cells of the reservoir model (Bjørlykke, 2010). The model is not built for any other application than petrophysical characterisation. The geological conceptual model was discussed in Chap. 4 and in this chapter is the focus on how the reservoir model is built.

---

[1] Leapfrog® is a software developed by ARANZ Geo Limited.

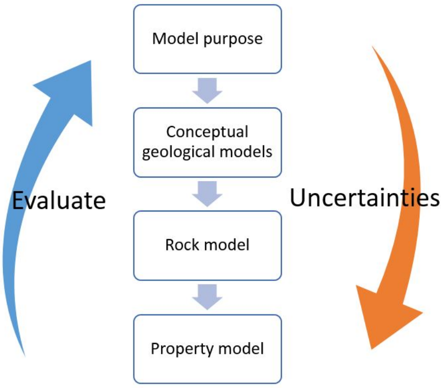

Figure 5.1.1. Overall workflow covered in this thesis.

There is a reason behind pointing out the overall workflow; no reservoir model should be built without a clear defined purpose. The purpose of the model should always be the foundation that the algorithm choice (Chap. 2.3.4) is based on. The purpose of the model also determines what kind and which amount of geological information should be included in the model.

In this case, the main data source are from core samples, of which the data can be considered deterministic. A deterministic algorithm choice is justified under the assumption that the available geological data is sparse.

5.1.1 Leapfrog Geo

Leapfrog Geo is a three-dimensional (3D) geological model software package, developed for mineral resource exploration. The main advantage of this software is that it accepts borehole data as a main data source and allows the user to construct a model relatively fast. The general data processing workflow in Leapfrog Geo is shown in Fig.5.1.2.

The software uses *radial basis functions* (RBFs, after Hardy (1971)) to interpolate the data in the 3D space. The RBFs are global interpolation methods, which means that the interpolation is dependent on all the data points. One of the benefits of RBFs is that they can provide smooth surface interpolations (Cowan et al., 2002). The surfaces in the model are constructed as finite approximations with infinite

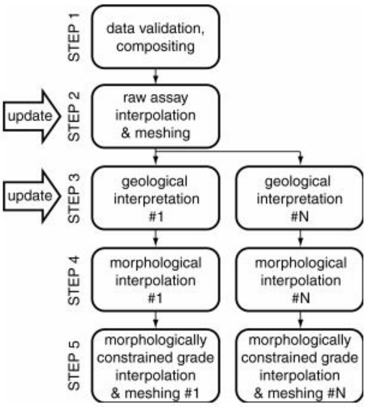
STEP 1
data validation, compositing
STEP 2
update
raw assay interpolation & meshing
STEP 3
update
geological interpretation #1
geological interpretation #N
STEP 4
morphological interpolation #1
morphological interpolation #N
STEP 5
morphologically constrained grade interpolation & meshing #1
morphologically constrained grade interpolation & meshing #N

Figure 5.1.2. Leapfrog Geo workflow scheme. From Cowan et al. (2002).

details which are implied to exist in a continuous volume function. In other words, Leapfrog Geo is a implicit modelling tool (Cowan et al., 2003).

Carr et al. (2001) described the mathematics behind the radial basic function interpolation process. The goal is to approximate the signed-distance function f($\mathbf{x}$) by an interpolant s($\mathbf{x}$). A distinct set of nodes $X = \sum_{i=1}^{N} \{\mathbf{x_i}\} \subset \mathbb{R}^3$ and a set of functions values $\{f_i\}_{i=1}^{N} \subset \mathbb{R}$ can be used to find an interpolat $s : \mathbb{R}^3 \to \mathbb{R}$, such that

$$s(\mathbf{x_i}) = f_i, \quad i = 1...N. \tag{5.1}$$

Points $\mathbf{x} \in \mathbb{R}^3$ is here denoted by $\mathbf{x} = (x, y, z)$.

A RBF is an equation of the form

$$s(x) = p(\mathbf{x}) + \sum_{i=1}^{n} \lambda_i \phi(|\mathbf{x} - \mathbf{x_i}|), \tag{5.2}$$

where p is a polynomial of low degree and the coefficients λ_i are real numbers. The points $\mathbf{x_i}$ are in this case the centres of the RBF.

The basic function ϕ is a real valued function on $[0, \infty)$, usually unbounded. For fitting a smooth function of two variables the thin-plate spline of $\phi(r)$ is used as

$$\phi(r) = r^2 log(r), \tag{5.3}$$

where r is the radius. Other common basic functions includes the multiquadric $\phi(r) = \sqrt{r^2 + c^2}$ used for e.g. fitting topographic data and the Gaussian $\phi(r) = exp(-cr^2)$ for e.g. neural networks.For fitting functions of three variables biharmonic $\phi(r) = r$ and triharmonic $\phi(r) = r^3$ splines can be used.

The benefit of using RBFs on scatter data is that the associated system of linear equations is guaranteed to be invertible and the RBFs do not require the data to line on a regular grid. However, the coefficient λ_i can not be an arbitrary number. Equation (5.2) imply that there must be orthogonality or side conditions. Here the side condition imposed for the coefficient λ_i of all the polynomial $p(x_j)$, can be written as;

$$\sum_{j=1}^{n} \lambda_j p(x_j) = 0. \tag{5.4}$$

Equation (5.4) is the same as the Kriging estimator in equation (2.20), indicating that λ_j is Kriging weights.

The RBF interpolation uses linear weighs in the exact same way as in Kriging. The difference between Kriging and RBF interpolation is that Kriging uses the covariance function obtained from a variogram, while RBF uses a basic function that is chosen from a standard set (Cowan et al., 2003).

An alternative to using RBFs in order to generate meshes (see Chap. 5.3.1) is the *Delaunay triangulation*. The Delaunay triangulation generates unstructured meshes of triangles that can be used in interpolation, the finite element method and the finite volume method. While RBF is an implicit method, Delaunay triangulation works in the finite element domain. The idea behind the method is that within a finite point set S in the plane, a triangle within a circle with a fixed circumcenter and circumradius can be designed. The ratio between the triangle's circumradius and the length of its shortest edge should be as small as possible. Any number of points in S can lie on a Delaunay triangle's circumcircle, but the circumcircle in itself can not contain any points. The principel is illustrated in Fig. 5.1.3. Horizontally spaced scatter data yield the best result when generating meshes. More detailed reviews of the Delaunay triangulation method can be found in e.g. Lee and Schachter (1980); Shewchuk (2002).

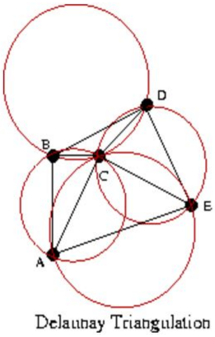

Figure 5.1.3. Illustration of Delaunay triangulation. From `http://www.geom.uiuc.edu/~samuelp/del_project.html`.

5.1.2 Generic approach

The generic approach used in this reservoir model is data-driven. Ringrose and Bentley (2015) discuss the data driven approach compared to a more concept-driven approach to reservoir modelling. In the data driven approach the data analysed and statistical guidelines are drawn. These guidelines are input to the statistical model of the reservoir, which is implemented by statistical algorithms. The outcome of the algorithm is a model, which can be interpreted and a forecast emerges (Fig. 5.1.4).

The data driven approach closely resembles the default path in reservoir modelling. Because of the algorithm and computer software chosen in this thesis, the user's possibility to alter the outcome of the modelling process is generally low. The result of the algorithm is one strongly deterministic model. If a stochastic algorithm was chosen instead a more concept-driven approach could be implemented. The algorithm produces several probable models, where the model closest to the conceptual model could be chosen.

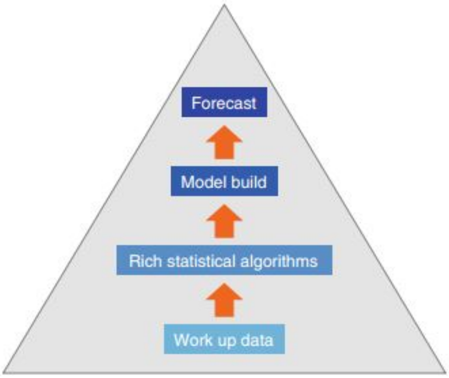

Figure 5.1.4. Data-driven generic approach. From Ringrose and Bentley (2015).

In the following chapter, Chap. 5.2, the input data to the model is introduced. The point-data from seismic constitute the framework of the model; surfaces and faults. The wells are then placed into the model with their assigned properties. In Chap. 5.2, the estimated data is resulting from the statistical algorithm introduced.

5.2 Input parameters

All the data in the Gullfaks model is implemented as data points (scatter-data), and is constituted of 7 surfaces (Fig. 5.2.2), 22 faults and 14 wells (Fig. 5.2.1) in total. The formations that are examined in this thesis is the Ness and Tarbret formation. The Ness FM is split into two, the Upper and Lower Ness. The Tarbert formation is here divided in three parts; Tarbert Lower, Middle and Upper formation. The BCU (Base Cretaceous Unconformity) surface is included because the faults terminate against this surface, but the volume here termed the "Viking GP." is not analysed.

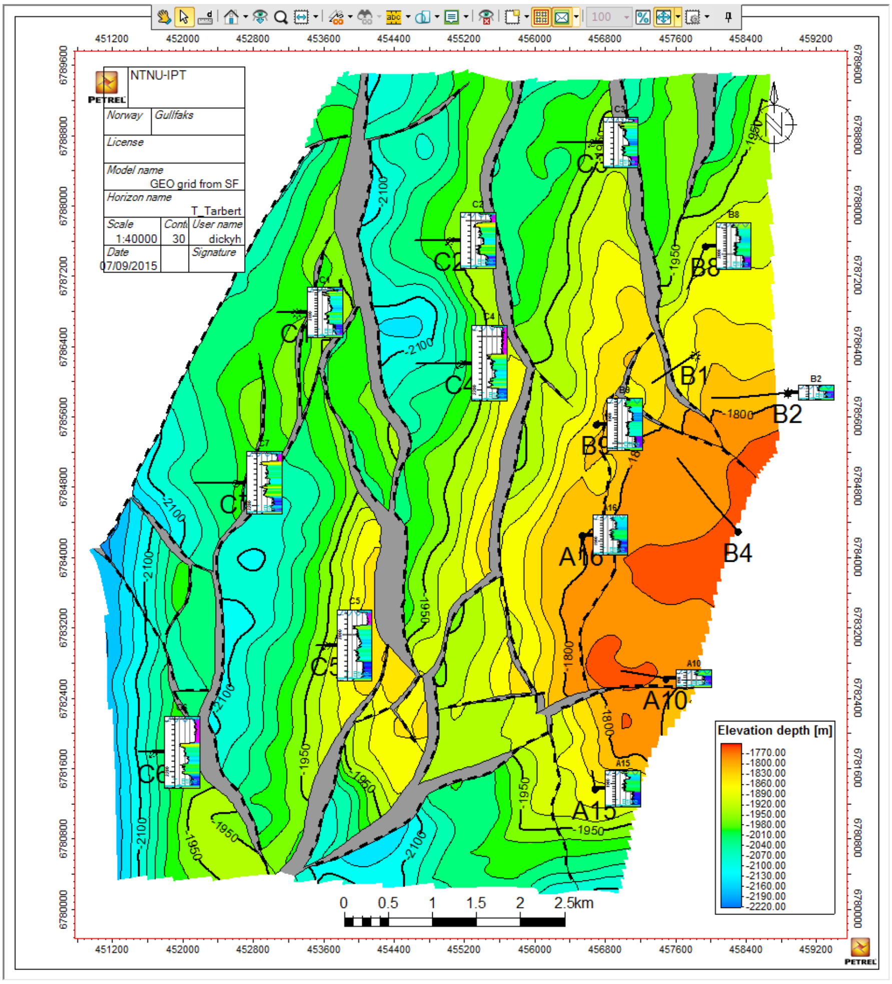
NTNU-IPT
PETREL
Norway
Gullfaks
License
Model name
GEO grid from SF
Horizon name
T_Tarbert
Scale
1:40000
Cont.
30
User name
dickyh
Date
07/09/2015
Signature
451200
452000
452800
453600
454400
455200
456000
456800
457600
458400
459200
6789600
6788800
6788000
6787200
6786400
6785600
6784800
6784000
6783200
6782400
6781600
6780800
6780000
C3
C2
C1
C4
C7
C5
C6
B8
B1
B2
B9
B4
A16
A10
A15
-2100
-1950
-1800
0
0.5
1
1.5
2
2.5km
Elevation depth [m]
-1770.00
-1800.00
-1830.00
-1860.00
-1890.00
-1920.00
-1950.00
-1980.00
-2010.00
-2040.00
-2070.00
-2100.00
-2130.00
-2160.00
-2190.00
-2220.00

Figure 5.2.1. Topographic overview of the Gullfaks Field at Top Tarbert, notice the well placements. The grey areas are fault zones. From PETREL model, made available by D. Harishidayat, unpublished.

5.2.1 Structural data

The structural data constitute the framework of the model and originates from a seismic survey. The surfaces and faults are implemented as scatter-data with coordinates (East, North, Z), where Z is the depth in meters.

The database of where the data was retrieved is designed for the PETREL software. Therefore, the data was manipulated and transferred from Excel files into Leapfrog Geo. Each surface and fault constitute of several thousand coordinate points.

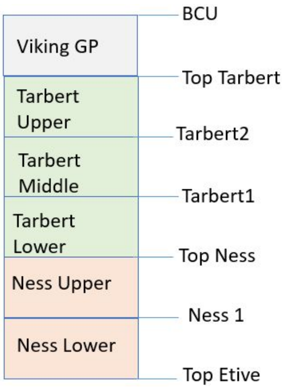
BCU
Viking GP
Top Tarbert
Tarbert Upper
Tarbert2
Tarbert Middle
Tarbert1
Tarbert Lower
Top Ness
Ness Upper
Ness 1
Ness Lower
Top Etive

Figure 5.2.2. Formations and surfaces in the Gullfaks model.

A screenshot from Leapfrog Geo is visible in Fig. 5.2.3. Each of the surfaces are entirely made up of the scatter-data. On the south-eastern side of the figure it appear like the layers overlap in the same points. Below the model is the point-surfaces listed with their corresponding colours. On the left side of the figure all the surfaces and faults are listed. The BCU point-surface is a relatively plain surface that obstruct the view of the underlying morphology, and is therefore not included in the figure below.

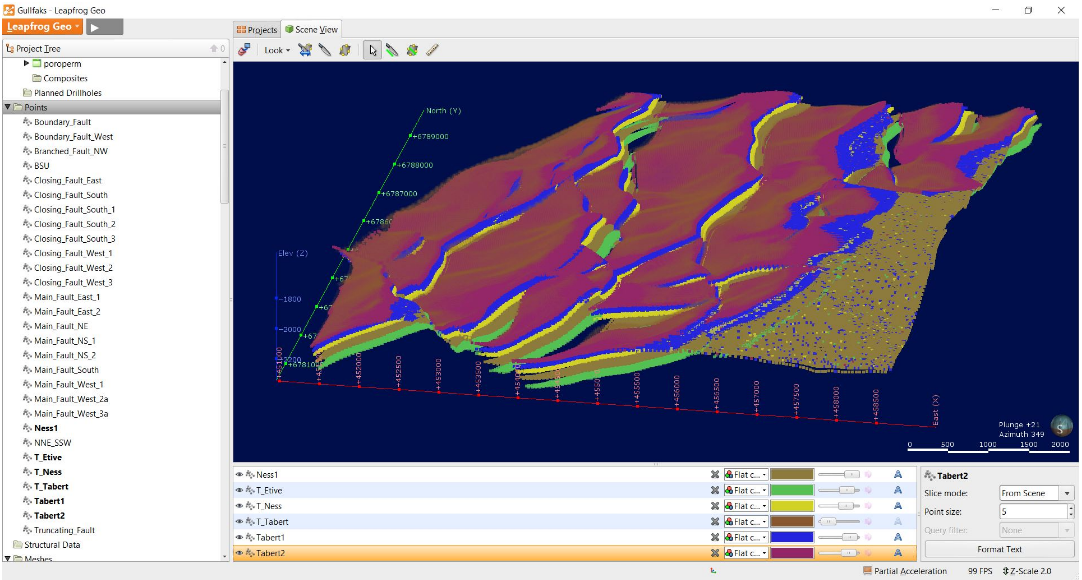
Gullfaks - Leapfrog Geo
Leapfrog Geo
Project Tree
poroperm
Composites
Planned Drillholes
Points
Boundary_Fault
Boundary_Fault_West
Branched_Fault_NW
BSU
Closing_Fault_East
Closing_Fault_South
Closing_Fault_South_1
Closing_Fault_South_2
Closing_Fault_South_3
Closing_Fault_West_1
Closing_Fault_West_2
Closing_Fault_West_3
Main_Fault_East_1
Main_Fault_East_2
Main_Fault_NE
Main_Fault_NS_1
Main_Fault_NS_2
Main_Fault_South
Main_Fault_West_1
Main_Fault_West_2a
Main_Fault_West_3a
Ness1
NNE_SSW
T_Etive
T_Ness
T_Tabert
Tabert1
Tabert2
Truncating_Fault
Structural Data
Meshes
Projects
Scene View
Look
North (Y)
+6789000
+6788000
+6787000
Elev (Z)
-1800
-2000
East (X)
+455500
+456000
+456500
+457000
+457500
+458000
+458500
Plunge +21
Azimuth 349
0
500
1000
1500
2000
Ness1
T_Etive
T_Ness
T_Tabert
Tabert1
Tabert2
Flat c...
Tabert2
Format Text
Partial Acceleration
99 FPS
Z-Scale 2.0

Slice mode: From Scene

Point size: 5

Query filter: None

Figure 5.2.3. Leapfrog Geo screen: Surfaces from scatter-data. BCU not included. The z-axis is magnified to enhance visibility.

The 22 faults, as seen in Fig. 5.2.4, were implemented in the same manner as the point-surfaces. The direction of the faults are mainly in an N-S to a NE-SW direction.

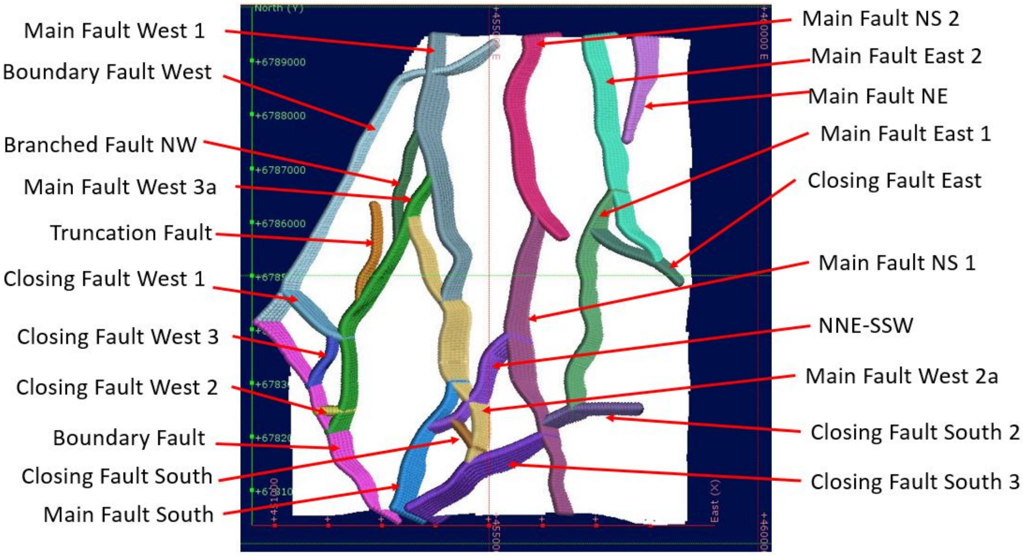
North (Y)
+6789000
+6788000
+6787000
+6786000
+45500 E
+460000 E
East (X)
Main Fault West 1
Boundary Fault West
Branched Fault NW
Main Fault West 3a
Truncation Fault
Closing Fault West 1
Closing Fault West 3
Closing Fault West 2
Boundary Fault
Closing Fault South
Main Fault South
Main Fault NS 2
Main Fault East 2
Main Fault NE
Main Fault East 1
Closing Fault East
Main Fault NS 1
NNE-SSW
Main Fault West 2a
Closing Fault South 2
Closing Fault South 3

Figure 5.2.4. The faults from the point-data, with their corresponding names. Implemented on Top Tarbert surface.

5.2.2 Well data

The data files containing well data were organised as "Collar" (Start point of each well), "Survey" (well trajectory) and "PoroPerm" (petrophysical data). The wells are implemented in the model with a start point defined by coordinates (East, North, Depth). The well names (hole-id) and their starting coordinates can be found in Fig. 5.2.5A. The input requires a maximum depth value, which only requires a depth large enough so that the necessary data is not cut from the model. The distribution of wells in the model is plotted in Fig. 5.2.5B.

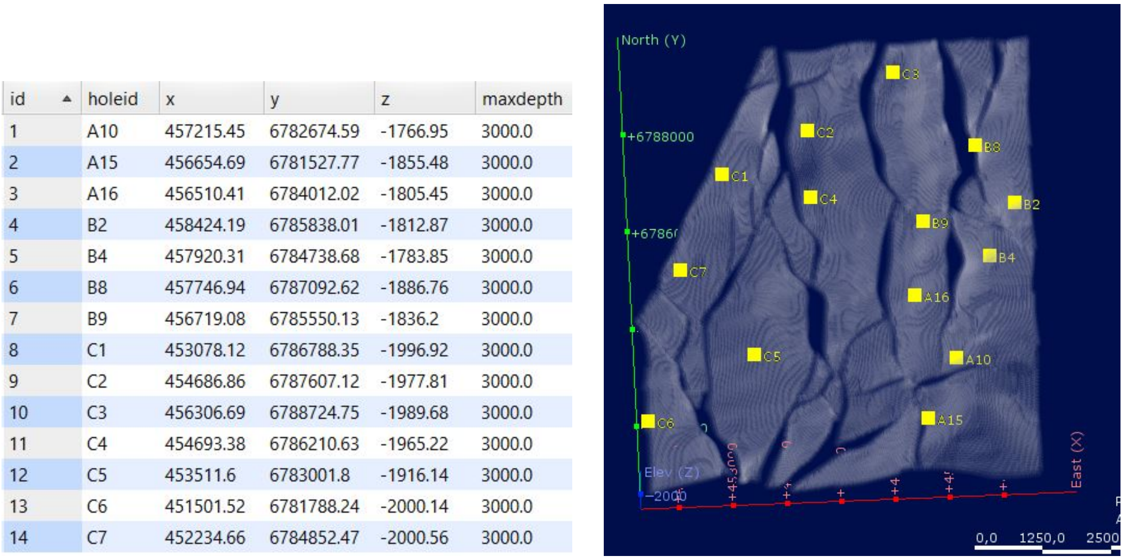

id ▲	holeid	x	y	z	maxdepth
1	A10	457215.45	6782674.59	-1766.95	3000.0
2	A15	456654.69	6781527.77	-1855.48	3000.0
3	A16	456510.41	6784012.02	-1805.45	3000.0
4	B2	458424.19	6785838.01	-1812.87	3000.0
5	B4	457920.31	6784738.68	-1783.85	3000.0
6	B8	457746.94	6787092.62	-1886.76	3000.0
7	B9	456719.08	6785550.13	-1836.2	3000.0
8	C1	453078.12	6786788.35	-1996.92	3000.0
9	C2	454686.86	6787607.12	-1977.81	3000.0
10	C3	456306.69	6788724.75	-1989.68	3000.0
11	C4	454693.38	6786210.63	-1965.22	3000.0
12	C5	453511.6	6783001.8	-1916.14	3000.0
13	C6	451501.52	6781788.24	-2000.14	3000.0
14	C7	452234.66	6784852.47	-2000.56	3000.0

Figure 5.2.5. A (left): Name of each well (hole-id) and start coordinates as (x,y,z)=(East, North, Depth) after ED50-UTM 31N coordinate system. The list include an arbitrary maximum depth of the well. B (right): Plot of the well points in Leapfrog Geo. C-group located to the west, B-group in North-East and A-group in South-East.

The wells are defined from the BCU surface and to the Top Etive surface and requires a defined well trajectory. The trajectory is plotted as point-coordinates of (depth, dip angle, azimuth) for each of the wells. The depth is the measured depth in the well, which means that it starts at zero at the defined start-point at BCU.

When the wells are defined, the petrophysical data can be assigned to each well (shown in Fig. 5.2.6). In figure 5.2.6A, the porosity scale look a bit unusual, but $300\text{x}10^{-3}$ is the same as 0.3 or 30%. The scale for permeability, Fig. 5.2.6B, is in millidarcy (mD).

The petrophysical values are measured every 0.5 m along the core, which is a relatively dense sampling interval. Most of the wells have a length around 60-70 m, but the C-group of wells are considerably longer. The longest well is C4, which

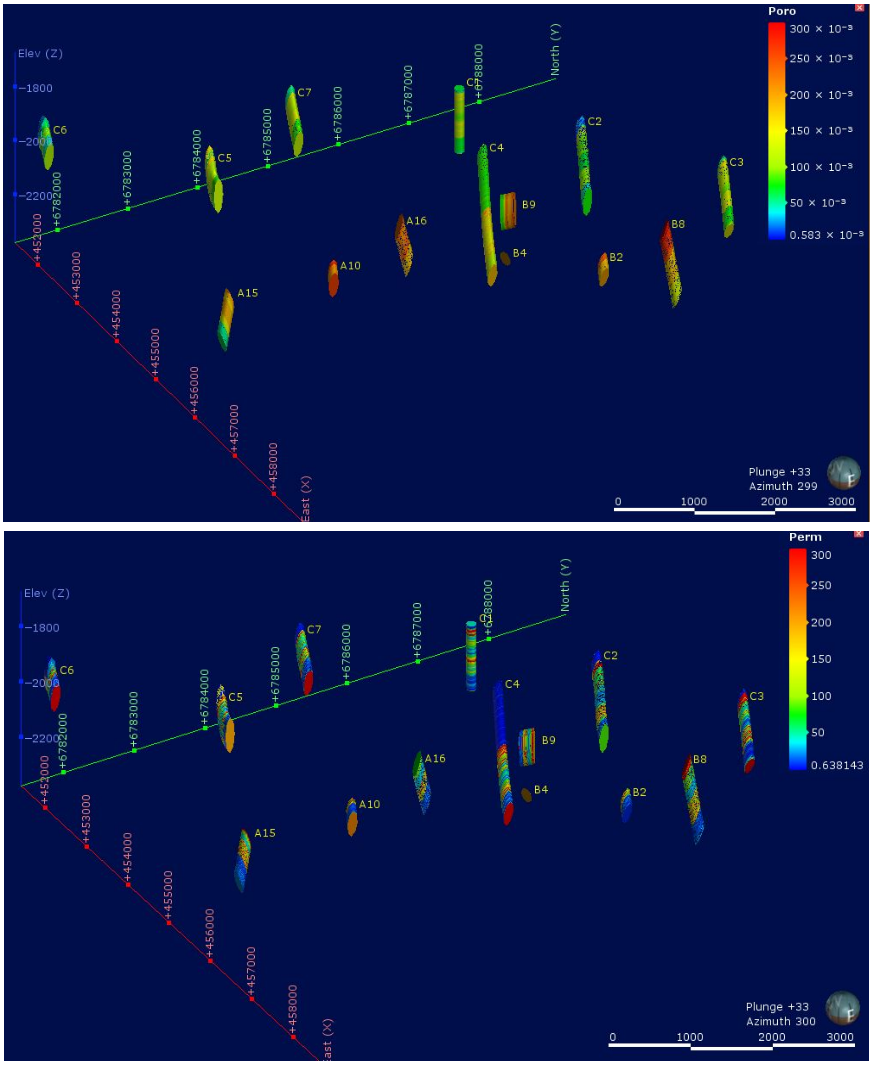
Poro
300 × 10⁻³
250 × 10⁻³
200 × 10⁻³
150 × 10⁻³
100 × 10⁻³
50 × 10⁻³
0.583 × 10⁻³
Elev (Z)
−1800
−2000
−2200
North (Y)
East (X)
+6782000
+6783000
+6784000
+6785000
+6786000
+6787000
+6788000
+452000
+453000
+454000
+455000
+456000
+457000
+458000
C6
C5
C7
C1
C4
C2
C3
B9
B4
B2
B8
A16
A10
A15
Plunge +33
Azimuth 299
0
1000
2000
3000
Perm
300
250
200
150
100
50
0.638143
Plunge +33
Azimuth 300

Figure 5.2.6. A (Upper): Well points of porosity. B (Lower): Well points of permeability in unit mD. The z-axis is magnified to increase visibility.

is close to 500 m deep measured along the well. The A- and B-group of wells are located on a local heights, as it can also be seen from Fig. 5.2.1. The formations thickens towards the C-group of wells. The well trajectory also affect the measured depth, whereof some of the wells in the model do not reach the Top Etive surface (e.g. B4.).

The distribution of petrophysical properties with respect to number of occurrences for all the wells can be seen in Fig. 5.2.7. The porosity properties are more

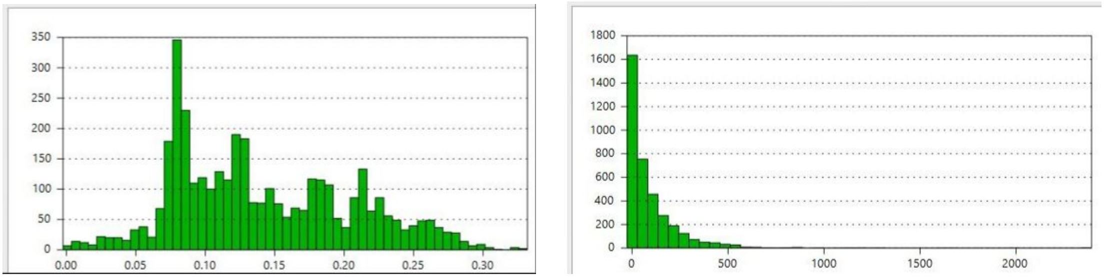

Figure 5.2.7. A (Left): Histogram of porosity properties. Porosity value along the x-axis and number of occurrences long the y-axis. B (Right): Histogram of permeability properties. Permeability value [mD] along the x-axis and number of occurrences long the y-axis.

evenly distributed than the measured permeability values. The majority of the permeability values are relatively low and few high values. A permeability and porosity property plot as a function of depth is a good way to get an overview of the well data. In Fig. 5.2.8 the well A10 is plotted, the plot is read in the same was as wireline logs. Both plots indicates peaks of a very good quality reservoir rock, from ~0-20 m depth. Below that the quality is poor. Plots for all the wells are located in Appendix A.

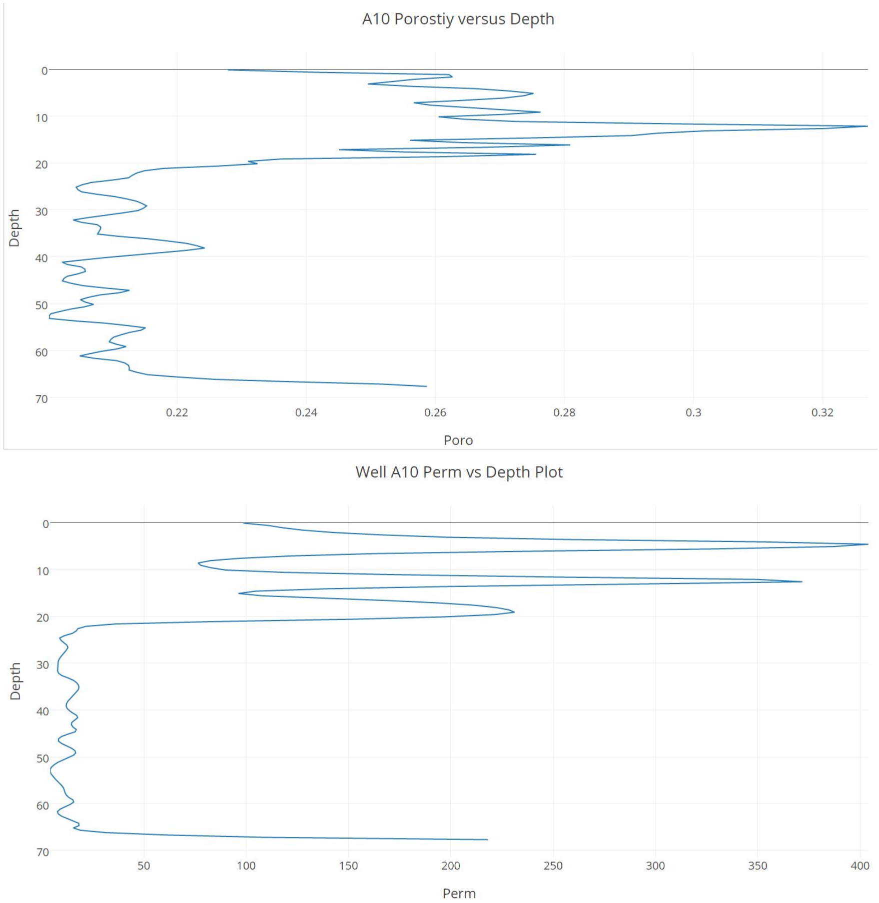

Figure 5.2.8. A (Upper): Well A10: Porosity versus depth [m] plot. B (Lower): Permeability [mD] versus depth [m] plot.

5.3 Estimated parameters

Modelling software often behaves as a "black box". The program is fed input parameters by the user and the program returns an output. However, what happens in between can be somewhat diffuse. In this chapter the main elements in the modelling process are reviewed.

5.3.1 Meshes

The scatter-points which was implemented in the model needs to be connected, this is done by interpolation. By default Leapfrog Geo utilises the radial basic function (RBFs, Chap. 5.1.1) as an interpolator and the standard type is calculated based on a linear variogram model. An alternative mesh type is formed by Delaunay triangulation (Chap. 5.1.1). The result of the interpolations is referred to as an iso-surface.

In Fig.5.3.1A the RBF method in Leapfrog Geo has been used to form an iso-surface of Top Etive. The resulting mesh can be seen as grey in the figure, it is very unevenly distributed. There is a higher density of scatter-points in the middle of the surface compared to the edges and the mesh is adoptive to the point density. According to Royer et al. (2015), a 3D implicit function is generally defined at the nodes of a tetrahedral or hexahedral mesh. The mesh in this case has a tetrahedral shape (Fig. 5.3.2), with a large variation in sizes depending on the distance between the connected nodes. The standard set variogram model used in the RBFs, which is underlying in all the formation iso-surfaces, is based on having the properties of range=3000, sill=600, and no nugget effect.

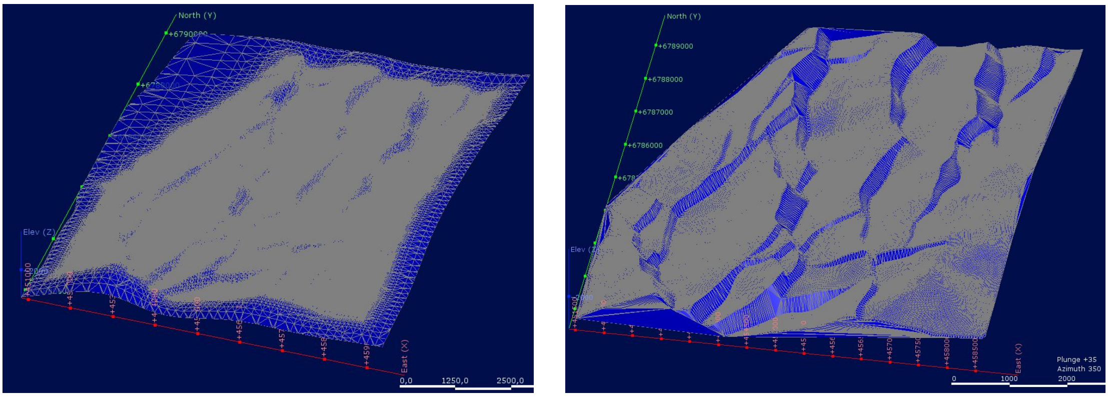

Figure 5.3.1. A (Left): Iso-surface from radial basic function. B (Right): Triangulated Iso-surface. Both figures show the Top Etive surface.

Alternatively, a triangulated mesh distribution can be chosen for the iso-surfaces, shown in Fig. 5.3.1B. An example of the shape of a triangulated mesh can be seen in Fig. 5.3.2). This mesh is relatively evenly distributed and more uniform in size. The triangulated mesh also preserves the original form of the surface and particularly the fault zones are drastically improved.

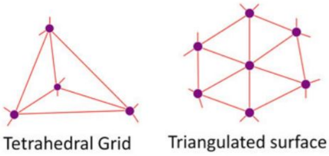

Figure 5.3.2. Mesh grids formed by different node placement. From Royer et al. (2015).

Even though the triangulated iso-surface look better than the RBF mesh, it is first when the faults are implemented that the major difference appears. Fig. 5.3.3A shows how the iso-surface behaves between the faults under a radial basic function formed mesh. The surface bows out on the outer side of the fault before it bows out on the inside again with a "S"-pattern. The triangulated iso-surfaces on the other hand share the common points with the fault, Fig. 5.3.3B, and divide the iso-surfaces in segments. All the formation iso-surfaces are therefore implemented with triangulated meshes, because this method yields the best result.

All the fault iso-surfaces are interpolated by the radial basic function. By default Leapfrog Geo assign alternating standard set variogram models to each fault dependent on their length and morphology.

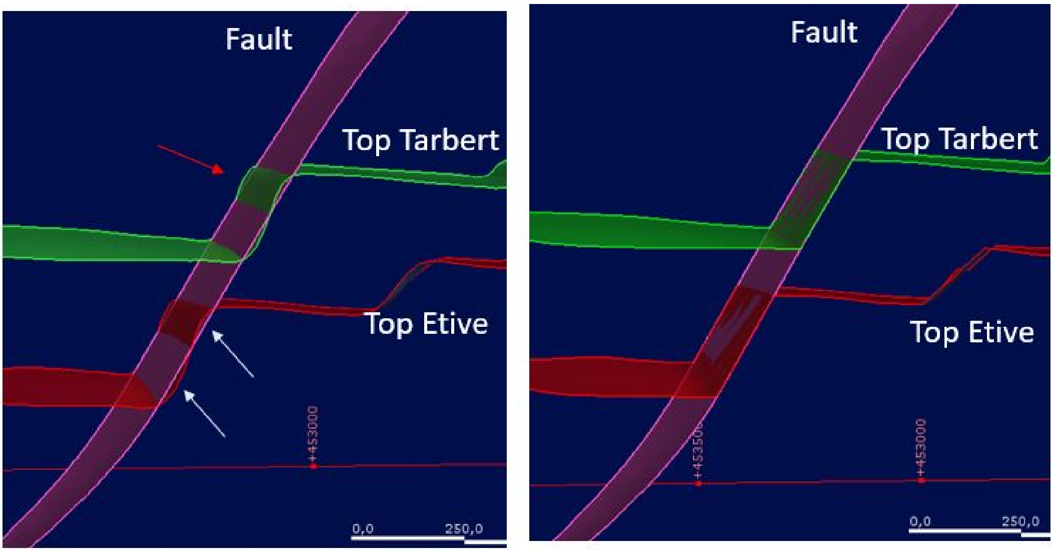

Figure 5.3.3. Iso-surfaces cut through of a fault: A (Left): Iso-surface interpolated with radial basic function, where white arrows indicate where Top Etive is present on both sides of the fault. Red arrow shows that Top Tarbert follows the same pattern. B (Right): Triangulated iso-surfaces that follows the fault.

5.3.2 Volume and grid

Up to this point the focus has only been on iso-surfaces that were interpolated from scatter-points either by the radial basic function or triangulation. The next step is to fill in the volume between the surfaces. This volume represent the formations and is limited by the mesh grids.

In this thesis two volume models are chosen for closer study; the "Geological Model" (GM) and the "Geological Model Fault Block 2" (GM Fault Block 2). The GM model contains the formations extending over the entire field. The field is built up of several fault blocks, and the GM Fault Block models represent each of these fault blocks. An individual fault block, GM Fault Block 2, has been isolated.

The volume models constitute the framework of the petrophysical models. The petrophysical data from all the wells are interpolated by the radial basic function and shown as interval values within a confined 3D volume.

Instead of limiting a continuous volume between meshes, a block model can be used. The block model has a regular cell grid, as shown in Fig. 5.3.4. Each cell represent a volume which can be assigned a petrophysical value. These petrophysical values are estimations and the result is a property model. In a combined block model, both permeability and porosity values can be assigned, but for visualisation purposes only one petrophysical value at the time will be shown in this thesis.

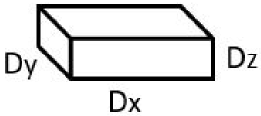

Figure 5.3.4. Illustration of regular grid cell with $D_x = D_y \geq D_z$.

5.3.3 Output

The output is divided into two parts; the first part is the volume formation models (no. 1-2) which is a necessary step to reach the second part, the property models. Two procedures has been chosen to characterise the petrophysical properties of Gullfaks (no. 3-4). The results of the two procedures are located in Chapter 6. All the porosity and permeability colour scales in the figures in Chap. 6 are equal for easy comparison.

1. The Geological Model (GM): The GM model is an volume model of the entire field where the volumes is constrained within the iso-surfaces of the formations.

2. The Geological Model Fault Block 2 (GM Fault Block 2): The fault block number 2 is selected and isloated. The volumes is constrained within the iso-surfaces of the formations.

3. Petrophysical model of the Geological Model (GM) volume:

This approach is the default method in Leapfrog Geo to visualise independent variables. The model is confined within the total GM volume, but not the formation volumes.
3a. Interpolated model: The petrophysical values are interpolated within the volume and grouped together in intervals by default (see table 1 below).

Porosity interval	Permeability interval [mD]
<0.082	<10.0
0.082-0.118	10.0-40.0
0.118-0.172	40.0-130.0
>0.172	>130.0

3b. Block Model. The petrophysical values are estimated and shown as a block model of the GM volume. The dimensions of each grid cell is selected to be 40m x 40m x 10m.

4. Petrophysical model of the Geological Model Fault Block 2 (GM Fault Block 2) volume:

In this approach the petropehysical interpolation is confined within the meshes of each of the formations. The procedure start with extracting the mesh for each of the formation output volumes in the GM Fault Block 2 (no. 2). The petrophysical values for all the wells are interpolate, but the result is constrained within the formation volume of the GM Fault Block 2. This procedure is one of the more hidden options in Leapfrog Geo.

4a. Interpolated model: The interpolated petrophysical values are concstrained within the GM Fault Block 2 volume and grouped to gether in intervalls. The porosity intervals have been hold constant, as shown in table 1. The permeability intervals has been decreased slightly (see table 2 below).

Permeability intervals [mD]
<10.0
10.0-40.0
40.0-80.0
80.0-100.0
100.0-130.0
>130.0

4b Block Model: The petrophysical values are estimated and shown as a block model of the GM Fault Block 2 volume. The dimensions of each grid cell is selected to be 70m x 70m x 40m.

4c Block Model: The dimensions of each grid cell is selected to be 40m x 40m x 10m.

4d Block Model: The dimensions of each grid cell is selected to be 10m x 10m x 5m.

Chapter 6

Results

6.1 The Geological Model (GM)

The result of the GM model is shown in Fig. 6.1.1, colours for each of the formations is shown in the colour scale. A volume model of the entire field is a good visual representation of the structural and stratigraphic architecture of the reservoir. There has been an extrapolation of volume in the North corner (upper left), compared to the mesh triangulated mesh in Fig. 5.3.1. The volume along the East corner (lower right) has been too thin to be filled in with a proper volume.

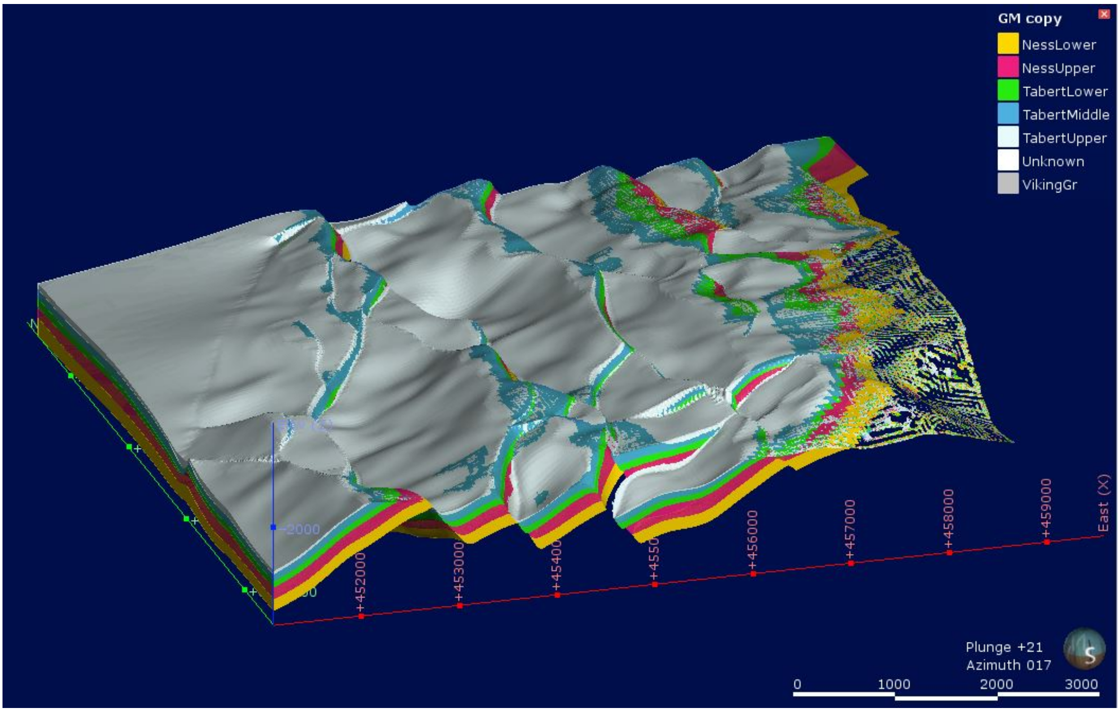
GM copy
NessLower
NessUpper
TabertLower
TabertMiddle
TabertUpper
Unknown
VikingGr
-2000
+452000
+453000
+45400
+4550
+456000
+457000
+458000
+459000
East (X)
Plunge +21
Azimuth 017
0
1000
2000
3000

Figure 6.1.1. GM volume model of the field, Viking Gp. and the "unknown" formation is excluded.

6.2 The Geological Model Fault Block 2 (GM Fault Block 2)

The volume model in Fig. 6.1.1 consists of several fault block models. In Fig. 6.2.1 "GM Fault Block 2" is shown. Two wells, C2 and C4, are located on the fault block and is marked in the figure. The area is closed by the faults; *Main Faults NS 1, Main Faults NS 2, Main Faults West 1, Main Faults West 2a*, the *NNE-SSW* and *Boundary Fault West* in West, South and East direction. Location of faults is shown in Fig. 5.2.4.

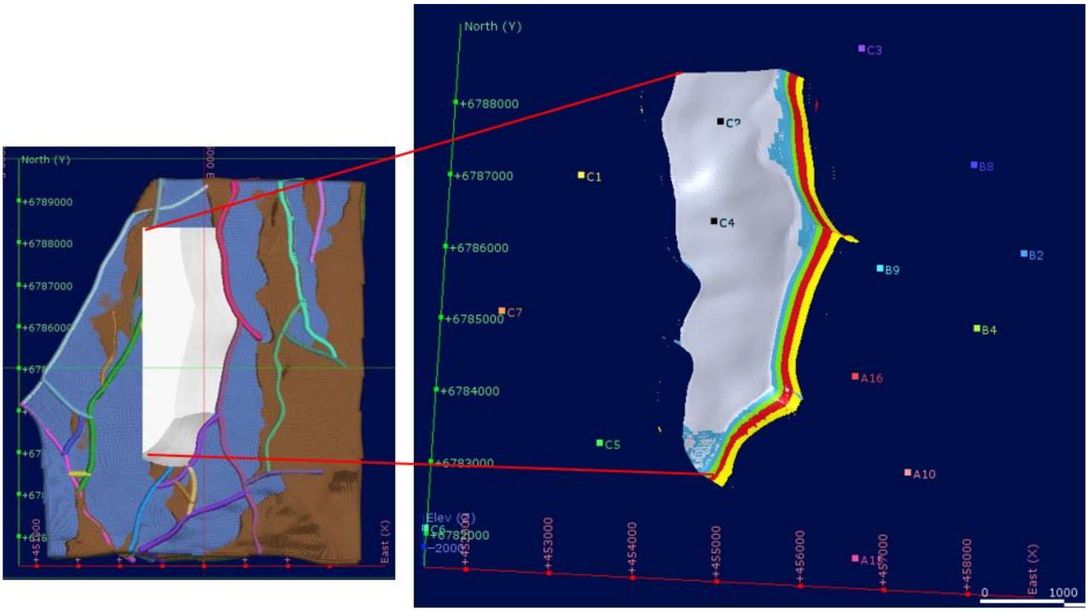
North (Y)
+6789000
+6788000
+6787000
+6786000
East (X)
North (Y)
+6788000
+6787000
+6786000
+6785000
+6784000
+6783000
+6782000
Elev (Z)
-2000
+453000
+454000
+455000
+456000
+457000
+458000
East (X)
0
1000
C1
C2
C3
C4
C5
C6
C7
B2
B4
B8
B9
A10
A16

Figure 6.2.1. A (Left): Scale and placement map for figure B) from iso-surfaces. The blue area in the figure is the Viking Gp. surface and brown is the Upper Tarbert surface. Location of faults is marked. B (Right): GM Fault Block 2. Formation colours are the same as in Fig. 6.1.1. Wells within selected volume is C2 and C4.

6.3 Petrophysical model of the Geological Model (GM) volum

6.3.1 Interpolated model

The petrophysical models is limited by the total volume of the Geological Model (GM). The Fig. 6.3.1 shows the interpolation of the porosity property. From Top Tarbert can it be seen that the porosity is largest in the South-East corner and decreases towards North-West. The four colours in the figure, from green to orange, corresponds with the porosity interval values in table 1 in Chap. 5.3.3.

The interpolated permeability properties confined in the GM volume model can be seen in Fig. 6.3.2. Also in this figure do the colours correspond with the interval values, dark blue is the lowest interval and increases towards yellow. The 3D permeability model in Fig. 6.3.2B reviles that the permeability trend is not so evenly distributed as in the porosity model. For instance green islands is located around the A16 well and a blue island around the C5 well.

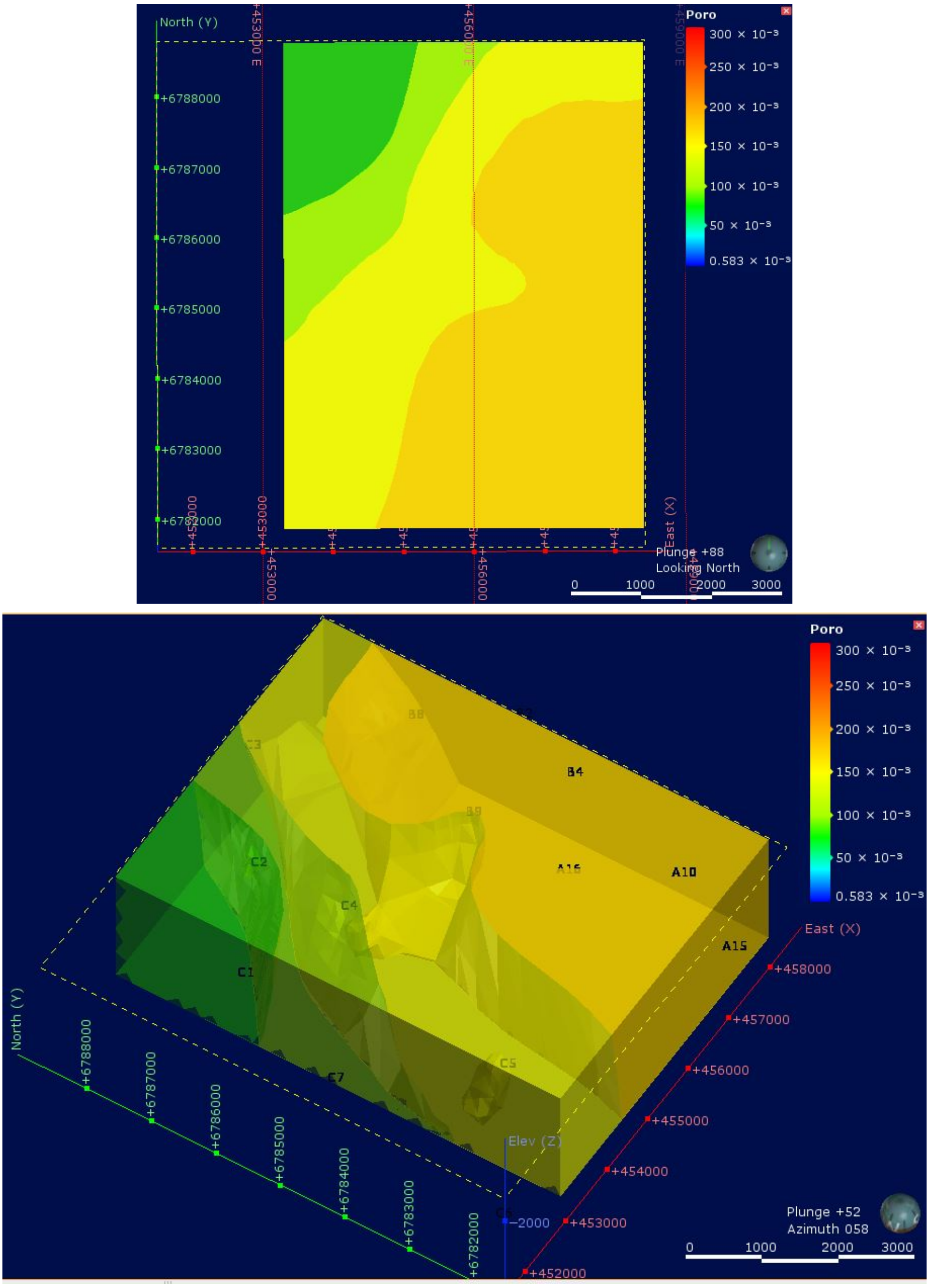
North (Y)
+6788000
+6787000
+6786000
+6785000
+6784000
+6783000
+6782000
+453000 E
+456000 E
+459000 E
+453000
+456000
East (X)
Poro
300 × 10⁻³
250 × 10⁻³
200 × 10⁻³
150 × 10⁻³
100 × 10⁻³
50 × 10⁻³
0.583 × 10⁻³
Plunge +88
Looking North
0
1000
2000
3000
B8
C3
B4
B9
C2
A16
A10
C4
C1
A15
C5
C7
East (X)
+458000
+457000
+456000
+455000
+454000
+453000
+452000
Elev (Z)
-2000
North (Y)
+6788000
+6787000
+6786000
+6785000
+6784000
+6783000
+6782000
Plunge +52
Azimuth 058
0
1000
2000
3000

Figure 6.3.1. A (Upper): Porosity GM volume model seen from Top Tarbert. B (Lower): Well placement marked on the 3D model, the opacity and z-axis is increased.

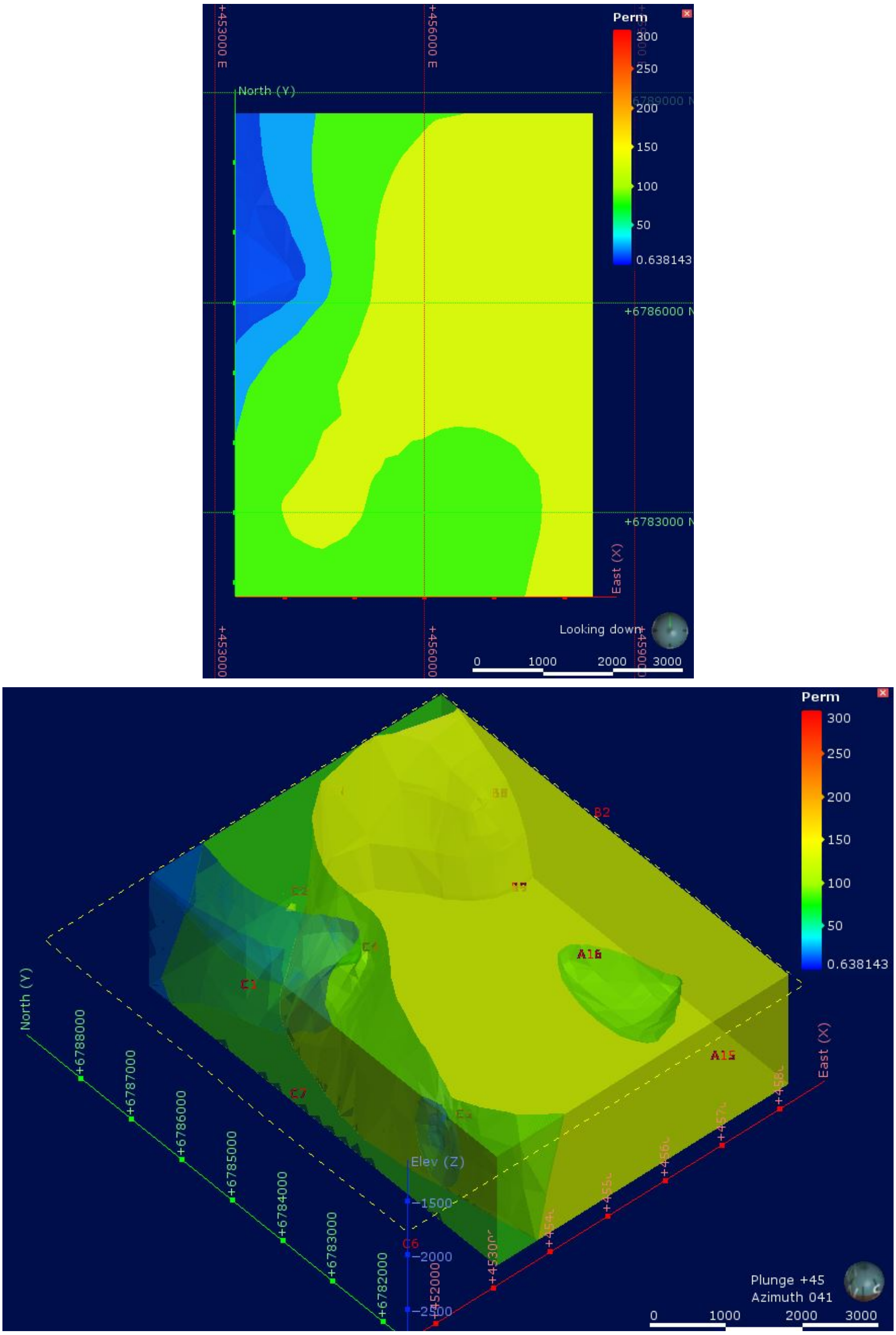
+453000 E
+456000 E
North (Y)
Perm
300
250
200
150
100
50
0.638143
+6789000 N
+6786000 N
+6783000 N
East (X)
Looking down
0
1000
2000
3000
B1
B2
B3
C2
C4
C1
C7
C3
A16
A15
C6
Elev (Z)
-1500
-2000
-2500
+6788000
+6787000
+6786000
+6785000
+6784000
+6783000
+6782000
+452000
+453000
+454000
+455000
+456000
+457000
+458000
Plunge +45
Azimuth 041

Figure 6.3.2. A (Upper): Permeability volume model B (Lower): Well placement marked on the 3D model, the opacity and z-axis is increased.

6.3.2 Block Model

The result of the block model for porosity is shown in Fig. 6.3.3 and permeability in Fig. 6.3.4. The block model has grid cells with dimensions 40m x 40m x 10m. The total number of blocks is 128 x 173 x 150 = 3,321,600. The outer grids is removed for visual purposes, but is still partially visible inside the model.

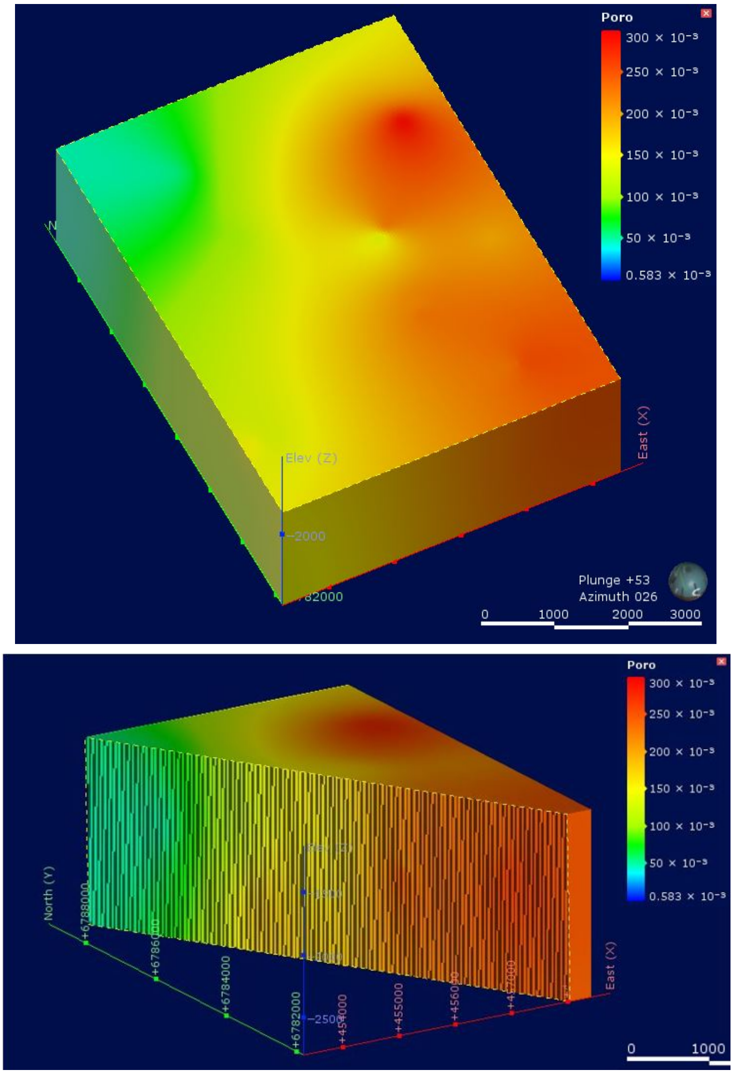
Poro
300 × 10⁻³
250 × 10⁻³
200 × 10⁻³
150 × 10⁻³
100 × 10⁻³
50 × 10⁻³
0.583 × 10⁻³
Elev (Z)
-2000
East (X)
82000
Plunge +53
Azimuth 026
0
1000
2000
3000
Poro
300 × 10⁻³
250 × 10⁻³
200 × 10⁻³
150 × 10⁻³
100 × 10⁻³
50 × 10⁻³
0.583 × 10⁻³
North (Y)
+6788000
+6786000
+6784000
+6782000
-2500
+454000
+455000
+456000
+457000
East (X)
0
1000

Figure 6.3.3. A (Left): Porosity block model. B (Right): Cut-through, diagonal from North to East corner. The blocks are visible from inside.

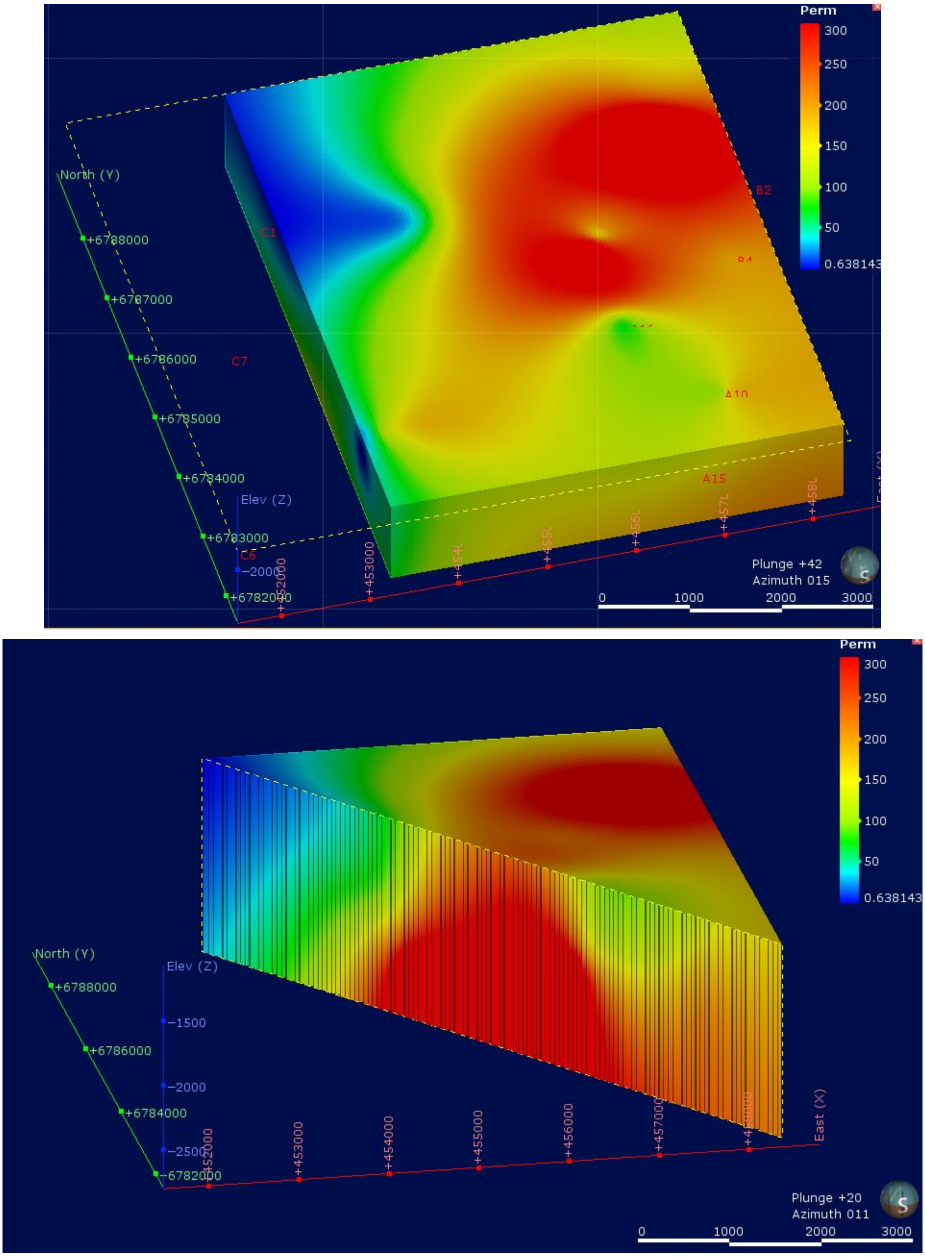
Perm
300
250
200
150
100
50
0.638143
North (Y)
+6788000
+6787000
+6786000
+6785000
+6784000
+6783000
+6782000
Elev (Z)
-2000
C1
C7
C6
B2
A10
A15
+452000
+453000
+454L
+455L
+456L
+457L
+458L
Plunge +42
Azimuth 015
0
1000
2000
3000
Perm
300
250
200
150
100
50
0.638143
North (Y)
+6788000
+6786000
+6784000
-6782000
Elev (Z)
-1500
-2000
-2500
+452000
+453000
+454000
+455000
+456000
+457000
+458000
East (X)
Plunge +20
Azimuth 011
0
1000
2000
3000

Figure 6.3.4. A (Left): Permeability block model. B (Right): Cut-through, diagonal from North to East corner. The blocks are visible from inside. Z-axis is increased.

6.4 Petrophysical model of the Geological Model Fault Block 2 (GM Fault Block 2) volume

The interpolated petrophysical is confined to the GM Fault Block 2. Figure 6.2.1 shows the placement of this fault block.Two well are located on the block, C2 and C4, but all the petrophysical well data is used during the interpolation and estimation.

The selected volume can be used to characterise the petrophysical properties on a formation level. All the models result in this chapter can be divided into individual formations.

6.4.1 Interpolated model

A complete selection of figures and corresponding statistics is gathered in Appendix B.1.

An example is the Upper Tarbert formation in Fig. 6.4.1, where the interpolated porosity values are mainly within the 0.082-0.118 porosity interval. The interpolated permeability values gradually increases towards North.

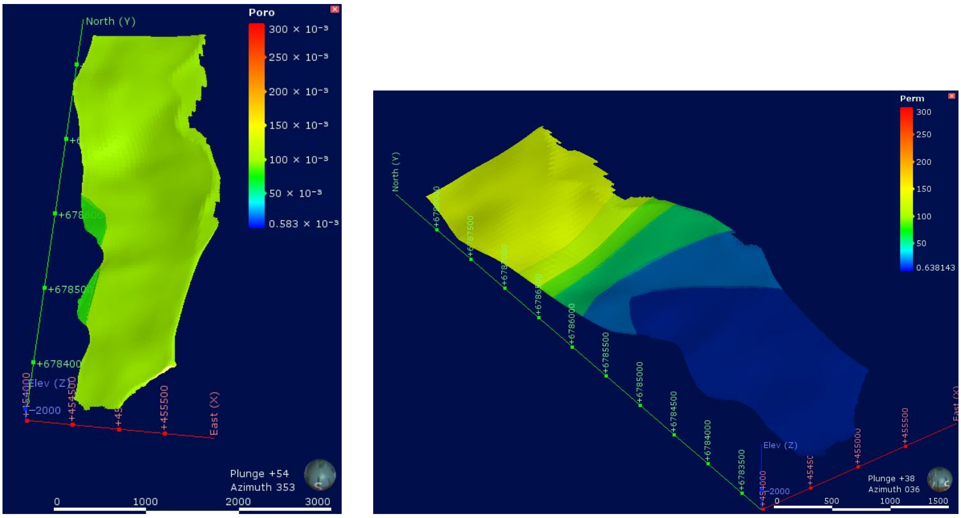
North (Y)
Poro
300×10^{-3}
250×10^{-3}
200×10^{-3}
150×10^{-3}
100×10^{-3}
50×10^{-3}
0.583×10^{-3}
Elev (Z)
-2000
East (X)
Plunge +54
Azimuth 353
0
1000
2000
3000
Perm
300
250
200
150
100
50
0.638143
North (Y)
+6787500
+6786000
+6785500
+6785000
+6784500
+6784000
+6783500
Elev (Z)
-2000
+455000
+455500
East (X)
Plunge +38
Azimuth 036
0
500
1000
1500

Figure 6.4.1. Upper Tarbert porosity GM Fault Block 2 volume model. A (Left): Interpolated porosity. B (Right): Interpolated permeability.

6.4.2 Block model: Grid cells 70m x 70m x 40m

In this case is grid cells with dimension 70m x 70m x 40m selected. Fig. 6.4.2 illustrates the number of blocks in the model and how the blocks are divided within each formation.

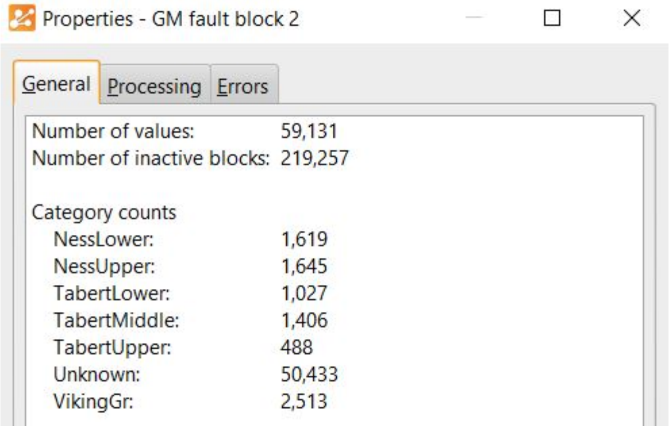

Number of values:	59,131
Number of inactive blocks:	219,257
Category counts	
NessLower:	1,619
NessUpper:	1,645
TabertLower:	1,027
TabertMiddle:	1,406
TabertUpper:	488
Unknown:	50,433
VikingGr:	2,513

Figure 6.4.2. Number of blocks for each formation, "Unknown" is surrounding blocks that is inactive in this thesis.

The results are not very successful. The formation appears to be to thin to be defined within the grid cell some places. For instance in the Upper Tarbert formation, Fig. 6.4.3. The Upper Ness formation in Fig. 6.4.4 shows how the grid looks like when it is continuous trough the formation.

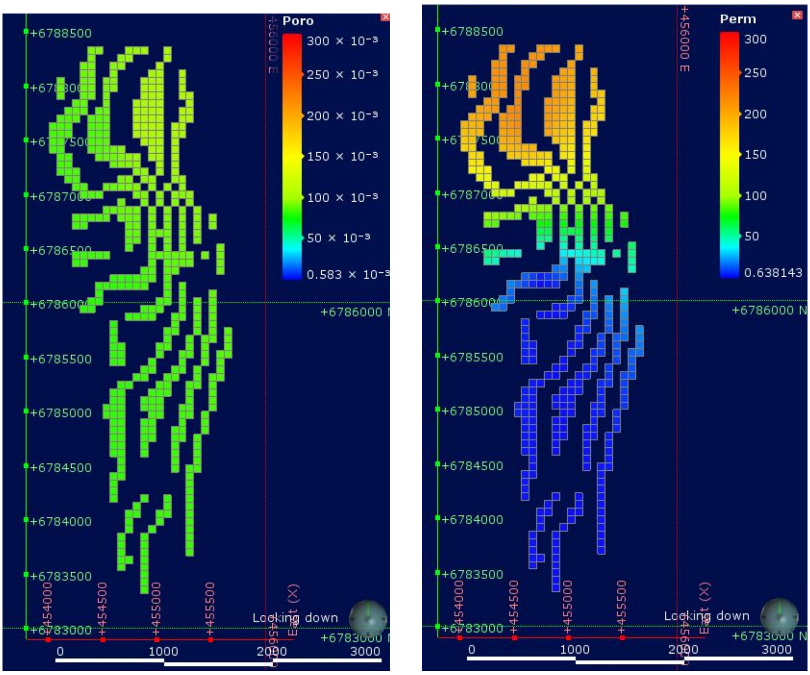
Poro
300 × 10⁻³
250 × 10⁻³
200 × 10⁻³
150 × 10⁻³
100 × 10⁻³
50 × 10⁻³
0.583 × 10⁻³
+6788500
+6787000
+6786500
+6786000
+6785500
+6785000
+6784500
+6784000
+6783500
+6783000
+454000
+454500
+455000
+455500
456000 E
+6786000 N
East (X)
Looking down
0
1000
2000
3000
Perm
300
250
200
150
100
50
0.638143

Figure 6.4.3. Upper Tarbert porosity GM Fault Block 2 volume model. A (Left): Porosity. B (Right): Permeability.

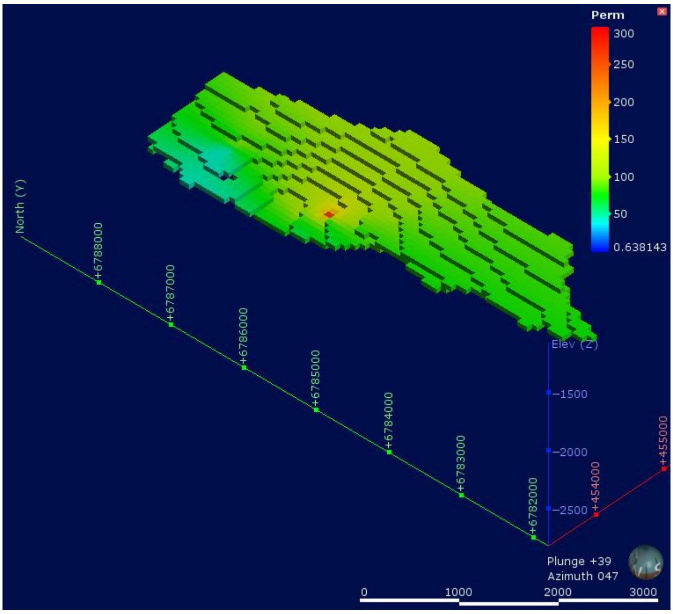
Perm
300
250
200
150
100
50
0.638143
North (Y)
+6788000
+6787000
+6786000
+6785000
+6784000
+6783000
+6782000
Elev (Z)
−1500
−2000
−2500
+454000
+455000
Plunge +39
Azimuth 047
0
1000
2000
3000

Figure 6.4.4. Upper Ness permeability block model

6.4.3 Block model: Grid cells 40m x 40m x 10m

In this case is grid cells with dimension 40m x 40m x 10m selected. Fig. 6.4.5 illustrates the number of blocks in the model and how the blocks are divided within each formation. The Upper Tarbert formation is used as an example below. Fig. 6.4.6 shows the porosity block model and the Fig. 6.4.6 shows the permeability block model. A complete selection of figures can be found in Appendix B.2. Fig. 6.4.8 shows a North-South snit through all the formation with estimated permeability values. It can be observed that the Tarbert formation has the largest variation in permeability values. The red area in the Ness Upper formation corresponds with well C4.

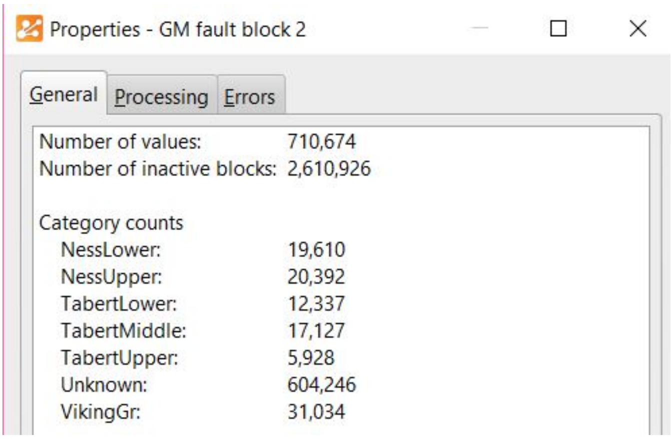

Number of values: 710,674
Number of inactive blocks: 2,610,926

Category counts

NessLower:	19,610
NessUpper:	20,392
TabertLower:	12,337
TabertMiddle:	17,127
TabertUpper:	5,928
Unknown:	604,246
VikingGr:	31,034

Figure 6.4.5. Number of blocks for each formation, "Unknown" is surrounding blocks that is inactive in this thesis.

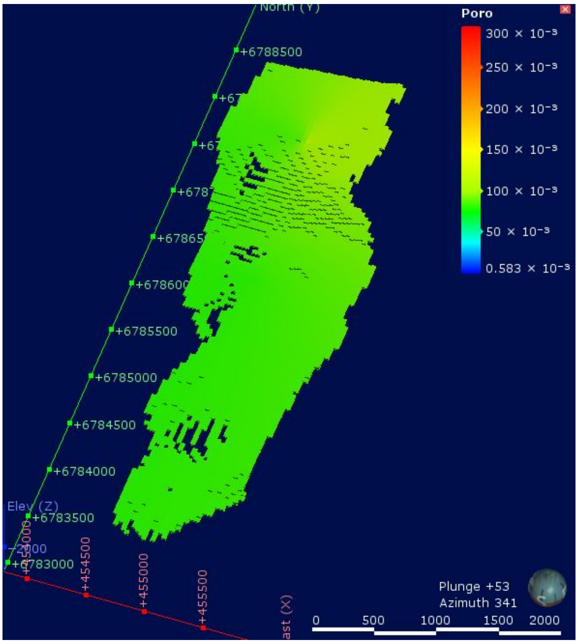
North (Y)
+6788500
+6783500
+6783000
+6785500
+6785000
+6784500
+6784000
Elev (Z)
-2000
+454500
+455000
+455500
East (X)
Poro
300×10^{-3}
250×10^{-3}
200×10^{-3}
150×10^{-3}
100×10^{-3}
50×10^{-3}
0.583×10^{-3}
Plunge +53
Azimuth 341
0
500
1000
1500
2000

Figure 6.4.6. Upper Tarbert porosity block model.

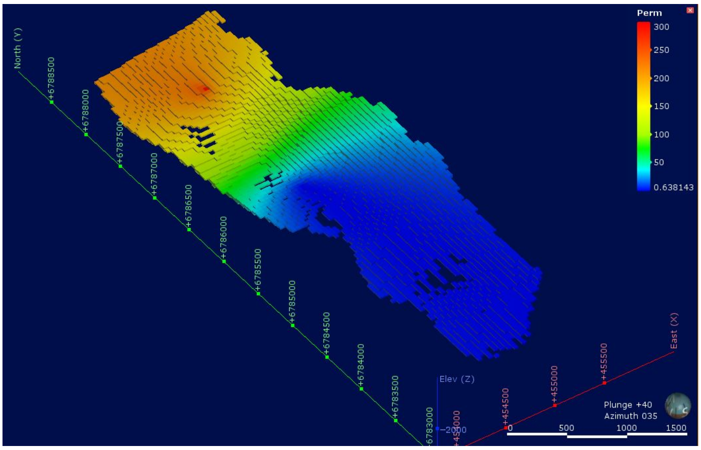
Perm
300
250
200
150
100
50
0.638143
North (Y)
+6788500
+6788000
+6787500
+6787000
+6786500
+6786000
+6785500
+6785000
+6784500
+6784000
+6783500
+6783000
Elev (Z)
-2000
+454500
+455000
+455500
East (X)
Plunge +40
Azimuth 035
0
500
1000
1500

Figure 6.4.7. Upper Tarbert permeability block model.

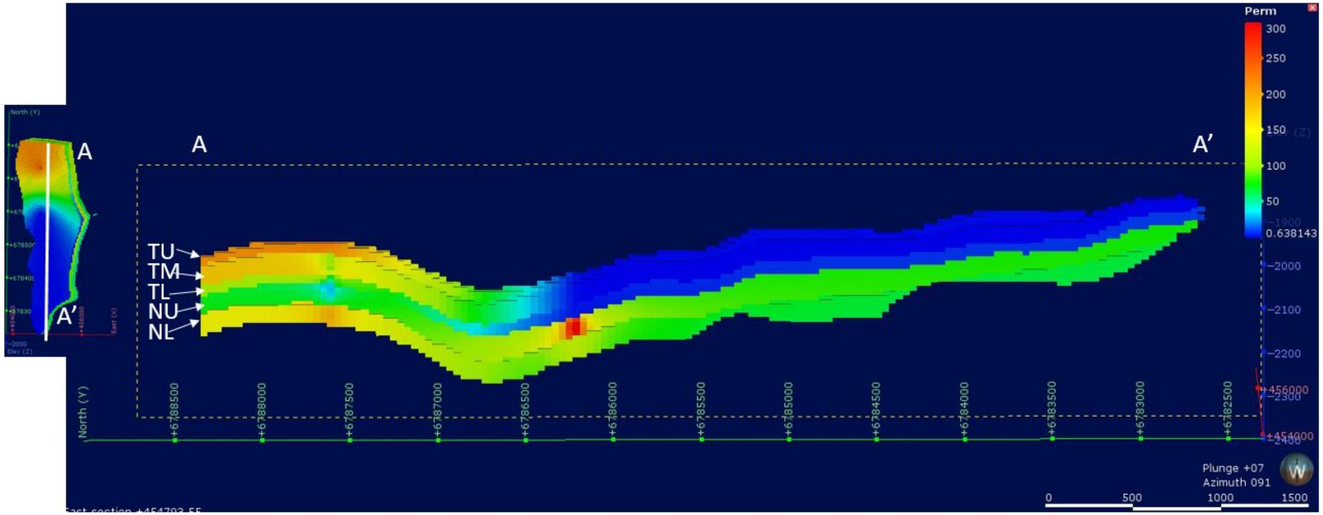
A
A'
TU
TM
TL
NU
NL
Perm
300
250
200
150
100
50
0.638143
−2000
−2100
−2200
North (Y)
+6788500
+6788000
+6787500
+6787000
+6786500
+6786000
+6785500
+6785000
+6784500
+6784000
+6783500
+6783000
+6782500
Plunge +07
Azimuth 091
0
500
1000
1500

Figure 6.4.8. Cut through the permeability block model of all the formations. TU = Tarbert Upper, TM = Tarbert Middle, TL = Tarbert Lower, NU = Ness Upper and NL = Ness Lower.

6.4.4 Block model: Grid cells 10m x 10m x 5m

The computer could not handle the calculations and the procedure therefore did not yield any results.

Chapter 7

Discussion and Conclusion

This thesis aims to characterise the spatial petrophysical distribution of porosity and permeability in the Tarbert and Ness Formation at the Gullfaks Field. The geomodelling software Leapfrog Geo was used to build a reservoir model and estimate the spatial petrophysical properties. Four different procedures were used to obtain the results. In this chapter the results from the modelling process is discussed.

7.1 Input data and method

The petrophysical properties porosity and permeability was extensively discussed in Chap. 2. These properties are obtained from core samples, measured every 0.5 m. The core samples has a relatively dense sampling interval, but the quality of the data is unknown.

The wells samples a small volume of the reservoir volume, and the petrophysical properties obtained from the cores are mainly on a microscopic level. In this thesis the petrophysical properties were characterised on a formation scale in the reservoir model. The petrophysical properties were interpolated from the well data with the radial basic function (RBF) and estimated for the entire field in the block model. In order to populate the block block model with estimated values, the representative elementary volume (REV) for each petrophysical property had to be upscaled (Chap. 2.3.1) with several orders of magnitude. Leapfrog Geo treats the petrophysical properties as individual, but equal variables, and do not recognise porosity as an additive property and permeability as a non-additive property (Chap. 2.1.4). Therefore it is a relatively large uncertainty related to the upscaling of these properties, and it is unclearer exactly how this software handles upscaling of variables. The "black-box" phenomena was briefly mentioned in Chap. 5.3, and shows that the software in itself can be source to uncertainty.

The framework in the reservoir model constitutes of formation surfaces and faults. A total of seven surfaces and 22 faults were implemented. The framework was implemented in the model as scatter-points originating from seismic. This method was necessary because Leapfrog Geo is built for GiS-data, and not seismic (like e.g. PETREL). The surfaces were interpolated using triangulation, while the faults were interpolated by RBF. The framework is used to limit the reservoir volume and defines the volume the petrophysical properties are evaluated within.

By choosing to work with a deterministic modelling tool, and therefore also a data-driven generic approach (Chap. 5.1.2), the input data are honoured deterministically in the model. Meaning that the users ability to change the outcome of the computer algorithm is limited. The challenge with this process is that the algorithm relays on the underlying data set, which for most reservoirs is statistically insufficient (Ringrose and Bentley, 2015).

7.2 Results

The result of the Geological Model (GM) in Chap. 6.1 is a volume model that can be used to visualise the field. The faults are not implemented in Fig. 6.1.1. to increase visualisation, but they can be added to the model. The reason behind building this model and the GM Fault Block 2 model (Chap. 6.2) was to constrain the volume for the petrophysical models.

The results of the petrophysical model of the Geological Model(GM) volume in Chap. 6.3 was poor. Volume control was difficult because the model can not be divided into formations. The interval values used in the intropetation models in Chap. 6.3.1, is by default selected from the histogram distributions in Fig. 5.2.7. This approach seems to work well with the porosity values, which is relatively even distributed. However, for the permeability values the intervals are probably to large, particularly for the intervals 40-130 mD and > 130 mD .groups which has a large spread in data values.

The most striking feature in the property models are the "islands" of very strongly coloured areas with sharp boundaries to the surrounding estimations. For instance the yellow area around well C4 in Fig. 6.3.1, the green area around well A16 i Fig. 6.3.2 and the red circles in Fig. 6.3.4. Ringrose and Bentley (2015) refers to these features as "bull-eyes", and suggest they occur when the algorithm did not match the element proportions of the wells with the frequency distribution at the wells. The occurrence of bulls-eyes is dependent on the well spacing, indicating that a regular spaced well pattern would yield the best result. For most petroleum fields are not regular spaced wells realistic.

The procedure used in the petrophysical model of the Geological Model Fault Block 2 (GM Fault Block 2) volume, yielded the best result. The volumes were confined within both the reservoir block and the formations. The porosity intervals were hold constant because the result showed a relatively low variability i distribution.

The all the interpolated models are collected in Appendix B.1., from the porosity models it can be seen that the lower and intermediate intervals are most common. The permeability intervals were decreased based on the observations from Chap. 6.3.1. Choosing an increased number of intervals yields a more subtle distribution of the permeability values.

Three different grid cell dimensions were chosen in the block model; 70m x 70m x 40m, 40m x 40m x 10m and 10m x 10m x 5m. The 70m x 70m x 40m dimension gave limited results, some of the formations were probably to thin to be captured properly within the cells (e.g. Upper Tarbert, Fig. 6.4.3).

The 40m x 40m x 10m dimension on the block cells yielded the best result. All the figures are located in Appendix B.2. Compared to the 70m x 70m x 40m grid celled block model, these block models are smoother, but seems to capture the heterogeneous distribution of the petrophysical properties better. The smoothness of the model is relatively low in this case, but it shows that it is a constrain on how low the cell block dimensions can be before loosing structure of the model.

The model with 10m x 10m x 5m dimension grid cells did not yield a result. Indicating that computer power also is a constrain on the number of cell blocks in a model.

Interpreting the results of petrophysical models on field scale in a geological context is challenging. In Chap. 4, Geological Model, were the correlation between facies and petrophysical values discussed. The petrophysical surface models shown in Fig. 4.3.2 and 4.3.1 can not be compared to the results of this model, manly due to the different data amount and the stochastic modelling algorithm. Fig. 6.4.8 is a collection of all the permeability formation block models with block size 40m x 40m x 10m. By interpreting this model, a shift in properties can be detected between Ness Upper Formation and the Tarbert Lower Formation. Particularly the Tarbert Middel and Tarbert Upper Formation has a larger variety in petrophysical properties and probably also facies. The southern area of these formations has a low permeability value that can indicate a high shale content, while the northern part of the formations have higher permeability values and can contain more sand. It almost looks like the lower permeability values (blue colour) in Tarbert Middel and Tarbert Upper Formation is back-stepping like it was described for the Cliff house sandstone in Fig. 4.1.6.

7.3 Conclution

The advantage of using Leapfrog Geo and a deterministic modelling approach is that the results can be retrieved relatively fast compared to e.g. stochastic model builders. Even with a very limited source of data it was possible to produce a porosity and a permeability model that honours the input well data and gives an estimation for the remaining area of the field.

Pixel-based methods have mainly been used for facies (rock) modelling (e.g. Deutsch (2006); Yao and Chopra (2000)). In this case the deterministic, implicit software Leapfrog Geo, was used to characterise petrophysical properties. Few, if any previous studies have used this software for an offshore petroleum field.

The study concludes that:

- Leapfrog Geo is suitable to characterise petrophysical properties in a reservoir model where the main data source is well data. However, with additional data sources, are probably other types of software preferable.
- the radial basic function (RBF) is suitable to interpolate and estimate fault iso-surfaces and petrophysical data. However, not formation iso-surfaces that had to be triangulated.
- the Geological Model Fault Block2 (GM Fault Block 2) volume procedure yielded the best result, because of the good volume control both within the fault block and the formations.
- a 40m x 40m x 10m grid cell size yielded the best result.
- grid cell size is constrained both by smoothness and computer power.

Leapfrog Geo is a estimation tool and is particularly useful to make geological models, for further work would it be interesting to implement the results in a simulation tool.

Bibliography

Allen, J. R. L.
1982a. *Sedimentary Structures: Their character and physical basis. Volume I.* Elsevier Scientific Publishing Company. Pp. 592.

Allen, J. R. L.
1982b. *Sedimentary Structures: Their character and physical basis. Volume II.* Elsevier Scientific Publishing Company. Pp. 662.

Allen, J. R. L.
1985. *Principles of physical sedimentology.* Allen and Unwin Ltd. Pp. 272.

Allen, P. A. and J. R. Allen
2013. *Basin analysis: Principles and application to petroleum play assessment, 3.ed.* John Wiley & Sons. Pp. 632.

Atkins, J. E. and E. F. McBride
1992. Porosity and packing of holocene river, dune, and beach sands (1). *AAPG Bulletin*, 76(3):339–355.

Badley, M., J. Price, C. R. Dahl, and T. Agdestein
1988. The structural evolution of the northern viking graben and its bearing upon extensional modes of basin formation. *Journal of the Geological Society*, 145(3):455–472.

Bale, A., H. Fossen, E. Berg, T. Kui, and Ø. Mjelde
2008. Comprehensive mini-frac testing in the gullfaks field as a tool for characterisation of reservoir structure and rock mechanics. In *International Petroleum Technology Conference.* International Petroleum Technology Conference.

Barrett, P.
1980. The shape of rock particles, a critical review. *Sedimentology*, 27(3):291–303.

Bear, J.
1988. *Dynamics of fluids in porous media.* Courier Corporation. Pp. 764.

Bear, J. and Y. Bachmat

1990. *Introduction to modeling of transport phenomena in porous media, 4.ed.* Springer Science & Business Media. Pp. 554.

Beard, D. and P. Weyl
1973. Influence of texture on porosity and permeability of unconsolidated sand. *AAPG Bulletin*, 57(2):349–369.

Bejan, A.
2004. Designed porous media: maximal heat transfer density at decreasing length scales. *International Journal of Heat and Mass Transfer*, 47(14):3073–3083.

Bejan, A., I. Dincer, S. Lorente, A. Miguel, and H. Reis
2004. *Porous and complex flow structures in modern technologies.* Springer Science & Business Media.

Bhattacharya, J. P.
2006. Deltas. In *Facies models revisited*, H. W. Posamentier and R. G. Walker, eds.

Bjørlykke, K.
2010. *Petroleum geoscience: From sedimentary environments to rock physics.* Springer Science & Business Media. Pp. 508.

Boggs, S.
2011. *Principles of sedimentology and stratigraphy, 5ed.* Prentice Hall Upper Saddle River. Pp. 585.

Box, G. E. P. and N. R. Draper
1987. *Empirical model-building and response surfaces*, volume 424. John Wiley & Sons, New York.

Boyd, R., R. Dalrymple, and B. Zaitlin
1992. Classification of clastic coastal depositional environments. *Sedimentary Geology*, 80(3):139–150.

Brayshaw, A. C., G. W. Davies, and P. W. M. Corbett
1996. Depositional controls on primary permeability and porosity at the bedform scale in fluvial reservoir sandstone. In *Advances in Fluvial Dynamics and Stratigraphy*, P. A. Carling and M. R. Dawson, eds., Pp. 373–394.

Brensdal, A. and C. Halvorsen
1992. Quantification of permeability variations across thin laminae in cross bedded sandstone. *Advances in Core Evaluation III: Reservoir Management*, Pp. 25–42.

Bridge, J. S.
2006. Fluvial facies models: Recent developments. In *Facies models revisited*, H. W. Posamentier and R. G. Walker, eds., volume 84, Pp. 85–170. SEPM (SOCIETY FOR SEDIMENTARY GEOLOGY).

Bridge, J. S. and M. R. Leeder
1979. A simulation model of alluvial stratigraphy. *Sedimentology*, 26(5):617–644.

Bruggeman, D.
1935. Effective medium model for the optical properties of composite materials. *Ann. Phys. Leipzig*, 24:636.

Caers, J.
2011. *Modeling Uncertainty in the Earth Sciences*. John Wiley & Sons. Pp. 248.

Caers, J. and T. Zhang
2004. Multiple-point geostatistics: a quantitative vehicle for integrating geologic analogs into multiple reservoir models. In *Integration of outcrop and modern analogs in reservoir modeling*, volume 80, Pp. 383–394. AAPG Special Volumes.

Carman, P.
1937. Fluid flow through granular beds. *Transactions-Institution of Chemical Engineeres*, 15:150–166.

Carr, J. C., R. K. Beatson, J. B. Cherrie, T. J. Mitchell, W. R. Fright, B. C. McCallum, and T. R. Evans
2001. Reconstruction and representation of 3d objects with radial basis functions. In *Proceedings of the 28th annual conference on Computer graphics and interactive techniques*, Pp. 67–76. ACM.

Chilès, J. and P. Delfiner
2009. *Geostatistics: Modeling Spatial Uncertainty*, Wiley Series in Probability and Statistics. Wiley. Pp. 720.

Cowan, E. J., R. K. Beatson, W. R. Fright, T. J. McLennan, and T. J. Mitchell
2002. Rapid geological modelling. *Applied Structural Geology for Mining Exploration and Mining. International Symposium (Kalgoorlie, 23-25 September 2002), Australia*, Pp. 23–25.

Cowan, E. J., R. K. Beatson, H. J. Ross, W. R. Fright, T. J. McLennan, J. C. Evans, TR. .and Carr, R. G. Lane, D. V. Bright, and A. J. Gillman
2003. Practical implicit geological modelling. In *Fifth International Mining Geology Conference*, Pp. 17–19.

Dalrymple, R. W., B. A. Zaitlin, and R. Boyd
1992. Estuarine facies models: conceptual basis and stratigraphic implications: perspective. *Journal of Sedimentary Research*, 62(6):1130–1146.

Davies, S., N. Dawers, A. McLeod, and J. Underhill
2000. The structural and sedimentological evolution of early synrift successions: the middle jurassic tarbert formation, north sea. *Basin Research*, 12(3-4):343–365.

Deutsch, C. V.
2006. A sequential indicator simulation program for categorical variables with point and block data: Blocksis. *Computers & Geosciences*, 32(10):1669–1681.

Deutsch, C. V. and L. Wang
1996. Hierarchical object-based stochastic modeling of fluvial reservoirs. *Mathematical Geology*, 28(7):857–880.

Dewan, J. T.
1983. *Essentials of modern open-hole log interpretation.* PennWell Books. Pp. 361.

Doligez, B., H. Beucher, F. Geffroy, and R. Eschard
1999. Integrated reservoir characterization: Improvement in heterogeneous stochastic modeling by integration of additional external constraints. *AAPG Special Volumes*, 71:333–341.

Ellefmo, S. L. and E. Larsen
2013. Innføring i geostatistikk, compendium. *Institutt for geologi og bergteknikk, NTNU.*

Eschard, R., B. Tveiten, G. Desaubliaux, J. C. Lecomte, and F. S. P. Van Buchem
1993. High resolution sequence stratigraphy and reservoir prediction of the brent group (tampen spur area) using an outcrop analogue. In *Subsurface Reservoir Characterization from Outcrop Observations: Proceedings of the 7th IFP Exploration and Production Research Conference, Scarborough, April 12-17, 1992*, number 51, Pp. 1–35.

Færseth, R.
1996. Interaction of permo-triassic and jurassic extensional fault-blocks during the development of the northern north sea. *Journal of the Geological Society*, 153:931–944.

Fält, L., R. Helland, V. W. Jacobsen, and D. Renshaw
1989. Correlation of transgressive-regressive depositional sequences in the middle jurassic brent/vestland group megacycle, viking graben, norwegian north sea. In *Correlation in hydrocarbon exploration*, J. D. Collinson, ed., Pp. 191–200. Springer Netherlands.

Fjellanger, E., T. R. Olsen, and J. L. Rubino
1996. Sequence stratigraphy and palaeogeography of the middle jurassic brent and vestland deltaic systems, northern north sea. *Norsk Geologisk Tidsskrift*, 76:75–106.

Folkestad, A., T. Odisen, H. Fossen, and M. A. Pearce
2014. Tectonic influence on the jurassic sedimentary architecture in the northern north sea with focus on the brent group. Pp. 389–415. John Wiley & Sons, Ltd, Chichester, UK.

Fossen, H. and J. Hesthammer
1998. Structural geology of the gullfaks field, northern north sea. *Special publication-Geological Society of London*, 127:231–262.

Fossen, H. and J. Hesthammer

2000. Possible absence of small faults in the gullfaks field, northern north sea: implications for downscaling of faults in some porous sandstones. *Journal of Structural Geology*, 22(7):851–863.

Fossen, H., T. Odinsen, R. B. Færseth, and R. H. Gabrielsen
2000. Detachments and low-angle faults in the northern north sea rift system. *Special Publication-Geological Society Of London*, 167:105–132.

Fossen, H. and A. Rørnes
1996. Properties of fault populations in the gullfaks field, northern north sea. *Journal of Structural Geology*, 18(2):179–190.

Fraser, H.
1935. Experimental study of the porosity and permeability of clastic sediments. *The Journal of Geology*, Pp. 910–1010.

Gabrielsen, R., R. Færseth, R. Steel, S. Idil, and O. Kløvjan
1990. Architectural styles of basin fill in the northern viking graben. *Tectonic evolution of the North Sea rifts*, 181:158–179.

Georgiadis, J. G. and I. Catton
1987. Stochastic modeling of unidirectional fluid transport in uniform and random packed beds. *Physics of Fluids (1958-1988)*, 30(4):1017–1022.

Georgiadis, J. G. and I. Catton
1988. Dispersion in cellular thermal convection in porous layers. *International journal of heat and mass transfer*, 31(5):1081–1091.

Gibbons, K., C. Halvorsen, and E. Siring
1993. Vertical and horizontal permeability variation within a sandstone reservoir based on minipermeameter measurements. *Marine and petroleum geology*, 10(4):325–334.

Graton, L. C. and H. Fraser
1935. Systematic packing of spheres: with particular relation to porosity and permeability. *The Journal of Geology*, Pp. 785–909.

Graue, E., W. Helland-Hansen, J. Johnsen, L. Lømo, A. Nøttvedt, K. Rønning, A. Ryseth, and R. Steel
1987. Advance and retreat of brent delta system, norwegian north sea. In *Petroleum geology of north west Europe*, Pp. 915–937. Graham and Trotman London.

Hallam, A.
1977. Secular changes in marine inundation of ussr and north america through the phanerozoic. *Nature*, 269:769–772.

Hampson, G. J., P. J. Sixsmith, and H. D. Johnson
2004. A sedimentological approach to refining reservoir architecture in a mature hydrocarbon province: the brent province, uk north sea. *Marine and Petroleum Geology*, 21(4):457–484.

Haq, B. U., J. Hardenbol, and P. R. Vail
1987. Chronology of fluctuating sea levels since the triassic. *Science*, 235(4793):1156–1167.

Hardy, R. L.
1971. Multiquadric equations of topography and other irregular surfaces. *Journal of geophysical research*, 76(8):1905–1915.

Hassanizadeh, M. and W. G. Gray
1983. *General conservation equations for multiphase systems 1: Averaging procedure*, Pp. 1–16. A computational mechanics Publication. CML Publications.

Helland-Hansen, W., M. Ashton, L. Lømo, and R. Steel
1992. Advance and retreat of the brent delta: recent contributions to the depositional model. *Geological Society, London, Special Publications*, 61(1):109–127.

Hesthammer, J. and H. Fossen
1997. The influence of seismic noise in structural interpretation of seismic attribute maps. *First Break*, 15(6):209–219.

Holden, L., R. Hauge, Ø. Skare, and A. Skorstad
1998. Modeling of fluvial reservoirs with object models. *Mathematical Geology*, 30(5):473–496.

Husmo, T., G. Hamar, O. Høiland, E. Johannessen, A. Rømuld, A. Spencer, and R. Titterton
2003. Lower and middle jurassic. *The Millennium Atlas: Petroleum Geology of the Central and Northern North Sea. Geological Society, London*, Pp. 129–155.

Isaaks, E. H. and R. M. Srivastava
1989. *An introduction to applied geostatistics.* Oxford University Press. Pp. 561.

Jennette, D. C. and C. O. Riley
1996. Influence of relative sea-level on facies and reservoir geometry of the middle jurassic lower brent group, uk north viking graben. *Geological Society, London, Special Publications*, 104(1):87–113.

Jensen, J. L., P. W. M. Corbett, G. E. Pickup, and P. S. Ringrose
1996. Permeability semivariograms, geological structure, and flow performance. *Mathematical Geology*, 28(4):419–435.

Jensen, J. L., L. W. Lake, P. W. M. Corbett, and D. J. Goggin
2000. *Statistics for petroleum engineers and geoscientists, 2.ed.* Elsevier, Amsterdam. Pp. 338.

Johannessen, E. R., R. Mjøs, D. Renshaw, A. Dalland, and T. Jacobsen
1995. Northern limit of the "brent delta" at the tampen spur—a sequence stratigraphic approach for sandstone prediction. *Norwegian Petroleum Society Special Publications*, 5:213–256.

Journel, A. G. and F. G. Alabert
1990. New method for reservoir mapping. *Journal of Petroleum technology*, 42(02):212–218.

Journel, A. G. and C. J. Huijbregts
1978. *Mining geostatistics*. Academic press. Pp. 600.

Kingston, D., C. Dishroon, and P. Williams
1983. Global basin classification system. *AAPG bulletin*, 67(12):2175–2193.

Lantuéjoul, C.
2013. *Geostatistical simulation: models and algorithms*. Springer Science and Business Media. Pp. 256.

Lee, D.-T. and B. J. Schachter
1980. Two algorithms for constructing a delaunay triangulation. *International Journal of Computer & Information Sciences*, 9(3):219–242.

Løseth, T. M., A. E. Ryseth, and M. Young
2009. Sedimentology and sequence stratigraphy of the middle jurassic tarbert formation, oseberg south area (northern north sea). *Basin Research*, 21(5):597–619.

Lucia, F. J.
2007. *Carbonate reservoir characterization: an integrated approach*. Springer Science & Business Media. Pp. 336.

MacDonald, A. C. and J. O. Aasen
1994. A prototype procedure for stochastic modeling of facies tract distribution in shoreface reservoirs. *AAPG Special Volumes*, Pp. 91–108.

Mallet, J. L.
2002. *Geomodeling*. Oxford University Press, Inc. Pp. 624.

Matheron, G.
1967. *Eléments pour une théorie des milieux poreux*. Masson. Pp. 168.

Middleton, G. V.
1976. Hydraulic interpretation of sand size distributions. *The Journal of Geology*, 84:405–426.

Mjøs, R.
2009. Anatomy of the seaward steps and seaward termination of the brent clastic wedge. *Basin Research*, 21(5):573–596.

Narasimhan, T. N.
1983. *A note on volume averaging*, Pp. 46–50. A computational mechanics Publication. CML Publications.

Nield, D. A. and A. Bejan
2012. *Mechanics of Fluid Flow Through a Porous Medium*. Springer Science & Business Media. Pp. 778.

Nordahl, K.
2004. *A petrophysical evaluation of tidal heterolithic deposits: Application of a near wellbore model for reconciliation of scale dependent well data.* PhD thesis, Fakultet for ingeniørvitenskap og teknologi, NTNU.

Nordahl, K. and P. S. Ringrose
2008. Identifying the representative elementary volume for permeability in heterolithic deposits using numerical rock models. *Mathematical geosciences*, 40(7):753–771.

NPD-Factpages
2015. Gullfaks field, (accessed 04.10.2015). `http://factpages.npd.no`.

Nutting, P. G.
1930. Physical analysis of oil sands. *AAPG Bulletin*, 14(10):1337–1349.

Nøttvedt, A., R. Gabrielsen, and R. Steel
1995. Tectonostratigraphy and sedimentary architecture of rift basins, with reference to the northern north sea. *Marine and Petroleum Geology*, 12(8):881–901.

Olaussen, S., L. Beck, L. M. Falt, E. Graue, K. G. Jacobsen, O. A. Malm, and D. South
1992. Gullfaks field-norway east shetland basin, northern north sea. *AAPG Special Volumes*, Pp. 55–83.

Petterson, O., A. Storli, E. Ljosland, and I. Massie
1990. *The Gullfaks field: geology and reservoir development.* Springer Netherlands.

Pöppelreiter, M. C., M. A. Balzarini, B. Hansen, and R. Nelson
2008. Realizing complex carbonate facies, diagenetic and fracture properties with standard reservoir modelling software. *Geological Society, London, Special Publications*, 309(1):39–49.

Pryor, W. A.
1973. Permeability-porosity patterns and variations in some holocene sand bodies. *AAPG Bulletin*, 57(1):162–189.

Pyrcz, M. J. and C. V. Deutsch
2014. *Geostatistical reservoir modeling.* Oxford University Press. Pp. 433.

Ramm, M.
1992. Porosity-depth trends in reservoir sandstones: theoretical models related to jurassic sandstones offshore norway. *Marine and Petroleum Geology*, 9(5):553–567.

Ramm, M. and K. Bjørlykke
1994. Porosity/depth trends in reservoir sandstones: Assessing the quantitative effects of varying pore-pressure, temperature history and mineralogy, norwegian shelf data. *Clay minerals*, 29(4):475–490.

Ravnås, R., K. Bondevik, W. Helland-Hansen, L. Lømo, A. Ryseth, and R. Steel
1997. Sedimentation history as an indicator of rift initiation and development: the late bajocian-bathonian evolution of the oseberg-brage area, northern north sea. *Norsk Geologisk Tidsskrift*, 77(4):205–232.

Refsgaard, J. C., J. P. Van der Sluijs, J. Brown, and P. Van der Keur
2006. A framework for dealing with uncertainty due to model structure error. *Advances in Water Resources*, 29(11):1586–1597.

Reineck, H.-E. and I. B. Singh
1980. Tidal flats. In *Depositional Sedimentary Environments*, Pp. 430–456. Springer.

Renard, P. and G. De Marsily
1997. Calculating equivalent permeability: a review. *Advances in Water Resources*, 20(5):253–278.

Richards, P., G. K. Lott, H. Johnson, R. W. Knox, and J. B. Riding
1993. 3. jurassic of the central and northern north sea. In *Lithostratigraphic Nomenclature of the UK North Sea*, R. W. Knox and W. G. Cordey, eds. British Geological Survey. Pp. 199.

Ringrose, P. and M. Bentley
2015. *Reservoir model design.* Springer. Pp. 249.

Ringrose, P. S., A. W. Martinius, and J. Alvestad
2008. Multiscale geological reservoir modelling in practice. *Geological Society, London, Special Publications*, 309(1):123–134.

Ringrose, P. S., K. S. Sorbie, P. W. M. Corbett, and J. L. Jensen
1993. Immiscible flow behaviour in laminated and cross-bedded sandstones. *Journal of Petroleum Science and Engineering*, 9(2):103–124.

Roberts, A., G. Yielding, N. Kusznir, I. Walker, and D. Dorn-Lopez
1995. Quantitative analysis of triassic extension in the northern viking graben. *Journal of the Geological Society*, 152(1):15–26.

Rouby, D., H. Fossen, and P. Cobbold
1996. Extension, displacement, and block rotation in the larger gullfaks area, northern north sea: determined from map view restoration. *AAPG bulletin*, 80(6):875–889.

Royer, J., P. Mejia, G. Caumon, and P. Collon
2015. 3d and 4d geomodelling applied to mineral resources exploration—an introduction. In *3D, 4D and Predictive Modelling of Major Mineral Belts in Europe*, Pp. 73–89. Springer.

Sæland, G. T. and G. S. Simpson
1982. Interpretation of 3-d data in delineating a subunconformity trap in block 34/10, norwegian north sea. *AAPG Special Volumes*, Pp. 217–235.

Scheidegger, A.
1974. *The physics of flow through porous media, 3ed.* University of Toronto Press. Pp. 353.

Seifert, D. and J. Jensen
1999. Using sequential indicator simulation as a tool in reservoir description: Issues and uncertainties. *Mathematical Geology*, 31(5):527–550.

Sheriff, R. E. and L. P. Geldart
1995. *Exploration seismology.* Cambridge university press. Pp. 592.

Shewchuk, J. R.
2002. Delaunay refinement algorithms for triangular mesh generation. *Computational geometry*, 22(1):21–74.

Srivastava, R. M.
1994. An overview of stochastic methods for reservoir characterization. *AAPG Special Volumes*, Pp. 3–16.

Strebelle, S.
2002. Conditional simulation of complex geological structures using multiple-point statistics. *Mathematical Geology*, 34(1):1–21.

Sun, D., J. Bloemendal, D. Rea, J. Vandenberghe, F. Jiang, Z. An, and R. Su
2002. Grain-size distribution function of polymodal sediments in hydraulic and aeolian environments, and numerical partitioning of the sedimentary components. *Sedimentary Geology*, 152(3):263–277.

Walker, R. G. and D. J. Cant
1984. Sandy fluvial systems. In *Facies models*, R. G. Walker, ed., volume 1, Pp. 71–89. Geoscience Canada Reprint Series, Geological Society of Canada.

Went, D., R. Hamilton, N. Platt, and J. Underhill
2013. Role of forced regression in controlling brent group reservoir architecture and prospectivity in the northern north sea. *Petroleum Geoscience*, 19(4):307–328.

Yao, T. and A. Chopra
2000. Integration of seismic attribute map into 3d facies modeling. *Journal of petroleum science and engineering*, 27(1):69–84.

Yielding, G., J. Øverland, and G. Byberg
1999. Characterization of fault zones for reservoir modeling: An example from the gullfaks field, northern north sea. *AAPG bulletin*, 83(6):925–951.

Zolotukhin, A. B. and J. R. Ursin
2000. *Introduction to petroleum reservoir engineering.* Norwegian Academic Press (HøyskoleForlaget). Pp. 407.

Appendix A

Appendix: Input graphs

A.1 Porosity well graphs

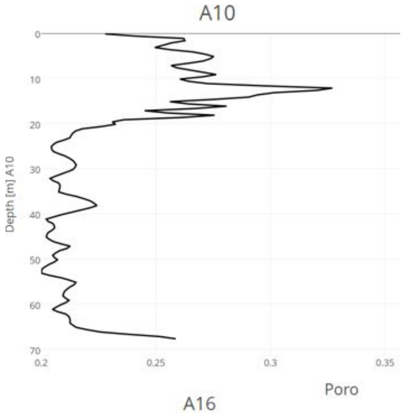
A10
Depth [m] A10
0
10
20
30
40
50
60
70
0.2
0.25
0.3
0.35
Poro

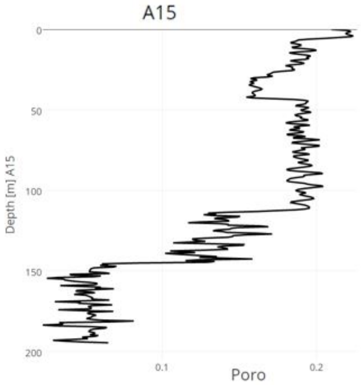
A15
Depth [m] A15
0
50
100
150
200
0.1
0.2
Poro

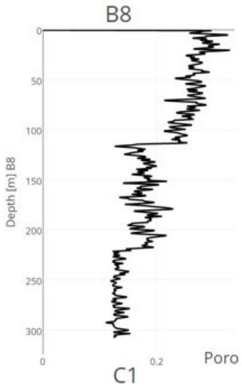
B8
Depth [m] B8
0
50
100
150
200
250
300
0
0.2
Poro

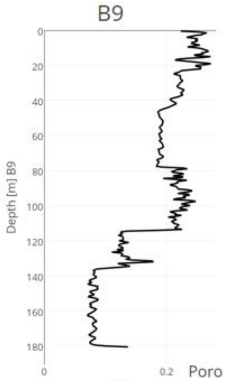
B9
Depth [m] B9
0
20
40
60
80
100
120
140
160
180
0
0.2
Poro

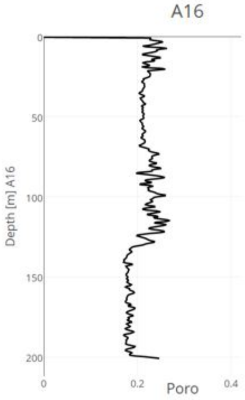
A16
Depth [m] A16
0
50
100
150
200
0
0.2
0.4
Poro

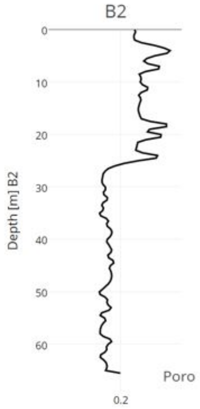
B2
Depth [m] B2
0
10
20
30
40
50
60
0.2
Poro

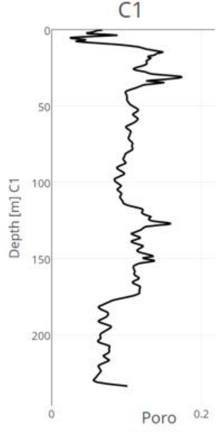
C1
Depth [m] C1
0
50
100
150
200
0
0.2
Poro

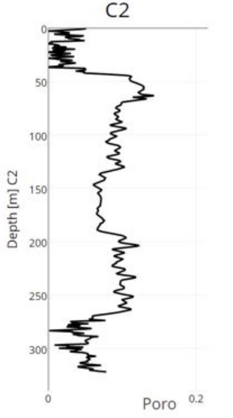
C2
Depth [m] C2
0
50
100
150
200
250
300
0
0.2
Poro

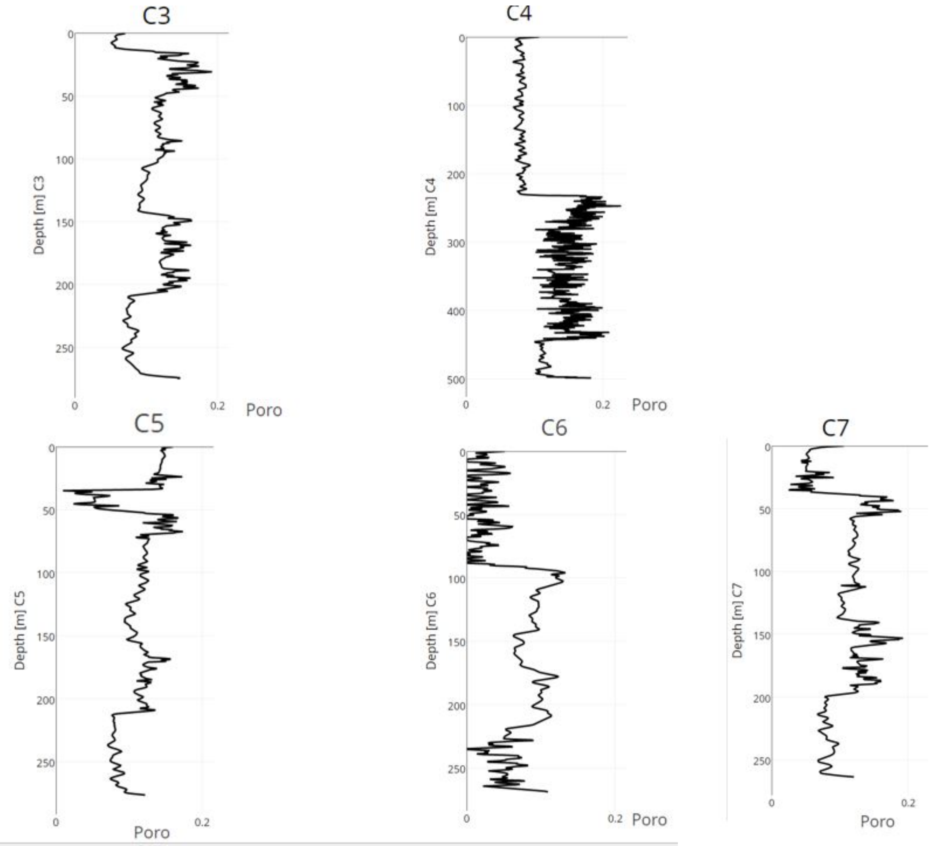
C3
Depth [m] C3
0
50
100
150
200
250
0
0.2
Poro
C4
Depth [m] C4
0
100
200
300
400
500
0
0.2
Poro
C5
Depth [m] C5
0
50
100
150
200
250
0
0.2
Poro
C6
Depth [m] C6
0
50
100
150
200
250
0
0.2
Poro
C7
Depth [m] C7
0
50
100
150
200
250
0
0.2
Poro

A.2 Permeability well graphs

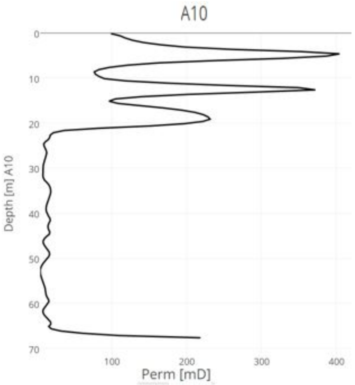

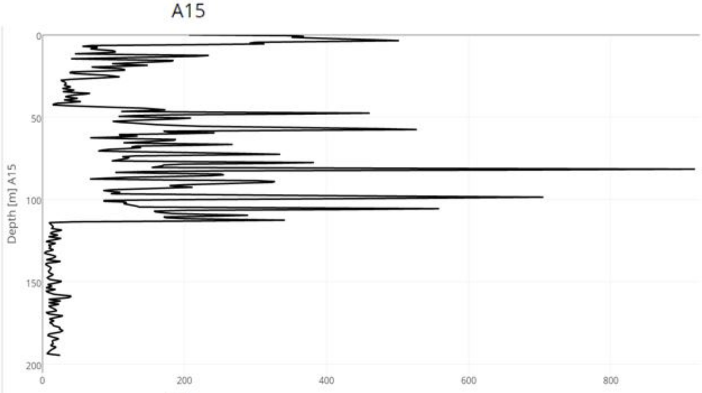

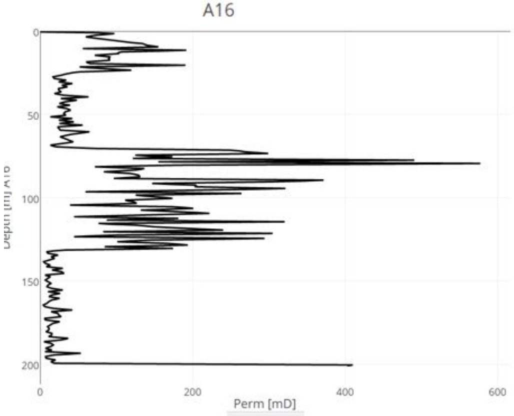

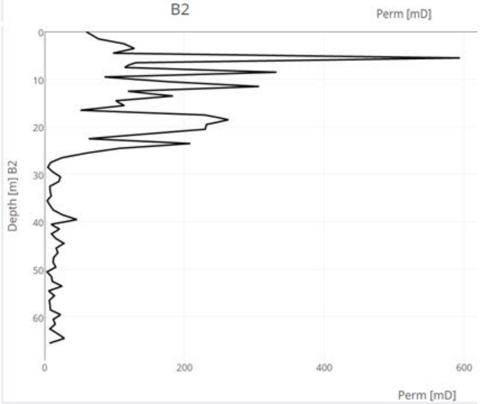

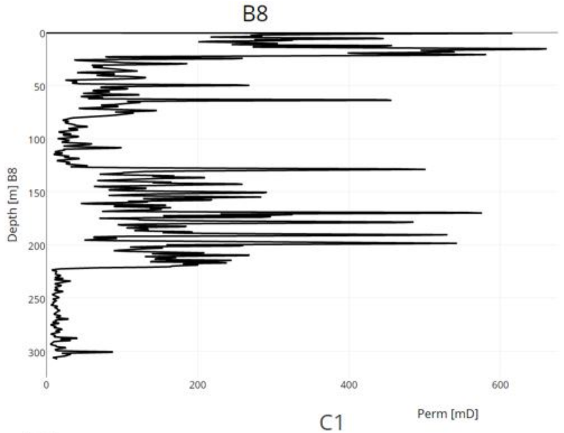
B8
Depth [m] B8
0
50
100
150
200
250
300
0
200
400
600
Perm [mD]

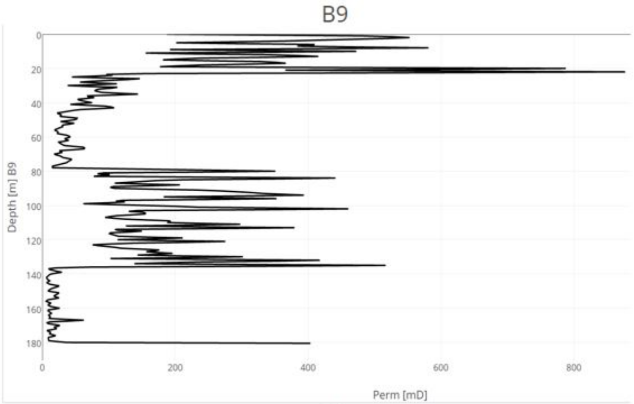
B9
Depth [m] B9
0
20
40
60
80
100
120
140
160
180
0
200
400
600
800
Perm [mD]

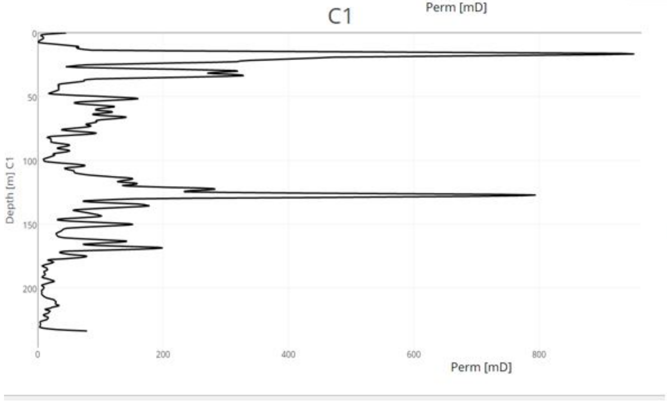
C1
Depth [m] C1
0
50
100
150
200
0
200
400
600
800
Perm [mD]

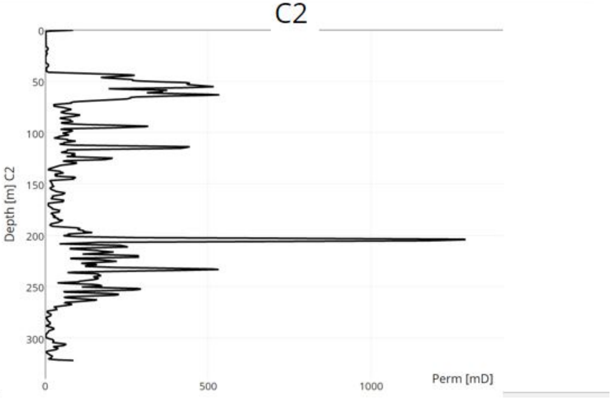
C2
Depth [m] C2
0
50
100
150
200
250
300
0
500
1000
Perm [mD]

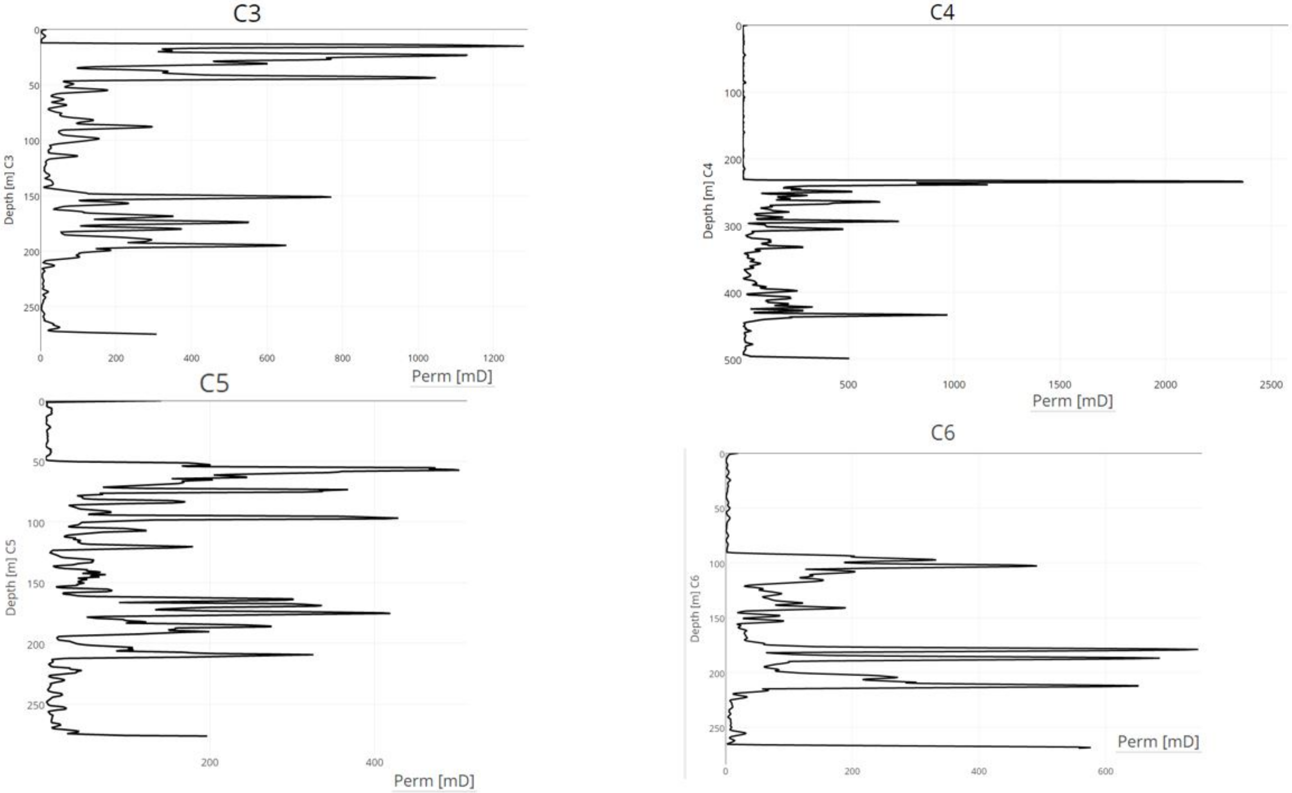
C3
Depth [m] C3
0
50
100
150
200
250
0
200
400
600
800
1000
1200
Perm [mD]
C4
Depth [m] C4
0
100
200
300
400
500
500
1000
1500
2000
2500
Perm [mD]
C5
Depth [m] C5
0
50
100
150
200
250
200
400
Perm [mD]
C6
Depth [m] C6
0
50
100
150
200
250
0
200
400
600
Perm [mD]

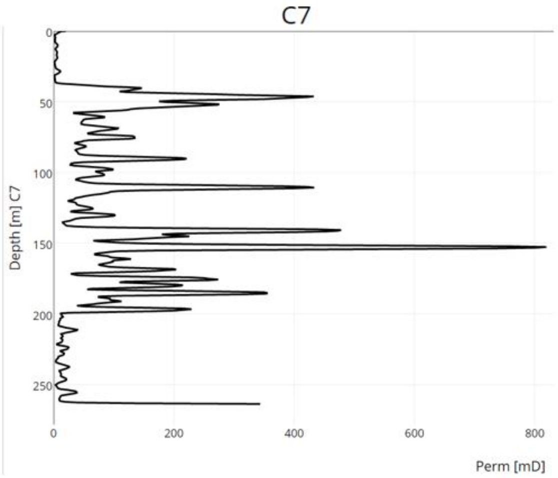
C7
Depth [m] C7
0
50
100
150
200
250
0
200
400
600
800
Perm [mD]

Appendix B

Appendix: Property Model GM fault block 2

B.1 Interpolated Model

B.1.1 Tarbert Upper

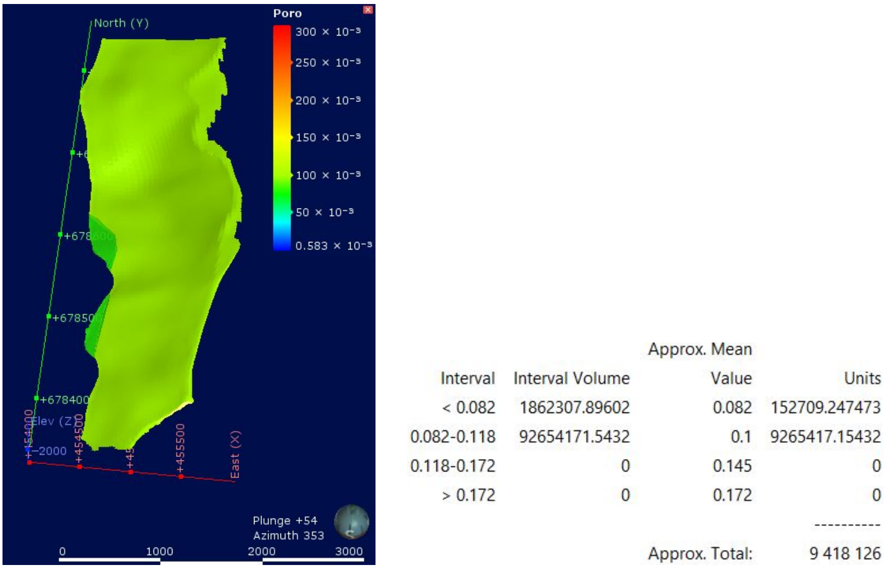
North (Y)
Poro
300 × 10⁻³
250 × 10⁻³
200 × 10⁻³
150 × 10⁻³
100 × 10⁻³
50 × 10⁻³
0.583 × 10⁻³
+678400
+67850
Elev (Z)
−2000
+455500
East (X)
Plunge +54
Azimuth 353
0
1000
2000
3000

Interval	Interval Volume	Approx. Mean Value	Units
< 0.082	1862307.89602	0.082	152709.247473
0.082-0.118	92654171.5432	0.1	9265417.15432
0.118-0.172	0	0.145	0
> 0.172	0	0.172	0

		Approx. Total:	9 418 126

Figure B.1.1. A (Left): Porosity volume model. B (Right): Corresponding statistics.

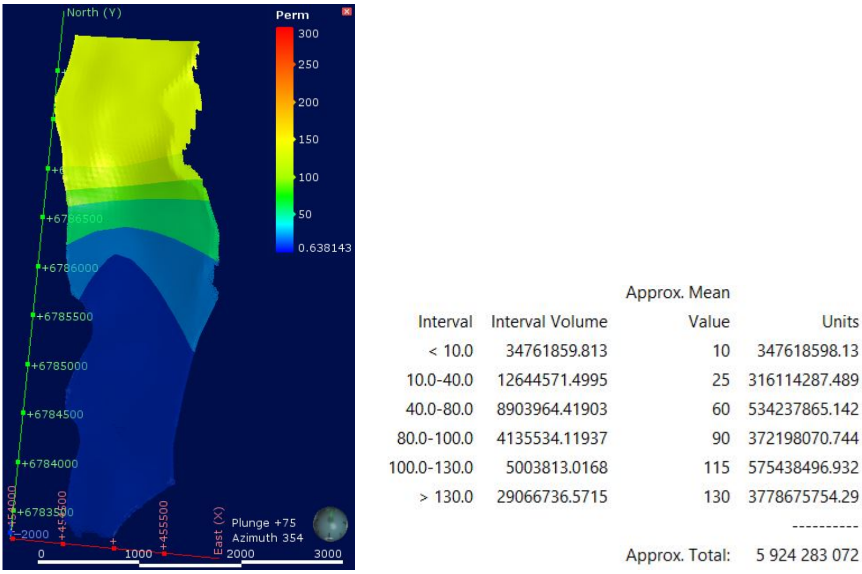
North (Y)
Perm
300
250
200
150
100
50
0.638143
+6786500
+6786000
+6785500
+6785000
+6784500
+6784000
+6783500
-2000
+454000
+455000
+455500
East (X)
Plunge +75
Azimuth 354
0
1000
2000
3000

Interval	Interval Volume	Approx. Mean Value	Units
< 10.0	34761859.813	10	347618598.13
10.0-40.0	12644571.4995	25	316114287.489
40.0-80.0	8903964.41903	60	534237865.142
80.0-100.0	4135534.11937	90	372198070.744
100.0-130.0	5003813.0168	115	575438496.932
> 130.0	29066736.5715	130	3778675754.29

		Approx. Total:	5 924 283 072

Figure B.1.2. A (Left):Permeability volume model. B (Right): Corresponding statistics.

B.1.2 Tarbert Middle

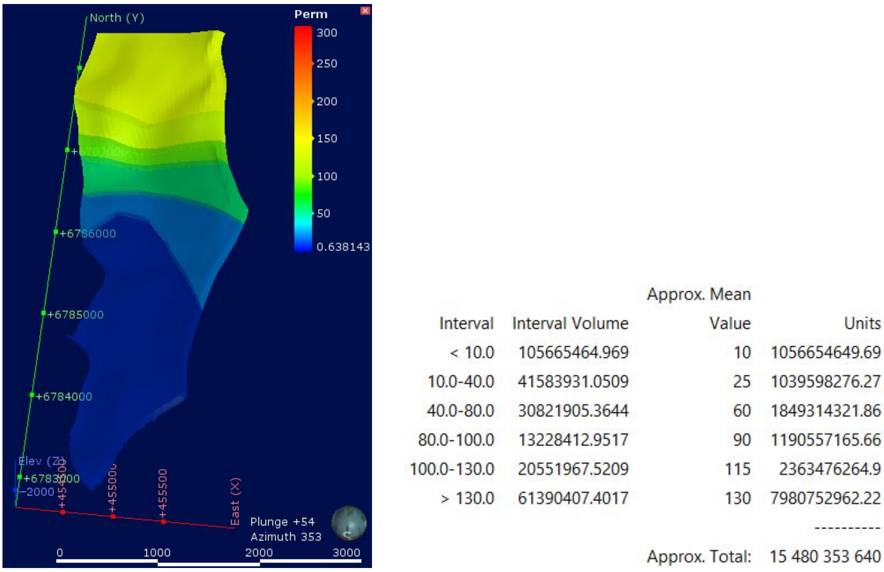
North (Y)
Perm
300
250
200
150
100
50
0.638143
+6786000
+6785000
+6784000
+6783000
Elev (Z)
-2000
+455000
+455500
East (X)
Plunge +54
Azimuth 353
0
1000
2000
3000

Interval	Interval Volume	Approx. Mean Value	Units
< 10.0	105665464.969	10	1056654649.69
10.0-40.0	41583931.0509	25	1039598276.27
40.0-80.0	30821905.3644	60	1849314321.86
80.0-100.0	13228412.9517	90	1190557165.66
100.0-130.0	20551967.5209	115	2363476264.9
> 130.0	61390407.4017	130	7980752962.22

		Approx. Total:	15 480 353 640

Figure B.1.3. A (Left):Permeability volume model. B (Right): Corresponding statistics.

B.1.3 Tarbert Lower

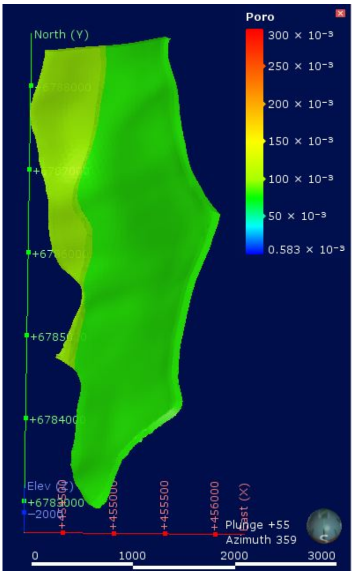
Poro
300 × 10⁻³
250 × 10⁻³
200 × 10⁻³
150 × 10⁻³
100 × 10⁻³
50 × 10⁻³
0.583 × 10⁻³
North (Y)
+6785
+678400
Elev (Z)
+6783000
−2000
+455000
+455500
+456000
East (X)
Plunge +55
Azimuth 359
0
1000
2000
3000

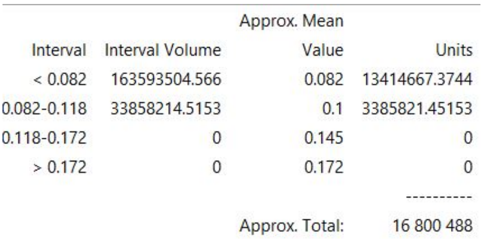

Interval	Interval Volume	Approx. Mean Value	Units
< 0.082	163593504.566	0.082	13414667.3744
0.082-0.118	33858214.5153	0.1	3385821.45153
0.118-0.172	0	0.145	0
> 0.172	0	0.172	0

		Approx. Total:	16 800 488

Figure B.1.4. A (Left):Porosity volume model. B (Right): Corresponding statistics.

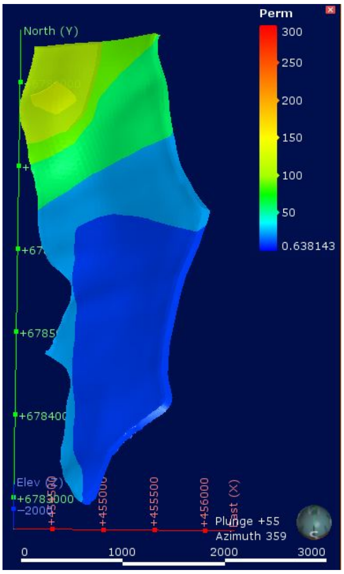
Perm
300
250
200
150
100
50
0.638143
North (Y)
+6785
+678400
Elev (Z)
+6783000
−2000
+455000
+455500
+456000
East (X)
Plunge +55
Azimuth 359
0
1000
2000
3000

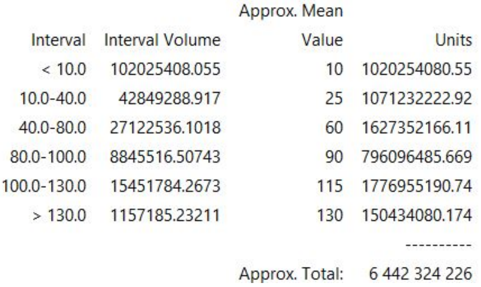

Interval	Interval Volume	Approx. Mean Value	Units
< 10.0	102025408.055	10	1020254080.55
10.0-40.0	42849288.917	25	1071232222.92
40.0-80.0	27122536.1018	60	1627352166.11
80.0-100.0	8845516.50743	90	796096485.669
100.0-130.0	15451784.2673	115	1776955190.74
> 130.0	1157185.23211	130	150434080.174

		Approx. Total:	6 442 324 226

Figure B.1.5. A (Left):Permeability volume model. B (Right): Corresponding statistics.

B.1.4 Ness Upper

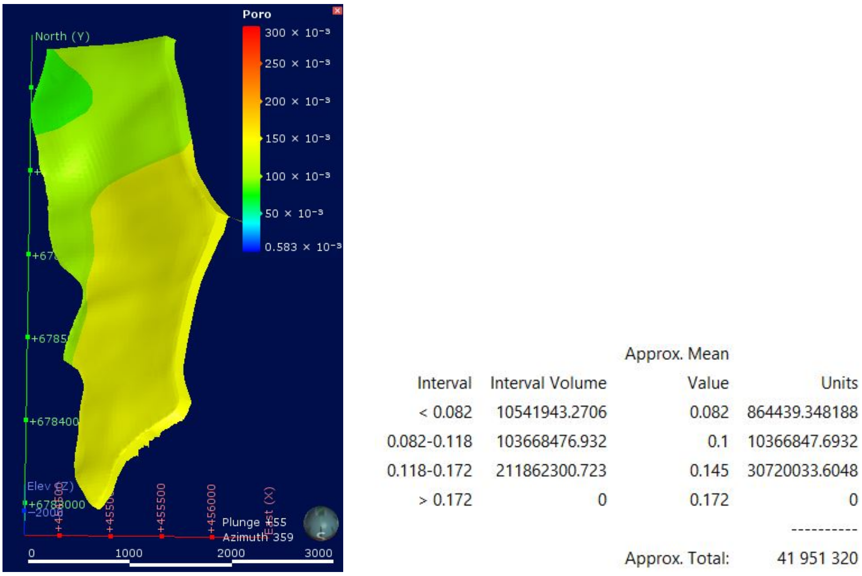
Poro
300 × 10-3
250 × 10-3
200 × 10-3
150 × 10-3
100 × 10-3
50 × 10-3
0.583 × 10-3
North (Y)
+67
+6785
+678400
Elev (Z)
+6783000
-2000
+455000
+4550
+455500
+456000
East (X)
Plunge +55
Azimuth 359
0
1000
2000
3000

Interval	Interval Volume	Approx. Mean Value	Units
< 0.082	10541943.2706	0.082	864439.348188
0.082-0.118	103668476.932	0.1	10366847.6932
0.118-0.172	211862300.723	0.145	30720033.6048
> 0.172	0	0.172	0

		Approx. Total:	41 951 320

Figure B.1.6. A (Left):Porosity volume model. B (Right): Corresponding statistics.

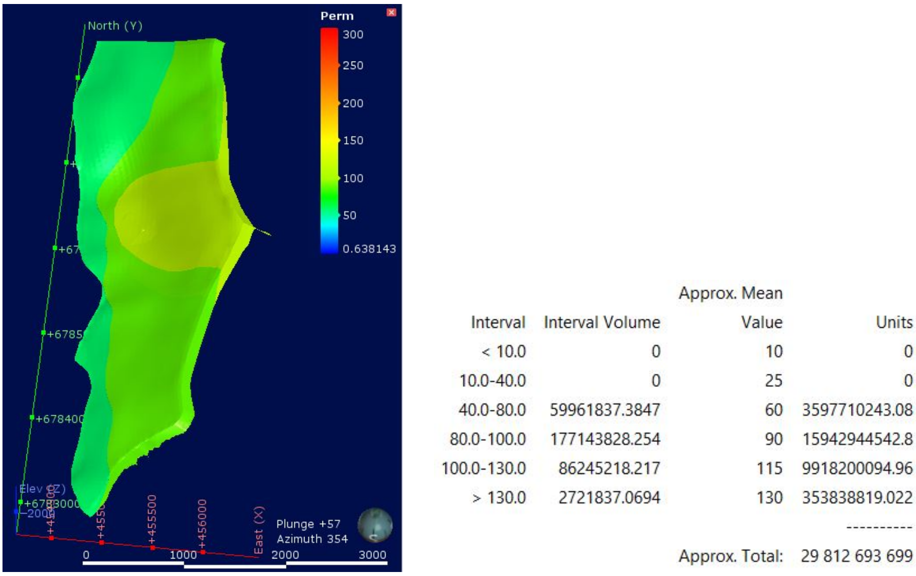
Perm
300
250
200
150
100
50
0.638143
North (Y)
+67
+6785
+678400
Elev (Z)
+6783000
-2000
+455000
+4550
+455500
+456000
East (X)
Plunge +57
Azimuth 354
0
1000
2000
3000

Interval	Interval Volume	Approx. Mean Value	Units
< 10.0	0	10	0
10.0-40.0	0	25	0
40.0-80.0	59961837.3847	60	3597710243.08
80.0-100.0	177143828.254	90	15942944542.8
100.0-130.0	86245218.217	115	9918200094.96
> 130.0	2721837.0694	130	353838819.022

		Approx. Total:	29 812 693 699

Figure B.1.7. A (Left):Permeability volume model. B (Right): Corresponding statistics.

B.1.5 Ness Lower

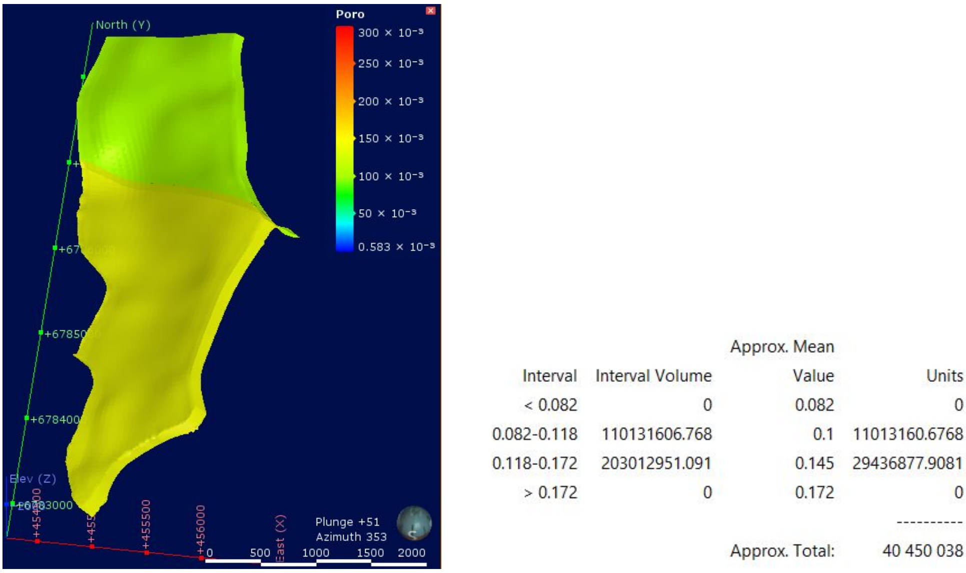
North (Y)
Poro
300 × 10⁻³
250 × 10⁻³
200 × 10⁻³
150 × 10⁻³
100 × 10⁻³
50 × 10⁻³
0.583 × 10⁻³
+678500
+678400
Elev (Z)
+6783000
+455500
+456000
East (X)
Plunge +51
Azimuth 353
0
500
1000
1500
2000

Interval	Interval Volume	Approx. Mean Value	Units
< 0.082	0	0.082	0
0.082-0.118	110131606.768	0.1	11013160.6768
0.118-0.172	203012951.091	0.145	29436877.9081
> 0.172	0	0.172	0

		Approx. Total:	40 450 038

Figure B.1.8. A (Left):Porosity volume model. B (Right): Corresponding statistics.

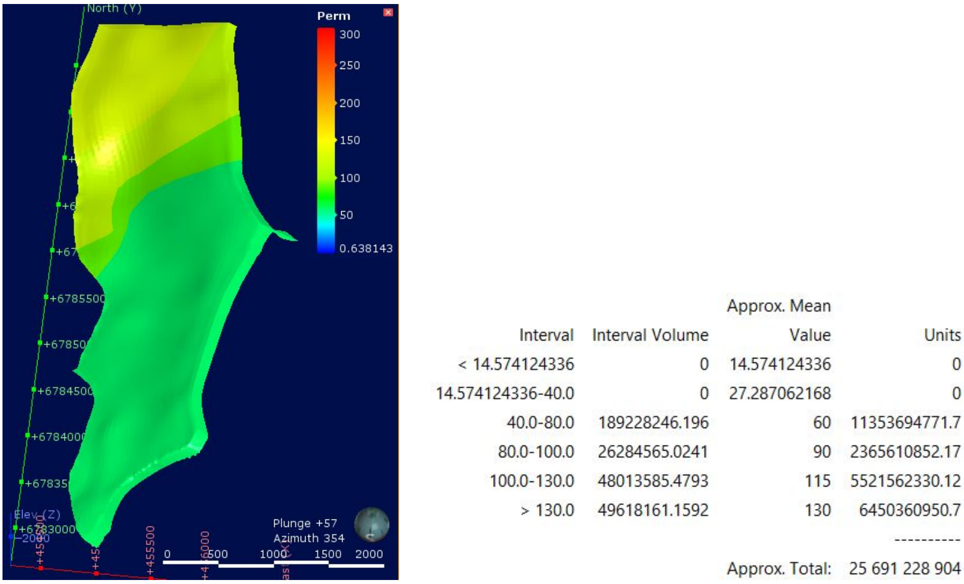
North (Y)
Perm
300
250
200
150
100
50
0.638143
+6785500
+678500
+6784500
+6784000
+678350
Elev (Z)
+6783000
-2000
+455500
East (X)
Plunge +57
Azimuth 354
0
500
1000
1500
2000

Interval	Interval Volume	Approx. Mean Value	Units
< 14.574124336	0	14.574124336	0
14.574124336-40.0	0	27.287062168	0
40.0-80.0	189228246.196	60	11353694771.7
80.0-100.0	26284565.0241	90	2365610852.17
100.0-130.0	48013585.4793	115	5521562330.12
> 130.0	49618161.1592	130	6450360950.7

		Approx. Total:	25 691 228 904

Figure B.1.9. A (Left):Permeability volume model. B (Right): Corresponding statistics.

B.2 Block model

B.2.1 Tarbert Upper

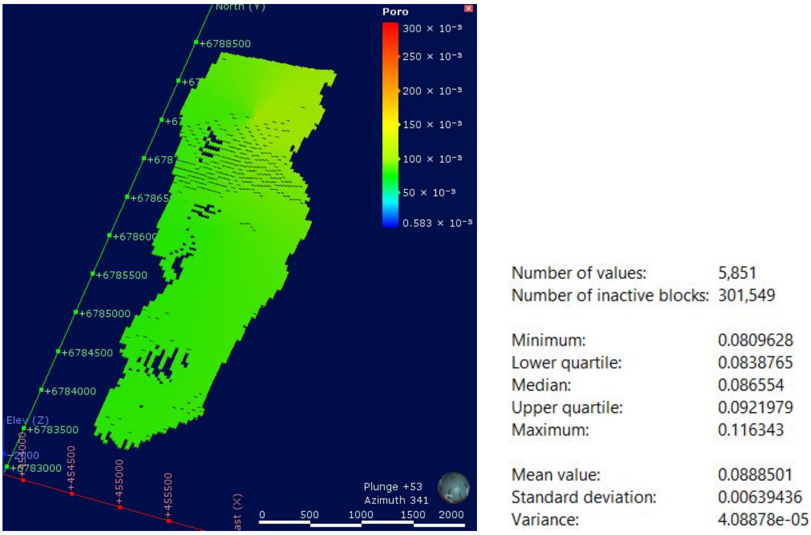
North (Y)
Poro
300 × 10⁻³
250 × 10⁻³
200 × 10⁻³
150 × 10⁻³
100 × 10⁻³
50 × 10⁻³
0.583 × 10⁻³
+6788500
+6785500
+6785000
+6784500
+6784000
+6783500
+6783000
Elev (Z)
+454500
+455000
+455500
East (X)
Plunge +53
Azimuth 341
0
500
1000
1500
2000

Number of values:	5,851
Number of inactive blocks:	301,549
Minimum:	0.0809628
Lower quartile:	0.0838765
Median:	0.086554
Upper quartile:	0.0921979
Maximum:	0.116343
Mean value:	0.0888501
Standard deviation:	0.00639436
Variance:	4.08878e-05

Figure B.2.1. A (Left):Porosity block model. B (Right): Corresponding statistics.

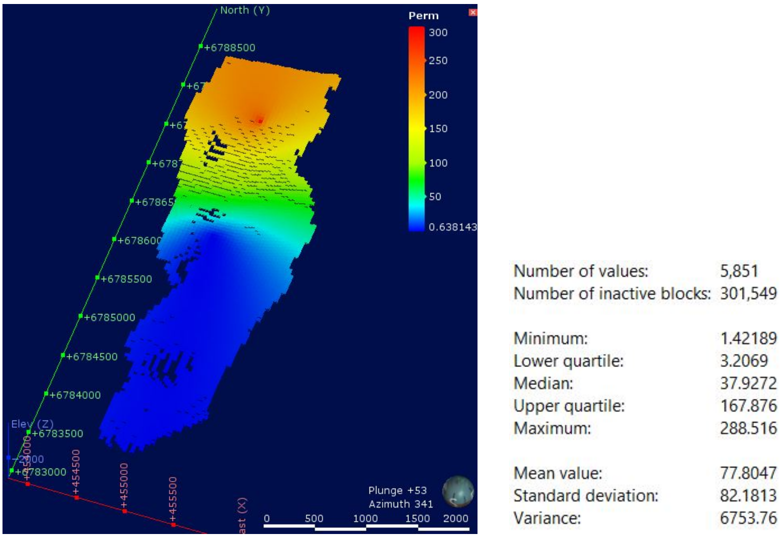
North (Y)
Perm
300
250
200
150
100
50
0.638143
+6788500
+6785500
+6785000
+6784500
+6784000
+6783500
+6783000
Elev (Z)
+454500
+455000
+455500
East (X)
Plunge +53
Azimuth 341
0
500
1000
1500
2000

Number of values:	5,851
Number of inactive blocks:	301,549
Minimum:	1.42189
Lower quartile:	3.2069
Median:	37.9272
Upper quartile:	167.876
Maximum:	288.516
Mean value:	77.8047
Standard deviation:	82.1813
Variance:	6753.76

Figure B.2.2. A (Left):Permeability block model. Red block corresponds with well C2. B (Right): Corresponding statistics.

B.2.2 Tarbert Middle

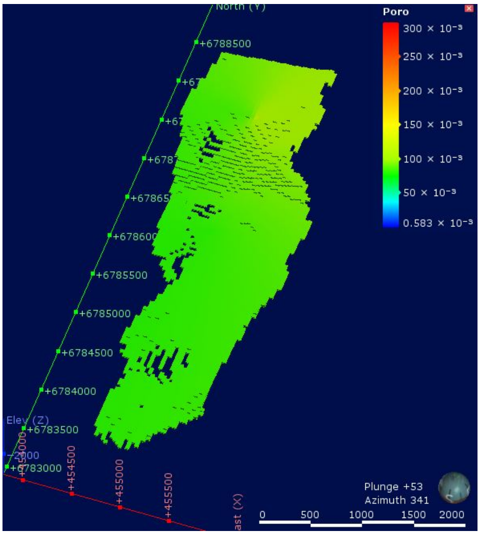
North (Y)
Poro
300 × 10⁻³
250 × 10⁻³
200 × 10⁻³
150 × 10⁻³
100 × 10⁻³
50 × 10⁻³
0.583 × 10⁻³
+6788500
+6785500
+6785000
+6784500
+6784000
+6783500
+6783000
Elev (Z)
+454500
+455000
+455500
East (X)
Plunge +53
Azimuth 341
0
500
1000
1500
2000

Number of values:	5,851
Number of inactive blocks:	301,549
Minimum:	0.0809628
Lower quartile:	0.0838765
Median:	0.086554
Upper quartile:	0.0921979
Maximum:	0.116343
Mean value:	0.0888501
Standard deviation:	0.00639436
Variance:	4.08878e-05

Figure B.2.3. A (Left): Porosity block model. B (Right): Corresponding statistics.

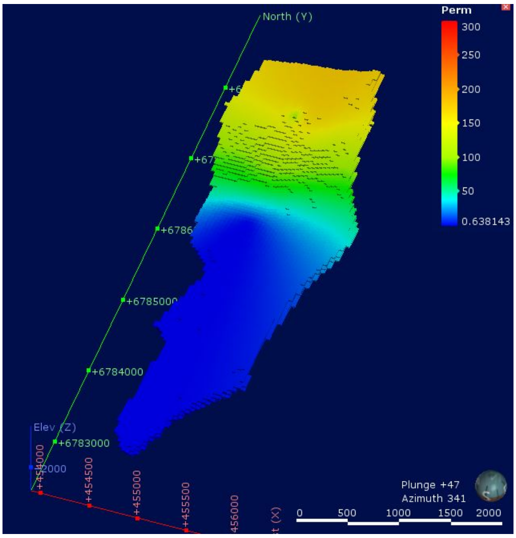
North (Y)
Perm
300
250
200
150
100
50
0.638143
+6785000
+6784000
+6783000
Elev (Z)
+454500
+455000
+455500
456000
East (X)
Plunge +47
Azimuth 341
0
500
1000
1500
2000

Number of values:	17,021
Number of inactive blocks:	334,979
Minimum:	0
Lower quartile:	2.21743
Median:	28.4769
Upper quartile:	120.408
Maximum:	178.803
Mean value:	59.4837
Standard deviation:	64.0867
Variance:	4107.1

Figure B.2.4. A (Left):Permeability volume model. B (Right): Corresponding statistics.

B.2.3 Tarbert Lower

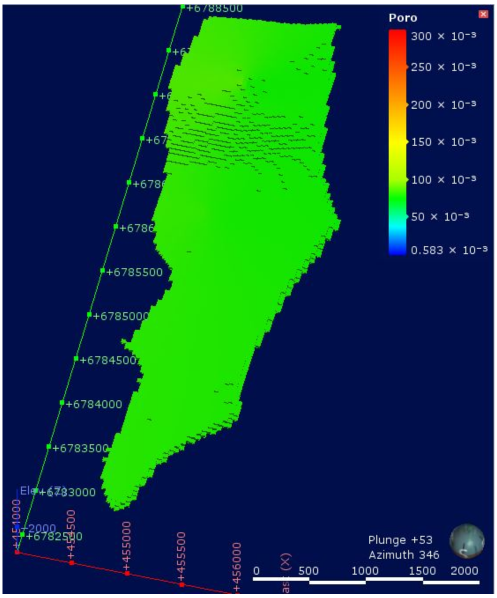
Poro
300 × 10⁻³
250 × 10⁻³
200 × 10⁻³
150 × 10⁻³
100 × 10⁻³
50 × 10⁻³
0.583 × 10⁻³
+6788500
+6785500
+6785000
+6784500
+6784000
+6783500
+6783000
+6782500
+455000
+455500
+456000
Plunge +53
Azimuth 346
0
500
1000
1500
2000

Number of values:	12,341
Number of inactive blocks:	335,339
Minimum:	0.0705927
Lower quartile:	0.0787913
Median:	0.0805151
Upper quartile:	0.0815955
Maximum:	0.0899427
Mean value:	0.0806449
Standard deviation:	0.00228918
Variance:	5.24034e-06

Figure B.2.5. A (Left): Porosity block model. B (Right): Corresponding statistics.

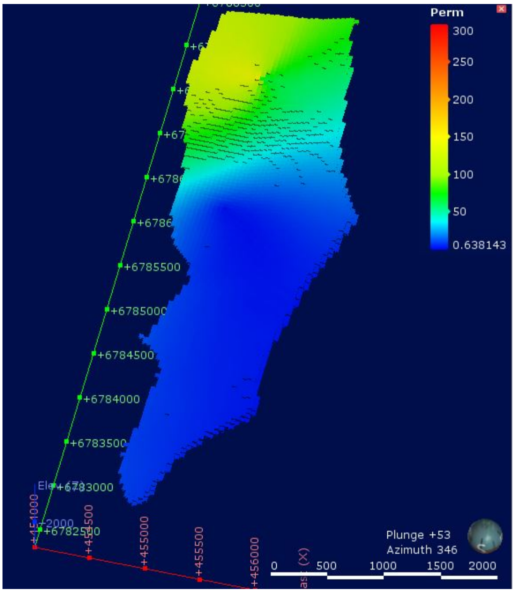
Perm
300
250
200
150
100
50
0.638143
+6785500
+6785000
+6784500
+6784000
+6783500
+6783000
+6782500
+455000
+455500
+456000
Plunge +53
Azimuth 346
0
500
1000
1500
2000

Number of values:	12,341
Number of inactive blocks:	335,339
Minimum:	2.31395
Lower quartile:	5.6411
Median:	9.56598
Upper quartile:	44.8777
Maximum:	150.002
Mean value:	29.666
Standard deviation:	36.3204
Variance:	1319.17

Figure B.2.6. A (Left): Permeability block model. B (Right): Corresponding statistics.

B.2.4 Ness Upper

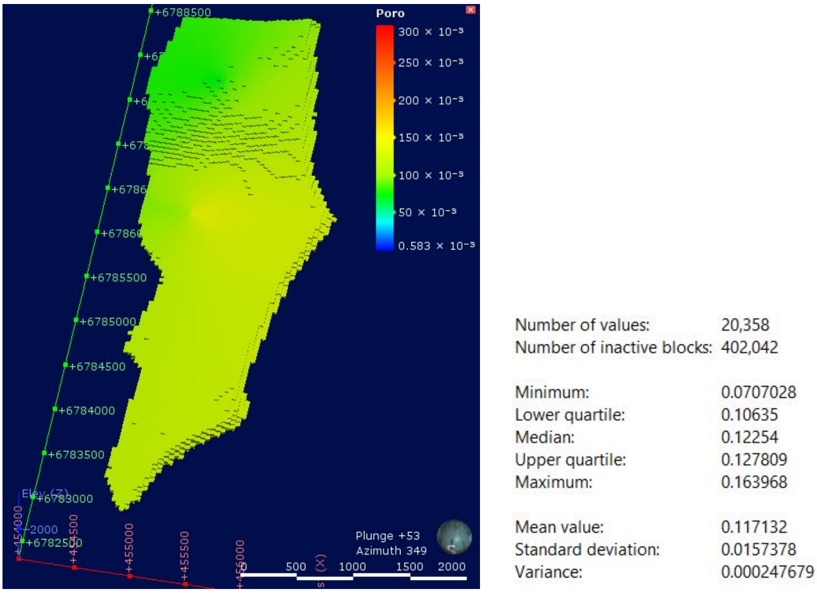

Poro
300×10^{-3}
250×10^{-3}
200×10^{-3}
150×10^{-3}
100×10^{-3}
50×10^{-3}
0.583×10^{-3}
+6788500
+6785500
+6785000
+6784500
+6784000
+6783500
+6783000
+6782500
Elev (Z)
2000
+454000
+454500
+455000
+455500
+456000
(X)
Plunge +53
Azimuth 349
0
500
1000
1500
2000

Number of values:	20,358
Number of inactive blocks:	402,042
Minimum:	0.0707028
Lower quartile:	0.10635
Median:	0.12254
Upper quartile:	0.127809
Maximum:	0.163968
Mean value:	0.117132
Standard deviation:	0.0157378
Variance:	0.000247679

Figure B.2.7. A (Left): Porosity block model. B (Right): Corresponding statistics.

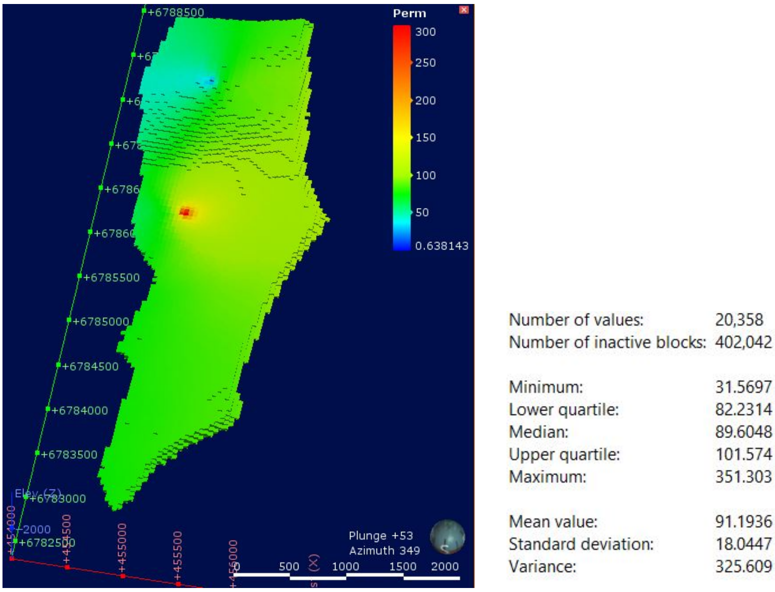

Perm
300
250
200
150
100
50
0.638143
+6788500
+6785500
+6785000
+6784500
+6784000
+6783500
+6783000
+6782500
Elev (Z)
2000
+454000
+454500
+455000
+455500
+456000
(X)
Plunge +53
Azimuth 349
0
500
1000
1500
2000

Number of values:	20,358
Number of inactive blocks:	402,042
Minimum:	31.5697
Lower quartile:	82.2314
Median:	89.6048
Upper quartile:	101.574
Maximum:	351.303
Mean value:	91.1936
Standard deviation:	18.0447
Variance:	325.609

Figure B.2.8. A (Left): Permeability block model. Red block corresponds with well C4. B (Right): Corresponding statistics.

B.2.5 Ness Lower

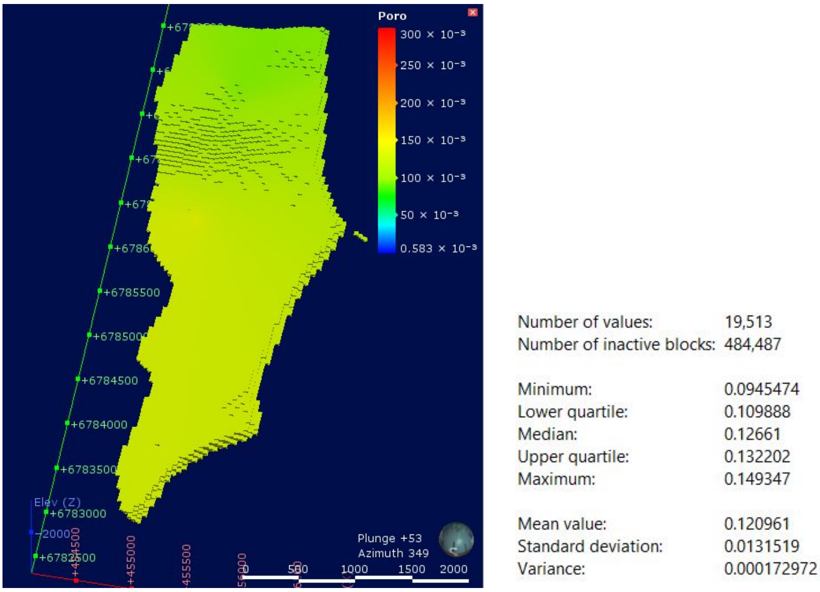
Poro
300 × 10⁻³
250 × 10⁻³
200 × 10⁻³
150 × 10⁻³
100 × 10⁻³
50 × 10⁻³
0.583 × 10⁻³
+6785500
+6785000
+6784500
+6784000
+6783500
+6783000
+6782500
Elev (Z)
-2000
+454500
+455000
+455500
Plunge +53
Azimuth 349
0
500
1000
1500
2000

Number of values:	19,513
Number of inactive blocks:	484,487
Minimum:	0.0945474
Lower quartile:	0.109888
Median:	0.12661
Upper quartile:	0.132202
Maximum:	0.149347
Mean value:	0.120961
Standard deviation:	0.0131519
Variance:	0.000172972

Figure B.2.9. A (Left): Porosity block model. B (Right): Corresponding statistics.

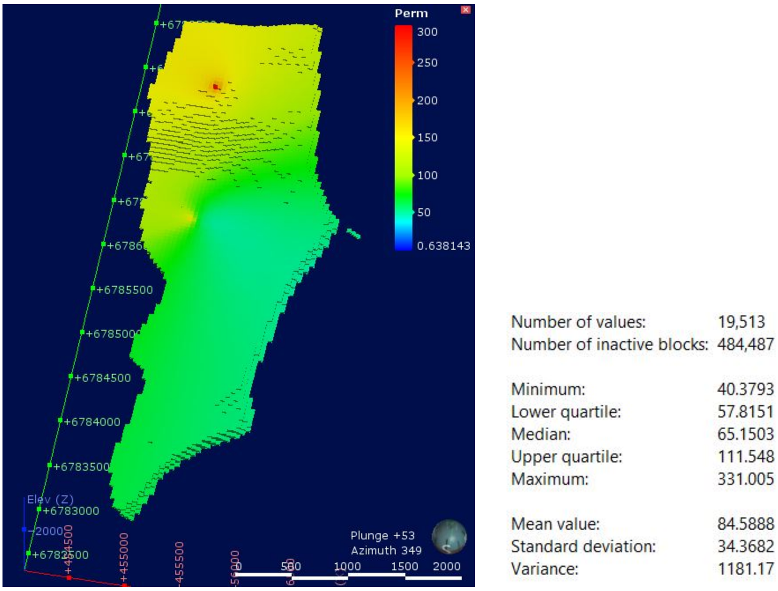
Perm
300
250
200
150
100
50
0.638143
+6785500
+6785000
+6784500
+6784000
+6783500
+6783000
+6782500
Elev (Z)
-2000
+454500
+455000
+455500
Plunge +53
Azimuth 349
0
500
1000
1500
2000

Number of values:	19,513
Number of inactive blocks:	484,487
Minimum:	40.3793
Lower quartile:	57.8151
Median:	65.1503
Upper quartile:	111.548
Maximum:	331.005
Mean value:	84.5888
Standard deviation:	34.3682
Variance:	1181.17

Figure B.2.10. A (Left): Permeability block model. Red block corresponds with well C2. B (Right): Corresponding statistics.